Sound propagation in dry granular materials: discrete element simulations, theory, and experiments

Sound propagation in dry granular materials:
discrete element simulations, theory, and experiments.
O. Mouraille

Cover image: by O. Mouraille

Printed by Gildeprint Drukkerijen, Enschede
Thesis University of Twente, Enschede - With references - With summary in Dutch.
ISBN 978-90-365-2789-7

SOUND PROPAGATION IN DRY GRANULAR MATERIALS: DISCRETE ELEMENT SIMULATIONS, THEORY, AND EXPERIMENTS

PROEFSCHRIFT

ter verkrijging van
de graad van doctor aan de Universiteit Twente,
op gezag van de rector magnificus,
prof. dr. H. Brinksma,
volgens besluit van het College voor Promoties
in het openbaar te verdedigen
op vrijdag 27 februari 2009 om 15.00 uur

door

Orion Mouraille

geboren op 26 december 1979
te Montpellier, Frankrijk

Dit proefschrift is goedgekeurd door de promotor:

prof. dr. S. Luding

Samenstelling promotiecommissie:

prof. dr. F. Eising	Universiteit Twente, voorzitter/secretaris
prof. dr. S. Luding	Universiteit Twente, promotor
prof. dr. D. Lohse	Universiteit Twente
dr. N. Kruyt	Universiteit Twente
dr. Y. Wijnant	Universiteit Twente
prof. dr. X. Jia	Université Paris-Est Marne-la-Vallée
prof. dr. H. Steeb	Universität Bochum
prof. dr. W. Mulder	Technische Universiteit Delft

à Sanne et Elia

Contents

1

Introduction

The study of sound wave propagation in granular materials brings together two large fields of research: (i) the propagation of vibrations, sound, or more generally mechanical waves, in disordered heterogeneous media and (ii) the behavior and phenomenology of discrete and nonlinear granular materials in general.
In the following, a general introduction to granular matter is given. Then the effect of several granular material peculiarities, like heterogeneity, multiple-scales, particle rotations, tangential elastic forces and friction, history, etc ... on the wave propagation behavior will be discussed. Some characteristics of mechanical waves in disordered heterogeneous media like attenuation, dispersion and several non-linearities are introduced.
Finally an outline of the thesis will be given.

1.1 Granular matter

The term "granular matter" describes a large number of grains or particles acting collectively as an ensemble. Many examples for this material can be found in our daily life. Food grains like cereals or sugar, pharmaceutical products like powders or tablets, but also many examples in nature like sand, snow, or even "dust" clouds in space. In this thesis we consider static, solid-like situations where the particles are confined, i.e. they are held together by external forces.
According to the definition in [28], the name "granular material" is given to collections of particles when the particle size exceeds 1μm. Particles smaller than 1μm are significantly sensible to Brownian motion and the system behavior starts to be driven by temperature, which implies a totally different physical description. In general, classical thermodynamic laws are not sufficient for granular materials. As an illustration, a representative energy for granular materials is the potential energy of one grain mgd, with m its mass, d its diameter and g the gravitational

acceleration. For a sand grain with $d = 1\text{mm}$ and a density $\rho = 2500\text{kg/m}^3$, this energy is about 13 orders of magnitude larger than the classical thermal agitation $k_B T$. Even if a granular temperature can be defined analogously to the classical temperature, i.e., proportional to the root mean square of grain velocity fluctuations, the granular materials are a-thermal, because thermal fluctuations are negligible.

The particularity of granular matter [11,12,34,38–40,43–45,60,94,99] is that it consists of solid particles, while at the same time being able to realize, depending on the boundary conditions, the three different states, solid, liquid, and gas. Indeed, it behaves as a solid when we walk on the sand at the beach, as compacted granular material at rest can sustain relatively large stresses if the grains can not escape to the sides. It can behave as a liquid: the sand flows in the hourglass, as does snow in an avalanche. Also, a gas-like behavior can be observed when the particles are sustained in the air by the wind during sand storms.

The difference with a usual liquid or gas is that, to be maintained in a certain equilibrium state, a constant input of energy from outside the system is needed as granular materials are highly dissipative. The inelastic and frictional collisions between particles are such that granular materials exhibit a very short relaxation time when they evolves towards the state of zero-energy without external input of energy. Shaking a granular bed under different conditions allows to determine a phase diagram where all the different states are present [29]. These experiments are closely related to the mixing behavior of granular materials, which, under certain conditions (amplitude and frequency for the shaking bed or the mixing method in a mill), can show segregation or mixing, the former is the well-known Brazil-nut effect which brings the large parts in breakfast cereals to the top.

Wet granular materials, as well as cohesive, frictional, fine powders, show a peculiar flow behavior [18, 64, 67, 89, 114]. Adhesionless powder flows freely, but when inter-particle adhesion due to, e.g., van der Waals forces is strong enough, agglomerates or clumps form, which can break into pieces again [51,108,109,111]. This is enhanced by pressure- or temperature-sintering [65] and, under extremely high pressure, tablets or granulates can be formed from primary particles [69–72]. Applications can be found, e.g. in the pharmaceutical industry.

One more specific property of granular matter is dilatancy. A highly compacted granular material must expand (or dilate) before it can deform. The dry area left by a foot when walking on wet sand close to the water is an illustration of this phenomenon. The shear stress exerted by the foot on the sand results in a dilatation of the compacted bed with increase in volume. By drainage under gravity, the water at the surface is forced into the created voids and leaves a dry surface.

1.2 Peculiarities of granular materials and wave propagation

Mechanical waves are disturbances that propagate through space and time in a medium in which deformation leads to elastic restoring forces. This produces a transfer of momentum or energy from one point to another, usually involving little or no associated mass transport. Probing a material with sound waves can give useful information on the state, the structure and the mechanical properties of this material. Therefore, it is important to study, preferably separately, how each of the characteristics of granular materials influences the wave propagation behavior. Concerning this, the main issues are described in the following.

Multi-scale

In granular materials, four main scales are present. (1) The contact scale, also denoted as the micro-scale, where a typical length can be for example the size of imperfections at the surface of a grain. (2) The particle scale, where the radius or the diameter of the particles are the typical lengths. (3) The length of force chains (described later in the introduction), typically around 10 to 20 particles diameters. The so-called "meso-scale" can be placed between the particle and the force chain scale. (4) The system scale, or macro-scale can vary from a few grain diameters (meso- and macro-scale are then overlapping) in a laboratory experiment with a chain of beads, to an almost infinite number of grain diameters in seismic applications.
In practice, the size of the granular sample as compared to the particle size determines the degree of scale separation in the system. On the other hand, it is not completely clear whether the particle size or the length of (force-chains) correlated forces - which is proportional to the particle size - is the appropriate control parameter. In some applications, when system and particle size are of the same order the material does not allow for scale separation, i.e. it is not possible to distinguish between the micro- and the macroscopic scale.

The difficulty in describing wave phenomena in granular materials in large-scale applications with a theoretical continuum approach is that the micro- and meso-scale phenomena are very complex and hard to describe with few parameters.
Many studies [13, 20, 35, 83, 104] try to improve the continuum (large-scale) description of the material by including discrete (micro-scale) features like micro-rotations (Cosserat-type continuum). However, there is still a long way to go as

the complexity of the mathematical description increases exponentially with the number of parameters. More generally, the problem faced can be formulated very simply: How to describe very complex phenomena with only a few parameters. One hopes that the answer lies in a pertinent choice of a few critical relevant parameters. However, complexity seems to be self conservative. As consequence, a remarkable contrast is observed between some very advanced theoretical approaches (cited above) trying to bridge at once macro- and micro-scale, where the level of description is such that the mathematics becomes unsolvable or very time consuming numerically, and some very simple laboratory experiments with regular arrangement of spherical monodisperse beads [5, 22, 50, 75, 84, 90], where the meso- and the micro-scale are studied in detail, leaving the extrapolation to the macro-scale as the open issue.

Heterogeneities

The heterogeneous nature of a granular material can be illustrated by the concept of force chains. Force chains are chains of particles that sustain a large part of the (shear) stress induced by a given load due to geometrical effects. Therefore, force chains are partly responsible for the heterogeneities (neighboring contacts/particles can have forces different by orders of magnitude) and for non-isotropic distribution of stress in a granular packing [12]. The chains are fragile and susceptible to reorganization and their irregular distribution in the material means that granular materials exhibit a strong configuration and history dependence [42]. Those chains usually have a length of a few grains to few tens of grain diameters.

A recurrent and very interesting issue concerns the interactions of those force chains with a wave propagating in the material. It seems that in contradiction to early intuitions [58], the wave does not propagates preferentially along the force chains [102]. However, there are indications that the wave is traveling faster along it [25]. Many open questions are remaining like whether the wave preferentially travels along force chains or if those chains form a barrier to transmission. An important issue bringing together multi-scale behavior and heterogeneity, is the length scale at which the system is probed. Some experimental and numerical studies [5, 48, 49, 102, 118] showed that at the scale of the force chains, no plane waves were propagating. Indeed, the wave-lengths and the heterogeneity length-scale are of the same order. The waves are thus scattered in the system. As a result, different wave velocities are observed whether the system is probed at the scale of the force chains or at the long wavelength limit scale (very large systems). Scattered waves are propagating slower as their traveling path is not the shortest one.

Rotations, tangential elastic forces and friction

Usually neglected in a first approximation, rotational degrees of freedom are very important in the description of granular materials [96]. The description of particle rotations is relatively straightforward. However, their role in the determination of tangential contact forces, which are directly linked to energy loss or to rheology for example, is hard to determine. The normal restoring forces can directly be related to the usual continuous elastic parameters of the grain material like bulk and shear modulus and to the stress or strain path history of the system. For the tangential elastic forces, it is much more complex. They do not only depend on the above mentioned parameters and history, but also on the surface state at the contact. This state can exhibit a strong plastic behavior with possibly several phases involved, in case of wetting [17], with large and short time-scale variation depending on temperature, breakage, etc. Those phenomena need to be described at a micro- (contact-) scale at least a few orders of magnitude smaller than the meso- (grain-) scale.

Closely related to this, the frictional behavior of granular materials, in case of dry grains is responsible for stick-slip behavior. Two grains in contact that are sheared can stick or slide, depending on the ratio between tangential and normal forces. The critical value for the ratio is called the Coulomb friction coefficient μ. Related, are also the rolling and torsion friction, but those will not be further addressed in this thesis, we rather refer to Ref. [71].

All those issues related to rotations and friction are crucial in the description of the wave propagation behavior [23,83,96,104,121], as they imply different transfer modes of momentum and energy. Rotations are responsible for the coupling between shear and rotation acoustic modes and must be taken into account when measuring the attenuation of a shear wave, for example. Friction is, for example, responsible for the conversion of a part of the mechanical energy of a wave into sound or heat.

History

The multiplicity of possible equilibrium states (more unknown than equations with frictional degrees of freedom) makes the history of the state of the material crucial for the description of its future evolution. As a consequence, the preparation procedure in the case of a laboratory experiment is crucial. Usually, several techniques are tested in order to get, at least on the level of macro-quantities as density, a fair reproducibility. At the particle level, or even at the contact level, the effect of different initial configurations can only be averaged out by doing statistics over many samples. The frictional nature of granular materials

is mostly responsible for this. As the state of the media directly influences the wave passing through it, and vice versa, the importance of history is obvious.

Dispersion

When the wave-number, which describes the propagation behavior of a wave in a given material, is frequency-dependent, this is called dispersion. Frequency, group or phase velocity and wave-number are related to each other, $v_g(\omega) = d\omega(k)/dk$ for the group velocity and $v_p(\omega) = \omega/k(\omega)$ for the phase velocity, with ω the frequency and k the wave number. As a consequence, different frequencies propagate at a different wave speed and a wave packet containing many frequencies tends to broaden, to disperse itself as the wave is traveling. In many materials, mechanical waves do show dispersive behavior. This phenomenon is directly related to the range of frequencies considered. In most applications one can define a long wave-length limit, where the wave-length is much larger than the grain size and a short wave limit, where the wave-length is of the order of the grain size. In the latter case, the dispersion is highest as comparable wavelengths can correspond to a different small number of particles. A simple illustration of this phenomenon is the dispersion relation of a one-dimensional chain of beads (1D spring-mass system) [6,30]. Dispersion is thus a real issue in the wave propagation in granular materials, as the material acts as a filter for the frequencies [20, 48], letting the low frequencies (large wave-lengths) pass through. In addition to dispersion, the material can delay or block the high frequencies (short wave-lengths). For shear modes and their coupled rotational modes, the dispersion relation can exhibit band gaps where no propagation is observed for some range of frequencies [23, 35, 75, 83, 96, 104, 121, 124].

Attenuation

Wave attenuation is one of the key mechanisms. It is caused by particle displacements and rotations, with energy transfer from one mode to the other, by friction, with energy losses (heat or sound), but also by viscous effects at the contact (wet bridges, water saturation). It is in particular important for geophysicists, who analyze the time signals of seismic waves, in order to determine the composition of the subsurface. The magnitude of attenuation is giving precious information on the nature of the material the wave has passed through. One can distinguish between the extrinsic attenuation arising from the wave source characteristics, source-material interface, geometrical spreading, etc., and the intrinsic attenuation related to the material (state) itself, viscous effects at the contact, mode conversions, etc. A well-known measure for the intrinsic attenuation is the "Q"

factor [115], defined as $Q = \mathrm{Re}(k)/2\,\mathrm{Im}(k)$ with k the wave number, used by geophysicists in their study of the subsurface.

Non-linearity

Wave propagation in granular materials involves non-linearities of different types. The first two non-linearities are found in the contact description between two particles.

At the contact: In the absence of long range forces, or water bridges and for a strong enough wave amplitude, a two-particle contact may open and close several times while the wave is passing through. The influence of the non-linearity due to the "clapping contacts" non-linearity has been studied in Ref. [119]. In addition, the contact between two spherical beads can be described by the Hertz contact law, where the normal force $|f| = k_H \delta^{3/2}$ (with k_H a stiffness coefficient) depends non-linearly on the one dimensional equivalent geometrical interpenetration (overlap) δ. The question of the relevance of this contact law for wave propagation in granular material has been discussed, e.g., in Refs. [21, 93].

Wave amplitude and confining pressure: A third non-linearity, related to the previous ones, is that the response to an excitation could be non-proportional to the amplitude of this excitation [59]. A strong excitation may open or close contacts (see above), create sliding contacts, and also changes the local configuration possibly on scales much larger than the particle size. This might increase the wave attenuation, as acoustic modes and energy conversion are enhanced. A second consequence is that the local effective stiffness and/or density is changed, implying a different wave velocity.

Related to this is the wave velocity dependence on the confining pressure. A different scaling at low confining pressures for the incremental elastic moduli, $p^{1/2}$ instead of the expected $p^{1/3}$ scaling for higher confining pressures derived from the Hertz contact law [118] (or $p^{1/4}$ instead of $p^{1/6}$ for the wave velocity), has been reported in various studies [22, 33, 49, 57, 100].

Whether it can be attributed to a variation in the number density of Hertzian contacts, due to buckling of particle chains [33], or interpreted in terms of progressive activation of contacts [22], is still an open issue. Numerical studies [100] have also helped to derive this velocity dependence for granular columns with different void fractions.

For almost zero confining pressure, the so-called jamming state of granular materials is realized and wave propagation in granular material near the jamming point constitutes a new and interesting field of research [102].

When the confining pressure is very low and the excitation amplitude is very high, one can have additional non-linearities like shock-waves propagating in the granular material. This is a field of research in itself [36, 50, 85, 90, 124]. This is not the subject of this thesis where we focus on strongly confined situations at rather high stresses.

1.3 Thesis goal and overview

The goal of this thesis is to investigate the role and the influence of micro properties at the contact and the meso-scale (such as friction, particle rotation, contact disorder) on the macro-scale sound wave propagation through a confined granular system. This is done with help of three-dimensional discrete element simulations, theory, and experiments that are introduced in chapter 2. The reader should not be surprised by the presence of some redundancy, as this thesis contains three published full papers included in chapters 4.1, 4.2 and 5.1, as well as three draft papers in chapters 2, 3, and 5.2.

In the second chapter, in addition to experiments, a data analysis technique, the *spectral ratio technique* (SRT), is presented. It is a tool used to analyze sound wave records in order to estimate the quality "Q" factor, which is a measure for the wave attenuation. One strength of this technique is that it gives an objective estimation of the intrinsic frequency dependent attenuation of the material (attenuation due to the interaction between the wave and the material) and it disregards the extrinsic attenuation due to the source and/or subsurface geometry. The technique is first derived in detail, followed by a discussion on the advantages and the limits of its applicability. The SRT is then applied to some numerical simulation, for which plenty of additional information is easily accessible, in order to judge the technique. Furthermore, it is applied to preliminary experiments in order to extract, in addition to the "Q" factor, the phase and the group velocity. Finally, a new experimental set-up, designed to better understand attenuation, phase and group velocities in a granular material, will be proposed.

The third chapter deals with the effect of tangential contact elasticity on the dispersive behavior of regular granular packings by comparing numerical simulation results to theoretical predictions. The latter are derived in the first part of the chapter, based on a single particle unit-cell periodic system and its harmonic wave description. Then, independently, numerical results on the dispersion relation are obtained by the analysis of different transient waves through a regular FCC (Face Centered Cubic) lattice granular material with rotational degrees of

freedom and tangential elasticity. The dispersion relations obtained with both approaches are compared and discussed for a better understanding of rotational waves.

In the fourth chapter, the implementation of advanced contact models involving adhesion and friction in a discrete element model (DEM) is described for regular and fully disordered structures.
In the first part, the influence of dissipation and friction and the difference between modes of agitation and propagation (compressive/shear) in a regular three-dimensional granular packing are detailed. The wave speed is analyzed and compared to the result from a continuum theory approach. The dispersion relation is extracted from the data and compared to theoretical predictions. Furthermore, results on the influence of small perturbations in the ordered structure of the packing (applying a tiny-size distribution to the particles) on the wave propagation are presented.
In the second part, a hysteretic contact model with plastic deformation and adhesion forces is used for sound propagation through fully disordered, densely packed, cohesive and frictional granular systems. Especially, the effect of friction and adhesion is examined, but also the effect of preparation history. The preparation procedure and a uniaxial (anisotropic) strain display a considerable effect on sound propagation for different states of compression and damage of the sample.

In the fifth and last chapter, the wave propagation properties are examined for a regular structure, starting from a mono-disperse distribution and slowly increasing the amount of disorder involved. The system size and the amplitude are varied, as well as the non-linearity and friction, in order to understand their effect on the wave-propagation characteristics.
In the second part of this chapter, a novel multi-mode theory for wave evolution in heterogeneous systems is presented. Wave-mode conversion, or wavenumber evolution is studied in a weakly polydisperse granular bar using DEM (Discrete Element Method) simulations. Different single (or double) discrete wavenumbers are "inserted" as initial condition for the granular packing and the system is then free to evolve. From the simulation results, parameters are extracted that are then used as input for the new theory. A better insight in the relation between the packing dimension and structure on one hand and the wave propagation behavior on the other hand is gained by calculating the eigenmodes of the packings.
Finally, the thesis is concluded by a summary, conclusions, and recommendations for further work.

2

Wave signal analysis by *Spectral Ratio Technique*

A detailed study of the dispersive behavior of a material provides much information, however difficult to extract in practice, on both the particular material itself, like the structure, the composition, etc., and the wave propagation behavior. This becomes clear as the different types and causes of dispersion - geometry, material, scattering, dissipation, and nonlinearity - are directly related to the material properties and their effect on the frequency-dependent wave propagation behavior. Experimentally, one way to characterize this dispersive behavior is to extract the frequency-dependent phase, group velocities, and attenuation effects from wave-signal records. This study is intended to explain and discuss how the Spectral Ratio Technique (SRT) can provide such a characterization and how an experimental set-up allowing for the study of a granular material like glass-beads or sand can be designed.

2.1 Introduction

The Spectral Ratio Technique (SRT), described in section 2.2, was first introduced [10] in order to extract the intrinsic attenuation, the one due to the interaction between the wave and the material only. Applied to materials that compose the different layers or strata, in an ideal description of the earth subsurface, it allows to determine their nature: rock, sandstone, sand, water, oil, etc. The objectivity of the technique, by taking a ratio and hence realizing a kind of normalization, allows to disregard the extrinsic attenuation due to the source or subsurface geometry.
In order to simplify the analysis and the treatment of the data, only a certain frequency band is considered, usually the low frequencies that correspond to large

wavelengths. As a first approximation, the intrinsic attenuation is assumed to be frequency-independent. Among the several ways to define the attenuation, the one mostly used is the quality factor Q as defined in Refs. [14, 107] and in section 2.2. Geophysicists are mostly interested in two numbers, the time-of-flight velocity and the quality factor Q. However, it is possible to extract more information like frequency-dependent quantities from the signals by applying the SRT [52,53]. Note that other techniques, like the amplitude spectrum method [86] or the phase spectrum method, which were successful to obtain group and phase velocities [91], should be described and compared to the spectral ratio technique in future work.

The goal is to determine frequency-dependent phase and group velocities and intrinsic (or specific) attenuation properties as the Q factor. This gives a way to understand in more detail the dispersion mechanisms of sound propagation in granular materials from an elegant analysis of experimental data. The interest in SRT, or in general of a detailed study of the dispersive behavior of a material, is justified by the amount of information on the material and propagation behavior that can be extracted from it. According to Sachse et al. [91], there are multiple causes of dispersion:

(1) the presence of specimen boundaries, called geometric dispersion.

(2) the frequency-dependence of effective material parameters, such as mass density, elastic moduli, dielectric constants, etc, called material dispersion.

(3) the scattering of waves by densely distributed fine inhomogeneities in a material, called scattering dispersion.

(4) the absorption or dissipation of wave energy into heat or other forms of energy in an irreversible process, called dissipative dispersion.

(5) the dependence of the wave speed on the wave amplitude called non-linear dispersion.

Most of these phenomena are enhanced in the high-frequency range, i.e., for wavelengths which are of the order of the microstructure (grain diameter), where the dispersion and the attenuation is maximal. Thus, by studying a broad frequency band, it becomes possible to extract the characteristics at low frequencies, i.e. in the quasi-static limit, and the behavior at high frequencies, which is highly dispersive. The frequency range depends largely on the application and equipment. Hence, frequencies of about 1Hz are considered in seismic applications, while frequencies in the high-sonic and ultrasonic range ($\geq$ 1kHz) are considered in laboratory experiments.
To apply the SRT, we need at least two time signals or two parts of a time signal, which are obtained differently according to the application:

A) In laboratory experiments, the signals can be obtained from two tests with

exactly the same conditions for a reference sample and the sample of interest [98, 113].

B) From the same source for two reflections separated in the time domain. This is applied for example in oil recovery applications, where the reflections at the top and at the bottom of an oil reserve are separated in time.

C) From the same sample or material where the transmitting wave is recorded at (at least) two different distances from the source, as sketched in Fig. 2.1. For example, in the field, geophysicists make use of vertical seismic profiles (VSP), which are collections of seismograms recorded from the surface to the bottom of a borehole, as input for the spectral ratio technique.

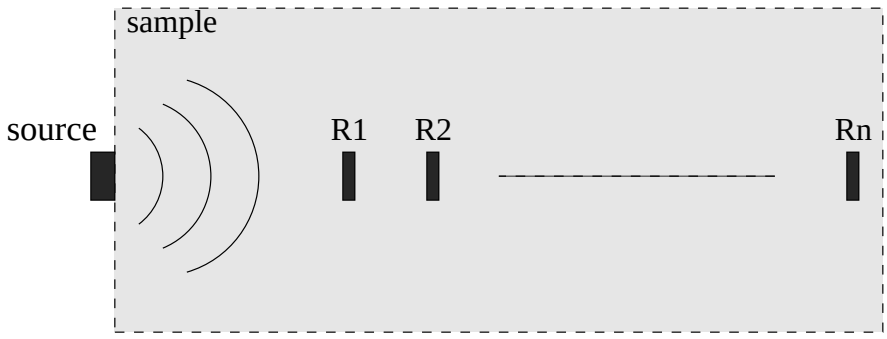

Figure 2.1: Sketch of a source and receivers (R1, R2, ..., Rn) in a configuration allowing for the application of the *spectral ratio technique*.

The SRT is most efficient for high quality signals with a large signal to noise ratio [115, 116] and also for highly lossy and dispersive materials [98]. Note that for the latter, success depends on the range of frequencies considered for the study. In laboratory experiments, the normalization has the advantage of minimizing the characteristic effects of the transducers, the transducer-sample interface and the electronic data acquisition system [98]. Tonn [115, 116] reports that the reliability of the SRT increases by enlarging the width of the investigated frequency band. Also, it is reported that, as the method is relatively fast, it allows statistical studies and hence increases the quality of the results. Finally, even if for all methods in general the reliability is decreasing with increasing noise level, the SRT seems to be more robust than other methods with respect to noise.
The advantages of the SRT cited above encourage us to use this technique in our numerical and physical experiments, even if there are some drawbacks [37]:

- In application B), described above, one needs to be able to isolate the reflections in the time domain which might not be straightforward.

- The temporal localization for the treatment of the data, even if the rectangu-

lar window seems to be the best, introduces a bias and, and possibly inconsistent zeros.

- The quality of the signal on the frequency range might be irregular, as the amplitude of higher frequencies might get close to the noise level.

- The choice of the distance between the receivers is important. A larger spacing improves the accuracy of the estimate for the attenuation, for example, by increasing the magnitude of the effect that is being measured. But this is at the expense of the spatial resolution.

In the present investigation, we are considering laboratory experiments. In this case, the configuration sketched in Fig. 2.1 is not relevant as the size of the receivers and the wavelength are of the same order. This set-up has the drawback that the measured wave field at R_{i+1} is influenced by the disturbance of the receivers R_i, R_{i-1}, etc. Therefore we consider in our study for each measurement a new sample with the desired length. The possible drawback of this set up will be discussed in section 2.4.
In the following, the SRT will be first reviewed in detail. The wave-number, the phase and group velocities and the quality factor Q are calculated. Afterwards the SRT is applied to numerical simulations results. Then it will be applied to some preliminary experimental results with sand and an outline for future experiments will be presented. Finally, some conclusions are given.

2.2 The Spectral Ratio Technique (SRT)

In a homogeneous medium the propagation of a plane harmonic wave, in the one-dimensional space $x \in \mathbb{R}^1$, can be described by

$$a(x,t) = A\,\exp[i(k\,x - \omega\,t)], \qquad \text{with} \quad \omega = 2\,\pi\,f, \tag{2.1}$$

with angular frequency ω and wavenumber k.
The complex amplitude A can be regarded as a constraint depending on various quantities like receiver/source functions, instrumental response etc., see [115,116]. However, it is not related to intrinsic attenuation [107]. If a certain form of attenuation is involved in the material, the wave-number k becomes complex and can be expressed as:

$$k = \mathrm{Re}(k) + i\,\mathrm{Im}(k). \tag{2.2}$$

The quality factor Q can be introduced as a measure of specific (also called intrinsic) attenuation

$$Q := \frac{\mathrm{Re}(k)}{2\,\mathrm{Im}(k)}, \qquad \text{or} \quad \mathrm{Im}(k) = \frac{\mathrm{Re}(k)}{2\,Q} = \frac{\omega}{2\,Q\,v_p} =: \alpha(k), \tag{2.3}$$

with the phase velocity $v_p = \omega/\mathrm{Re}(k)$. The group velocity is defined as $v_g = \partial\omega/\partial[\mathrm{Re}(k)]$.
Applying the Fourier transform $\mathcal{F}$ in time of the signals we obtain

$$F[a(x,t)] = \tilde{a}(x,\omega) = \tilde{A}(\omega)\exp(i\,k(\omega)\,x) \tag{2.4}$$

Next, we investigate two signals a_1 and a_2 at two different spatial positions x_1 and x_2 away from the source. The difference in the spatial distance is defined as $\Delta x = x_2 - x_1$. The ratio of the signals in frequency space can be written as

$$\frac{\tilde{a}_2(x_2,\omega)}{\tilde{a}_1(x_1,\omega)} = \frac{\tilde{A}_2}{\tilde{A}_1}\frac{\exp(i\,k\,x_2)}{\exp(i\,k\,x_1)} = \frac{\tilde{A}_2}{\tilde{A}_1}\exp(i\,k\,\Delta x), \tag{2.5}$$

The function g is defined as

$$g(\omega) := \ln\left(\frac{\tilde{a}_2(x_2,\omega)}{\tilde{a}_1(x_1,\omega)}\right) = \ln\left(\frac{\tilde{A}_2}{\tilde{A}_1}\right) + i\,k\,\Delta x. \tag{2.6}$$

Note that if the source is the same for the two signals, then the coefficient $\ln(\tilde{A}_2/\tilde{A}_1)$ is a constant in frequency space.

2.2.1 Phase and group velocity

Substituting equation (2.2) into equation (2.6), we obtain

$$i\,k = i\,\mathrm{Re}(k) - \mathrm{Im}(k) = \frac{1}{\Delta x}\left[g(\omega) - \ln\left(\frac{\tilde{A}_1}{\tilde{A}_2}\right)\right] =: \frac{R(\omega)}{\Delta x}. \tag{2.7}$$

From equation (2.7) we are able to calculate the attenuation $\mathrm{Im}(k)$ and the phase velocity v_p

$$\begin{aligned} \mathrm{Im}(k) &= -\mathrm{Re}(R)/\Delta x, \\ \mathrm{Re}(k) &= \mathrm{Im}(R)/\Delta x, \\ v_p &= \frac{\omega\Delta x}{\mathrm{Im}(R)}, \\ v_g &= \frac{\partial\omega}{\partial[\mathrm{Im}(R)/\Delta x]}. \end{aligned} \tag{2.8}$$

2.2.2 Phase velocity and specific attenuation Q

Starting from Eq. 2.7 and using Eq. 2.3, we observe

$$i\,\frac{\omega}{v_p} - \frac{\omega}{2\,Q\,v_p} = \frac{1}{\Delta x}\left[g(\omega) - \ln\left(\frac{A_1}{A_2}\right)\right]. \tag{2.9}$$

Assuming the special case that v_p and Q are frequency-independent, which holds for materials showing a non-dispersive behavior in a certain frequency band, the derivative of Eq. 2.7 with respect to the frequency ω becomes:

$$i\,\frac{1}{v_p} - \frac{1}{2\,Q\,v_p} = \frac{1}{\Delta x}\,\frac{\partial g}{\partial \omega}. \tag{2.10}$$

Splitting this into a real and imaginary part, leads to

$$\begin{aligned} \frac{1}{v_p} &= \mathrm{Im}\left[\frac{1}{\Delta x}\,\frac{\partial g}{\partial \omega}\right] \qquad \text{and} \\ \frac{1}{Q} &= -2\,v_p\,\mathrm{Re}\left[\frac{1}{\Delta x}\,\frac{\partial g}{\partial \omega}\right], \end{aligned} \tag{2.11}$$

which allows us to compute v_p and Q from the spectral ratio.

2.3 Numerical simulations

The SRT is now applied to time signals obtained from numerical simulations, where rather idealized conditions should lead to high-quality results. Indeed, the issues encountered in real experiments as source-receivers characteristics, source-sample and receiver-sample coupling, transfer between electrical and mechanical energy, or noise, are not relevant in the simulations. However, the relevance of the model with respect to reality is, of course, another issue.
In the following, a DEM (Discrete Element Model), see section 4.1.2, is used in order to simulate sound waves through a dense regular packing of grains. The wave agitation and the signal recording procedure are both described in detail in section 4.1.3. We will now discuss the results of two different types of waves. First, P- and S-waves in a purely elastic (frictionless) granular packing and secondly a P-wave in an inelastic packing with contact viscosity (dashpot model), see section 4.1.3.

For the P-wave, several graphs are plotted in Fig. 2.2. The two time signals are recorded at 10 and 30 layers ($d \sim 14$ and 42 cm) from the source, see Fig. 2.2 a). Their power spectra are calculated with an FFT algorithm using Matlab, see Fig. 2.2 b). The power spectra, identical for both signals, indicate the "relevant" frequency range. That is, from the lowest frequency allowed by the time window width, ~ 1 kHz, to the frequency where both spectra have a significant amplitude, ~ 50 kHz. The latter corresponds to the highest possible frequency in the system in the considered propagation direction (z), based on the oscillation of a layer. The SRT is then applied, using both spectra. This gives the real part of the

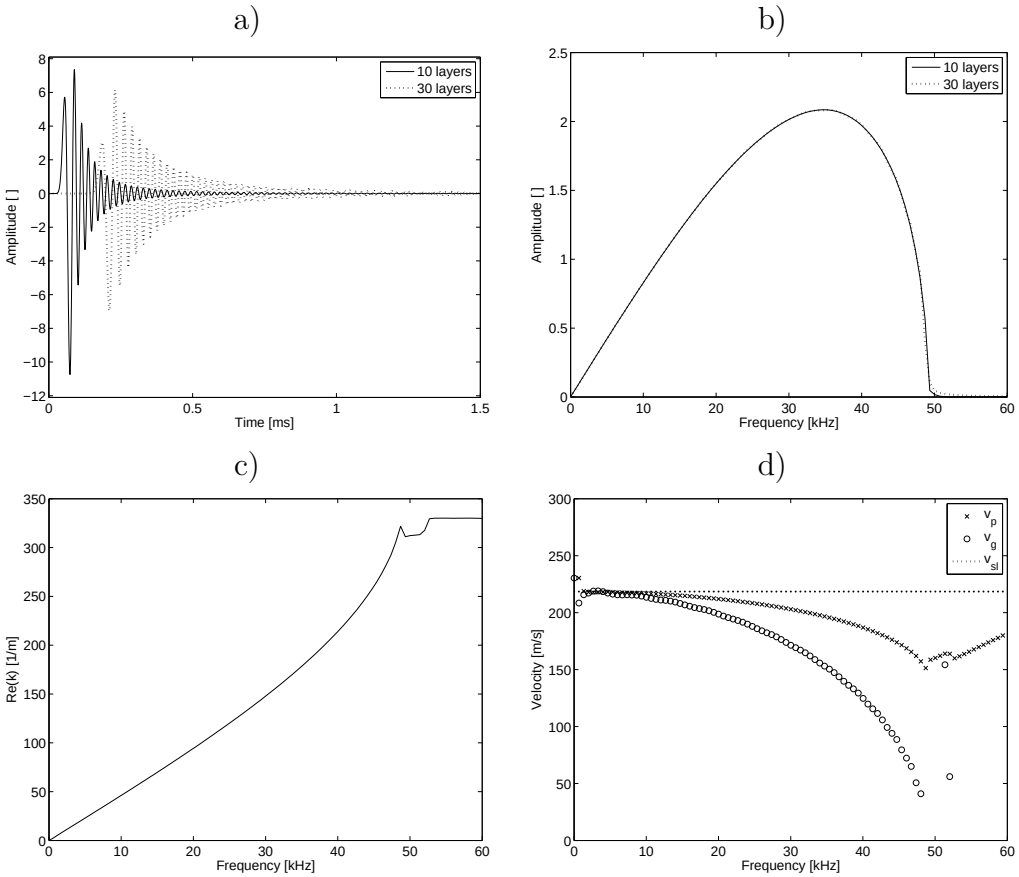

Figure 2.2: a) the time signals, b) the power spectrum, c) the real part of the wave-number and d) the phase and group velocities, for a P-wave. The time signals are recorded at 10 and 30 layers ($d \sim 14$ and 42 cm) away from the source.

wave-number $\mathrm{Re}(k)$ as function of frequency, see Fig. 2.2 c). This relation is nothing else than another way to describe the dispersion behavior of the packing considered. This result is identical to the dispersion relation obtained elsewhere by different methods from detailed simulation data, see Sec. 4.1.3. From $\mathrm{Re}(k)$, using the definitions given in section 2.2, ($v_p = \omega/\mathrm{Re}(k)$ and $v_g = \partial\omega/\partial[\mathrm{Re}(k)]$) it is possible to extract the phase v_p and the group velocity v_g, see Fig. 2.2 d). Those velocities are identical to the theoretically calculated velocity in the quasi-static limit v_{sl} (dotted line in Fig. 2.2 d)), see section 4.1.3 for low frequency, as expected. The deviation from the large wavelength limit (low frequency) is clearly visible for shorter wavelengths (high frequencies). The most powerful aspect of this method is that only two time signals were needed to obtain the same information as derived in section 4.1.3 with numerous time signals. As no attenuation is present in this numerical simulation, the imaginary part of the wave-number $\mathrm{Im}(k)$ and the inverse quality factor Q^{-1} are negligible.

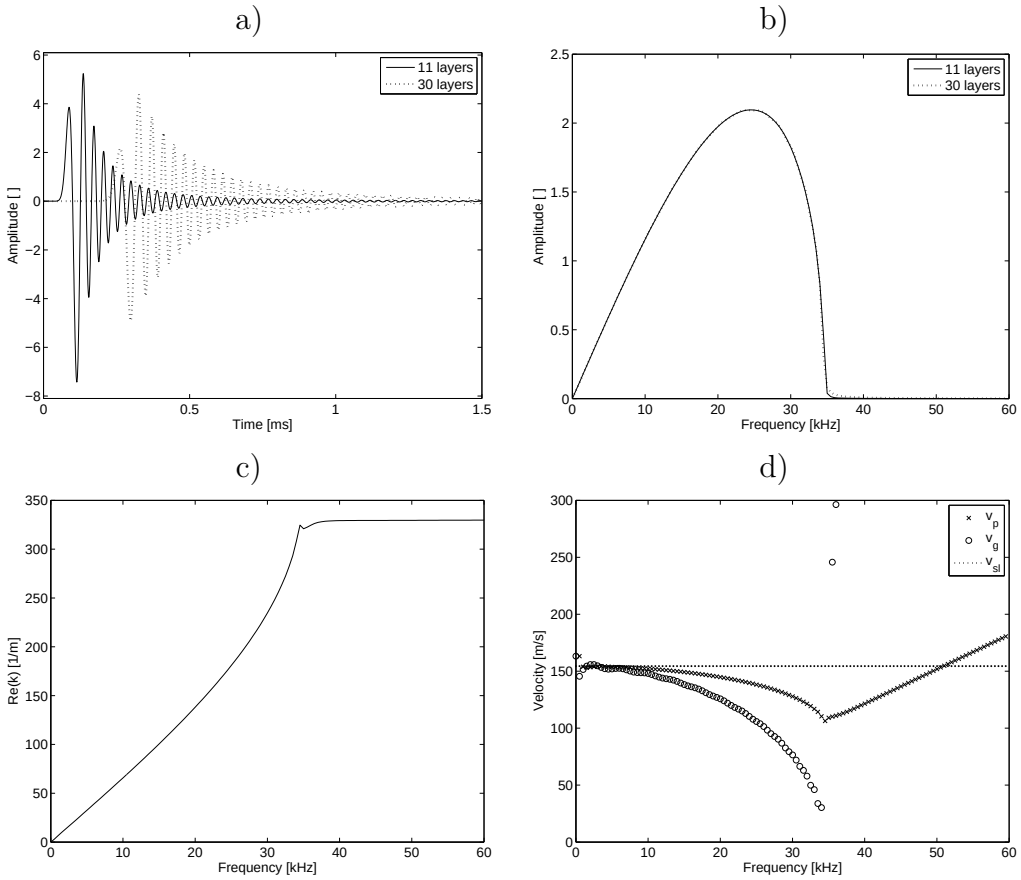

Figure 2.3: a) the time signals, b) the power spectrum, c) the real part of the wavenumber and d) the phase and group velocities, for a S-wave. The time signals are recorded at 11 and 30 layers ($d \sim 15$ and 42 cm) away from the source.

For the S-wave, the same type of graphs are plotted in Fig. 2.3. The differences with the P-wave are the same as observed in Sec. 4.1.3. The relevant frequency range is smaller, from ~ 1 kHz to ~ 35 kHz. This is a consequence of a smaller effective tangential stiffness as compared to the normal effective stiffness for this propagation direction (z). Both phase and group velocities, v_p and v_g, are smaller ($\approx \sqrt{2}$ times, see section 4.1.3) than for the P-wave. Otherwise, no other qualitative differences are observed. It is however remarkable that for low frequencies the results obtained for Re(k) are quite unstable in regard to the choice of the distance to the source for the time signal (data not shown here). A more detailed study should determine the exact causes for this effect.

The frequency-dependence of the viscous damping, which was introduced in the third simulation (P-wave with damping), shows an increasing attenuation for increasing frequencies. In Fig. 2.4 a), one can observe in the time signals the absence of the coda, which contains the high frequencies as observed in the

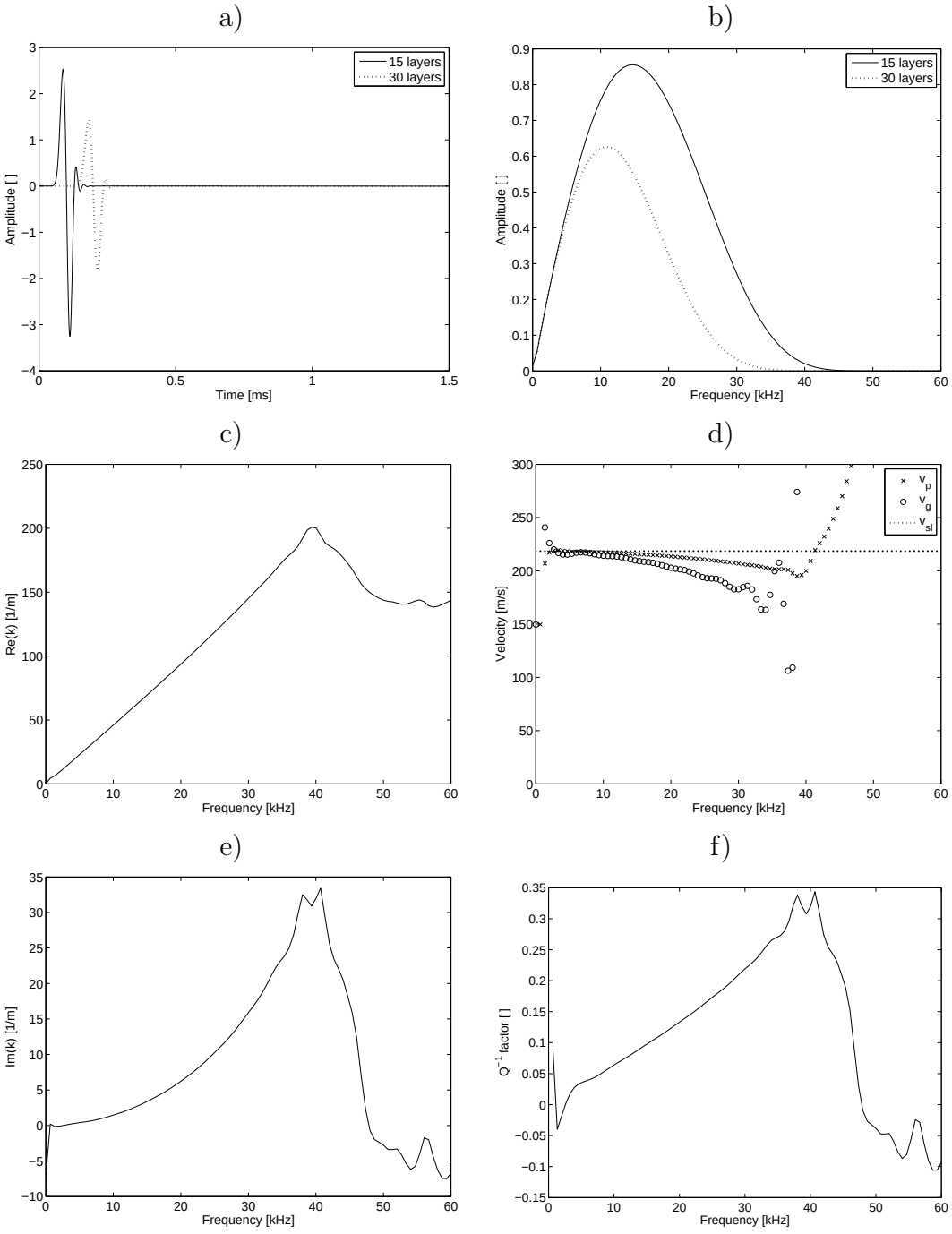

Figure 2.4: a) the time signals, b) the power spectrum, c) the real part of the wavenumber, d) the phase and group velocities, e) the imaginary part of the wavenumber and f) the inverse quality factor Q^{-1}, for a P-wave with damping. The time signals are recorded at 15 and 30 layers ($d \sim 21$ and 42 cm) away from the source.

simulations without damping. In Fig. 2.4 b) the power spectra lead to the same observation. For low frequencies the spectra of the two signals are identical. They deviate from each other from five kHz on. Also, as a consequence of damping, the highest relevant frequency is reduced to $\sim$ 30 kHz. Indeed, from that frequency on, the amplitude of the second signal spectrum is too low to be significant. With respect to that, within the reduced frequency range, one can see from Fig. 2.4 c) and d) that Re(k), v_p and v_g are similar to those in the simulation without damping (Fig. 2.2). Finally, the fact that the high frequencies are more strongly damped than the lower ones is qualified and quantified by both Im(k) and Q^{-1} in Fig. 2.4 e) and f). While Im(k) shows a clear non-linear increase of the damping for increasing frequencies, this non-linearity is almost not visible for the inverse quality factor Q^{-1}.

Unfortunately, the application of the SRT on the slightly polydisperse packings as used in section 4.1 and 5 did not lead to results with a comparable quality to those in the regular case. It seems that the influence of the source on one hand and a too short time window on the other hand are responsible for large scattering in the data. A longer packing, allowing to record the signals at a far enough distance away from the source and for sufficiently long time, should improve the results. Also, a larger packing section $(x-y)$, and averaging the signals for many different polydisperse packings (with respect to the random assignment of radii to the particles), would lead to much better statistics. Therefore, further investigations are needed in order to improve the numerical set-up and procedure, and to obtain the desired quality of results.

2.4 Physical experiments

2.4.1 Preliminary investigations

With the goal of first understanding the dispersive behavior of dry granular material (dry sand or glass beads) and later soils in general, many preliminary investigations have been done, with the use of the SRT. Some aspects of the results are discussed below.

Several types of piezoelectric transducers were tested in several configurations. The elementary set-up used for the tests is a rectangular box filled with loose river sand or glass beads. First, Panametrics ultrasonics piezoelectric transducers (V101) with a central frequency of 500 kHz were tested. As a first observation, the results (data not shown here) showed a large shift in frequency between the source spectrum, around 500 kHz, and the spectrum of the received signals, around 20 kHz after the wave traveled through a few centimeters of the material.

This typical phenomenon, due to the highly dispersive behavior of (loose) (dry) granular materials, is also reported elsewhere [58]. In view of the application of the SRT, two signals recorded at two different distances from the source are needed, as explained in section 2.1. However, to do so, the transducers (source and receiver) have to be placed at different distances from each other, implying emptying and refilling the box. This manipulation, especially in granular materials, needs to be extremely well controlled with respect to the material density and the confining stress, for example, to obtain a good reproducibility of the measurements. Placing at the same time two (at least) pairs of transducers in the box allows us to avoid this manipulation. However, this does not help if statistics over several measurements are needed, as new sample configurations are needed anyway. Also, the asymmetry present in the box increases the inhomogeneity of the system and hence the objectivity of the measurements with respect to each pair of transducers.

As a general remark, the shift in frequency, described above, lead to a very high noise level of the received signals, as not enough energy is transferred from the source to the receiver. This makes the results practically useless for the spectral ratio technique. One solution to this problem is to use transducers that emit and receive lower frequencies.

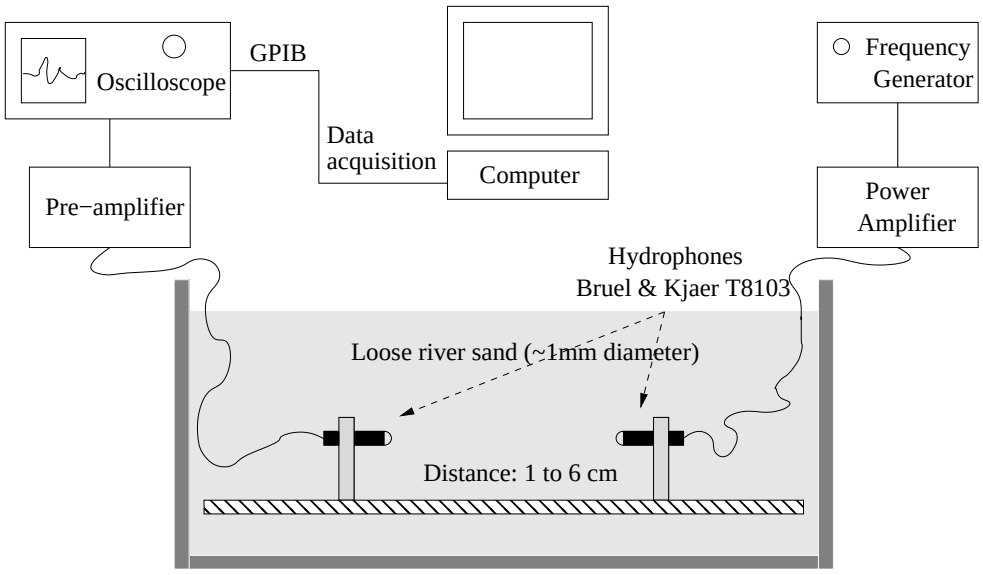

Figure 2.5: The set-up used for the preliminary experiments

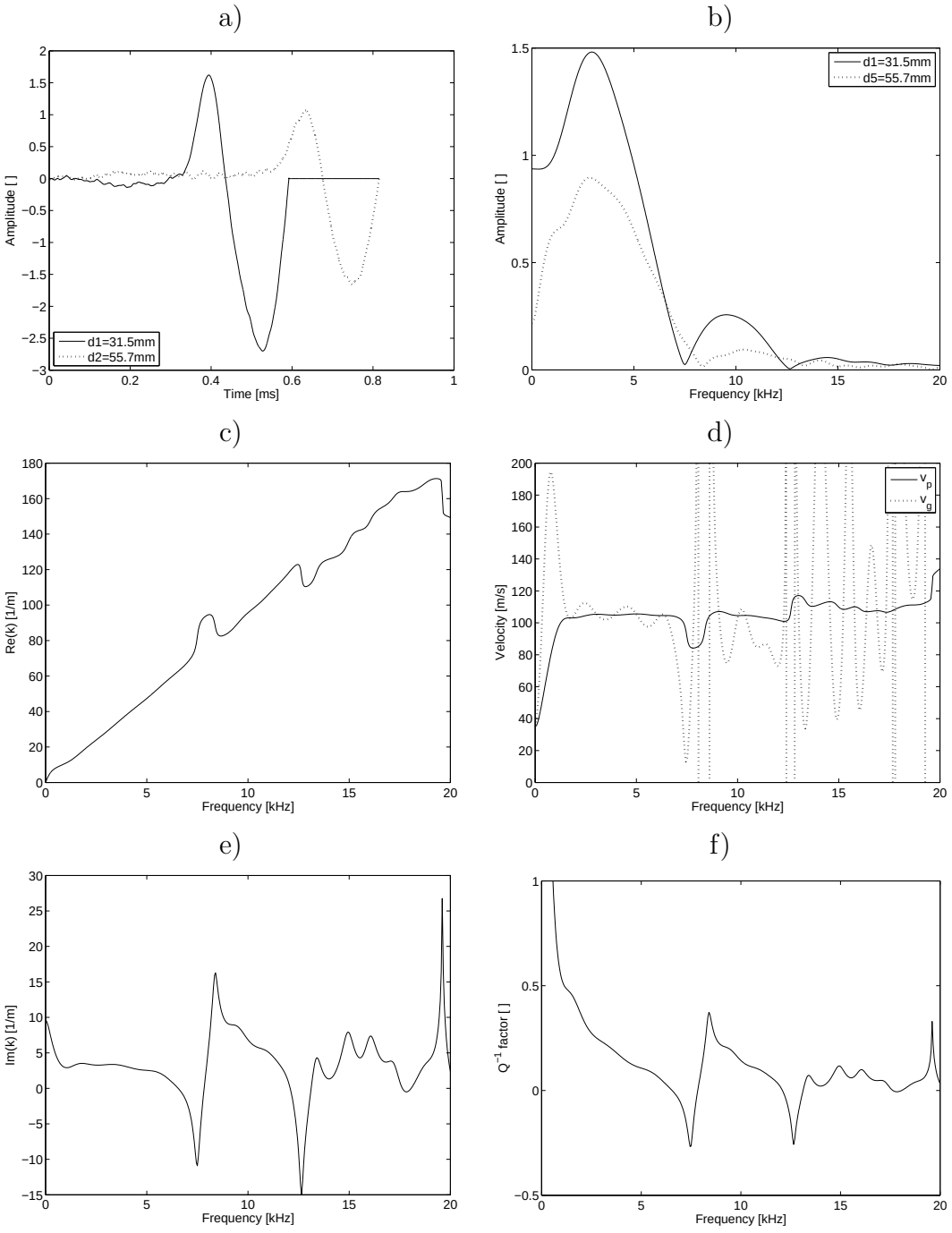

Figure 2.6: a) Two time signals at distance $d1$, and $d2$, b) their power spectrum, c) the real part of the wave-number, d) the phase and group velocities, e) the imaginary part of the wave-number and f) the inverse quality factor Q^{-1}. The time signals are recorded at distances $d = 31.5$ and 55.7 mm away from the source.

2.4.2 Results from the actual set-up

In the results presented in the following, finger-like hydro-phones, Bruel & Kjaer T8103, with a wide band around $\sim$ 10 kHz, were tested.
As in the preliminary investigations, the simple set-up consists of two hydrophones immersed in a box filled with loose river sand with a sharp size distribution, around 1mm diameter, see Fig. 2.5. The transducers are opposing each other in a frontal way. A set of measurements has been performed placing the transducers at different distances (d = 14, 22.5, 31.5, 45 and 55.7 mm). For each distance, the source signal is a sinusoidal pulse of one period with a chosen frequency (ω = 3, 4, ... , 12, 13, 15 and 20 kHz).
The SRT has been applied to the different signals and the two signals recorded at d = 31.5 and 55.7 mm away from the source are presented, see Fig. 2.6. The time signals, Fig. 2.6 a) are "cut" after the first oscillation in order to exclude any reflections. This arbitrary choice, which leads to the flat part (padding with zeros) in Fig. 2.6 a) in order to keep a fixed time window, might introduces undesirable effects. However, this choice was preferred to the one where reflections can be present. From the frequency spectrum, Fig. 2.6 b), it can be observed that the relevant frequency range, where the amplitudes are significantly high, is: 2 to 5 kHz and 8 to 12 kHz. The real part of the wave-number, Fig. 2.6 c), allows to extract approximate phase and group velocities, which are about 100 m/s. Attenuation, see Fig. 2.6 e) and f) can not be interpreted with respect to the signal to noise level.

2.4.3 A proposed improved set-up

The outcome of those preliminary experimental results is only a partial success. Even though encouraging, the room for improving the set-up is very large. The sample preparation needs to follow a strict procedure allowing for a good homogeneity of stress and density in the packing. Taking the transducers out of the sample would facilitate this. The boundary conditions must be controlled seriously. The contact interface between sand and transducers must be enhanced.
Considering all these points and also useful discussions with A. Merkel, V. Tournat and V. Gusev during a one-week stay at the laboratory of Acoustics in Le-Mans in France led to a design for an improved set-up and sample preparation procedure.

The use of low frequency piezoelectric transducers with a central frequency of 100 kHz (Panametrics contact transducers V1011), seems to offer many advantages. A nice and large contact interface between the transducers and the sand is

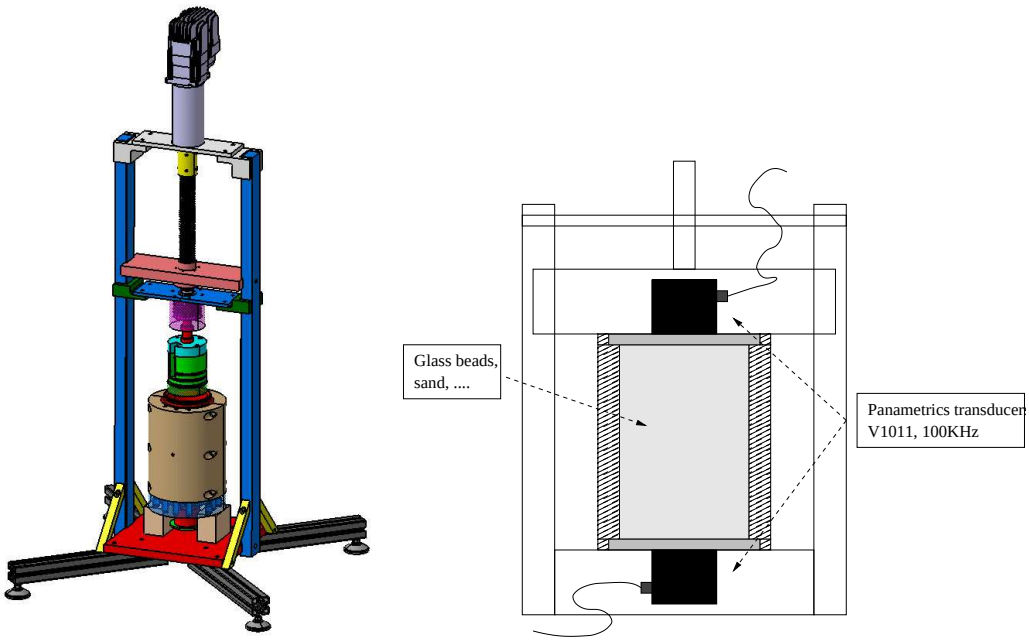

Figure 2.7: Sketch of a set-up for future experiments, see Ref. [55] for more details.

needed for a good coupling, especially crucial for loose sand or tests with a small confining pressure. The flexibility of the transducers allows to emit with high enough energy and precision signals with frequencies up to 200 kHz and down to one kHz. Inspired by other experimental set-ups [48, 118], a cylindrical cell will be used in order to better control the boundaries, see Fig. 2.7. The challenge in those experiments will be to avoid reflections, to achieve a high reproducibility of the samples and to accurately control the distance between the two receivers. The sample reproducibility seems to be the most critical point. Averaging over many sample configurations will filter out the high-frequency configuration-dependent effects. The objective is that this procedure will allow us to extract a general trend in the dispersion behavior beyond the range of the large wavelength limit.

2.5 Conclusions

The SRT has been presented and discussed. Interest in the technique is based on the objective to gain a better understanding of dispersion in granular materials in general and in sand in particular. Especially the possibility to extract frequency-dependent phase and group velocities and attenuation properties of the material is attractive.

The SRT has been successfully applied to numerical DEM simulation results for regular granular packings. In order to obtain the same high-quality results for polydisperse packings extra investigations are needed. For example, the packing size must be increased, in order to avoid source effects and too short time windows.
Promising experimental results have been presented, allowing us to propose the design of an improved set-up for which intensive investigations will be performed in near future, see [55].

3

Dispersion with rotational degrees of freedom

The goal of this chapter is to investigate the influence of rotational degrees of freedom on the dispersion behavior of acoustic waves in regular granular packings with tangential elasticity at the inter-particle contact. The study includes both theoretical and numerical approaches.

3.1 Introduction

The theoretical analysis of lattices with respect to vibrational (or acoustical) modes is quite common and can be found in many studies on crystals [6,30,76,79], Fewer studies are found that are related to the dispersion relation in frictional granular materials with tangential elasticity. Schwartz et al [96] derive the dispersion relations for regular and disordered packings including rotational degrees of freedom, which according to them should be treated on an equal footing with the translational degrees of freedom. As an illustration, their results obtained with a spin set to zero show an un-physical behavior in the static limit: the compressive and the shear wave have the same velocity, which is in that case in contradiction with continuum elasticity theory.

Mühlhaus et al [83] derived the dispersion relations for compressive and shear waves in a granular material within a continuum model framework including micro-rotations (Cosserat type continua). They observe that the rotational degrees of freedom allow the existence of two coupled branches (modes) in the dispersion relation where in one mode the main carrier of the energy are the displacements (shear) and in the other mode the main carrier are the grain rotations.

Some more recent theoretical work by Suiker et al, [104, 105] shows dispersion relations in a two-dimensional hexagonal lattice with sliding and also rolling resistance. It is shown that the results match with both Cosserat and high-order gradient continua approaches in the static limit.
Some other theoretical and experimental works on regular structures of grains, deriving dispersion relations and considering non-linear contact laws (Hertz-Mindlin) can be found in Refs. [23, 75, 121].

In this study, the modeling of tangential contact elasticity is examined with respect to its effect on the dispersive behavior of regular granular packings by comparing numerical simulation results to theoretical predictions. The latter are derived in section 3.2 of this chapter. In section 3.3, the numerical simulation results are obtained by the analysis of different transient waves through a regular FCC (Face Centered Cubic) lattice granular material with rotational degrees of freedom.

3.2 Harmonic wave analysis of a lattice

In this section, the vibrational modes of a three-dimensional lattice are determined. First, some definitions are given. Then, starting from Newton's equations of motion and the balance of angular momentum, which are realized for each particle in the lattice, a harmonic wave solution is considered. This leads to a generalized eigenvalue problem, which is solved numerically. Finally, the eigenvalues of the lattice are then presented via the so-called dispersion relation.

3.2.1 Inter-particle contact elasticity

Particle geometry and kinematics In the following, spherical particles of radius a are considered with a mass m, and a moment of inertia $I = qma^2$ (with $q = 2/5$ for a spherical particle in three dimensions). In the coordinate system (x, y, z), the position of particle p is given by the vector $\boldsymbol{r}^p$. Particles are considered to be rigid bodies with translational and rotational degrees of freedom.

The translational movement of the center of mass of particle p in time is described by the displacement vector $\boldsymbol{u}^p$. In the following $\dot{\boldsymbol{u}}^p$ and $\ddot{\boldsymbol{u}}^p$, with the dots denoting the time derivative, are the velocity and the acceleration of particle p, respectively. The rotation of the particle around its center of mass is characterized by the vector $\boldsymbol{\varphi}^p$, where $\boldsymbol{\varphi}^p = \varphi^p(\hat{\varphi}_x^p, \hat{\varphi}_y^p, \hat{\varphi}_z^p)$, with $\varphi^p = |\boldsymbol{\varphi}^p|$, and the unit vector $\hat{\boldsymbol{\varphi}}^p$ denotes the corresponding axis. The magnitudes of rotation are chosen to

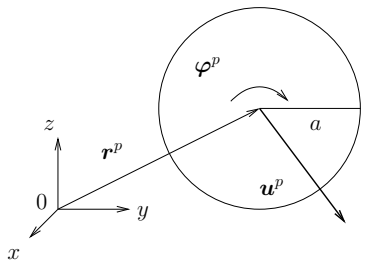

Figure 3.1: Particle geometry and kinematics.

be zero at time zero. In the same way as for the translational movement, $\dot{\boldsymbol{\varphi}}^p$ and $\ddot{\boldsymbol{\varphi}}^p$ designate the angular velocity and the angular acceleration, respectively. Those definitions are graphically represented in Fig. 3.1, where the curly arrow indicates that $\hat{\boldsymbol{\varphi}}^p$ points into the plane in direction of view and the particle rotates clockwise (negative rotation).

Contact geometry We now consider two particles, p and q in contact with each other at the point c. The translational and rotational movements of the particle in contact are described by $\boldsymbol{u}^q$ and $\boldsymbol{\varphi}^q$. The vector that connects the center of particle p and the contact point c is called the semi-branch vector, which also defines the normal direction at contact c. As all particles have the same radius a, one has $\boldsymbol{l}^{pc} = -\boldsymbol{l}^{qc} = \boldsymbol{l}^c$ for the particles p and q, see Fig. 3.2.

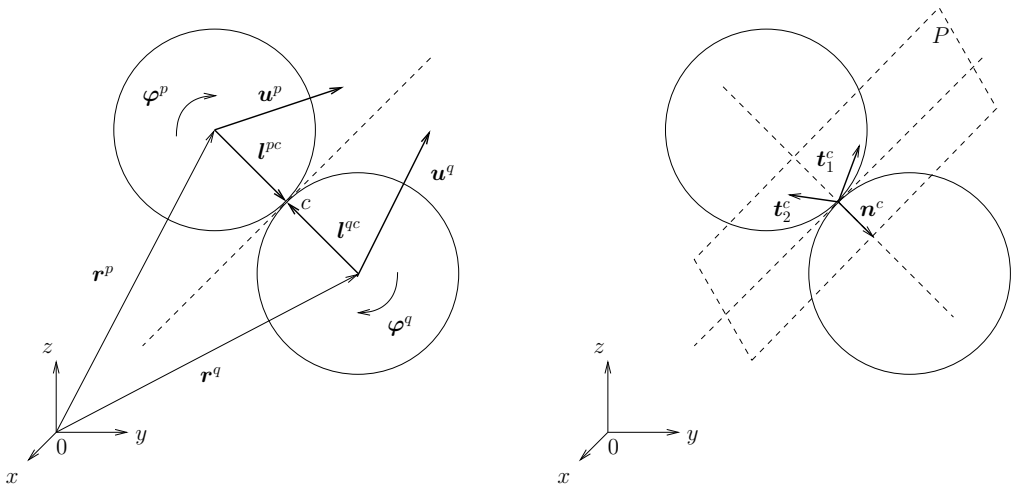

Figure 3.2: Contact interaction between two particles (left) and tangential plane P (right)

Relative displacements at the contact The vectors $\boldsymbol{u}^p$ and $\boldsymbol{u}^q$ are the particle center displacements, and their difference contributes to the relative displacement at the contact,

$$\boldsymbol{\Delta}^c = \boldsymbol{\Delta}^{pq} = (\boldsymbol{u}^q - \boldsymbol{\varphi}^q \times \boldsymbol{l}^c) - (\boldsymbol{u}^p + \boldsymbol{\varphi}^p \times \boldsymbol{l}^c) \tag{3.1}$$

which is here defined as the motion of q relative to p (with $\boldsymbol{\Delta}^{qp} = -\boldsymbol{\Delta}^{pq}$). In the same spirit, the particle rotations contribute to the tangential displacement.

Particle interactions The contact law defines the interaction between the two particles by relating the force to the relative displacement. The chosen law here is linear elastic, meaning that no particle rearrangement, separation, or irreversible sliding is allowed (which is equivalent to a mass-spring system). Note that therefore stiff particles, with point wise contact, are considered and only very small deformations are allowed. The contact force acting on particle p at contact c can be written as:

$$\boldsymbol{f}^c = \boldsymbol{S}^c \cdot \boldsymbol{\Delta}^c, \tag{3.2}$$

with the stiffness matrix as:

$$\boldsymbol{S}^c = k_n \boldsymbol{n}^c \boldsymbol{n}^c + k_{t_1} \boldsymbol{t}_1^c \boldsymbol{t}_1^c + k_{t_2} \boldsymbol{t}_2^c \boldsymbol{t}_2^c. \tag{3.3}$$

Using the expression for the unit tensor $\boldsymbol{I}^3 = \boldsymbol{n}^c \boldsymbol{n}^c + \boldsymbol{t}_1^c \boldsymbol{t}_1^c + \boldsymbol{t}_2^c \boldsymbol{t}_2^c$, where $\boldsymbol{n}^c$ is the unit vector in the normal direction (colinear to the branch vectors), and $\boldsymbol{t}_1^c$ and $\boldsymbol{t}_2^c$ (orthogonal to each other) are tangential unit vectors in the plane P orthogonal to $\boldsymbol{n}^c$, see Fig. 3.2 and choosing an isotropic tangential stiffness $k_{t_1} = k_{t_2} = k_t$ we obtain:

$$\boldsymbol{S}^c = k_t \boldsymbol{I}^3 + (k_n - k_t) \boldsymbol{n}^c \boldsymbol{n}^c \tag{3.4}$$

where k_n is the stiffness in the normal direction and k_t the tangential stiffness. Those stiffnesses can be obtained from the particle properties and some mechanical tests with two particles.

3.2.2 A generalized eigenvalue problem

Equations of motion: The starting point are the conservation laws for linear momentum (Newton's second law) and angular momentum

$$m\ddot{\boldsymbol{u}}^p = \sum_{c=1}^{C} \boldsymbol{f}^c \ , \quad \text{and} \quad I\ddot{\boldsymbol{\varphi}}^p = \sum_{c=1}^{C} \boldsymbol{\tau}^c \tag{3.5}$$

with $\boldsymbol{\tau}^c = \boldsymbol{l}^c \times \boldsymbol{f}^c$ the torque created by the force $\boldsymbol{f}^c$.

Forces and torques are now formally expressed in a single equation

$$\boldsymbol{M} \cdot \ddot{\boldsymbol{U}} = \sum_{c=1}^{C} \boldsymbol{F}^c \tag{3.6}$$

with $\boldsymbol{M}$ the generalized mass-inertia matrix, $\boldsymbol{F}^c$ the generalized force-torque vector and $\boldsymbol{U}$ the generalized displacement (translation/rotation) vector. These are given by:

$$\boldsymbol{M} = \begin{pmatrix} m\boldsymbol{I}^3 & \boldsymbol{0}^3 \\ \boldsymbol{0}^3 & I\boldsymbol{I}^3 \end{pmatrix}, \; \boldsymbol{U} = \begin{pmatrix} \boldsymbol{u} \\ \boldsymbol{\varphi} \end{pmatrix} \text{ and } \boldsymbol{F}^c = \begin{pmatrix} \boldsymbol{I}^3 \\ \boldsymbol{R}^{\times c} \end{pmatrix} \cdot \boldsymbol{f}^c \tag{3.7}$$

with $\boldsymbol{I}^3$ the identity matrix in three dimension (3x3) and $\boldsymbol{R}^{\times c}$, also a (3x3) matrix, such that $\boldsymbol{R}^{\times c} \cdot \boldsymbol{v} = \boldsymbol{l}^c \times \boldsymbol{v}$, $\forall$ vectors $\boldsymbol{v}$:

$$\boldsymbol{R}^{\times c} = \begin{pmatrix} 0 & -\boldsymbol{l}_z^c & \boldsymbol{l}_y^c \\ \boldsymbol{l}_z^c & 0 & -\boldsymbol{l}_x^c \\ -\boldsymbol{l}_y^c & \boldsymbol{l}_x^c & 0 \end{pmatrix}. \tag{3.8}$$

Harmonic wave solution: Assuming that the generalized displacements of the particles, $\boldsymbol{U}(\boldsymbol{r}, t)$, are harmonic oscillations, $\boldsymbol{U}(\boldsymbol{r}, t)$ is given by

$$\boldsymbol{U}(\boldsymbol{r}, t) = \boldsymbol{U}_0 \cdot e^{i(\omega t - \boldsymbol{k}\cdot\boldsymbol{r})} = \begin{bmatrix} \boldsymbol{u}_0 \\ \boldsymbol{\varphi}_0 \end{bmatrix} \cdot e^{i(\omega t - \boldsymbol{k}\cdot\boldsymbol{r})} \tag{3.9}$$

with $\boldsymbol{u}_0$ and $\boldsymbol{\varphi}_0$ the translational displacement and rotational spin amplitudes, $\boldsymbol{k}$ wave vector, ω frequency and t time.

The relative displacement at contact c, together with equations (3.1) and (3.9) and using $\boldsymbol{r} = \boldsymbol{r}^p$ and $\boldsymbol{r}^q \approx \boldsymbol{r}^p + 2a\boldsymbol{n}^c$ (true for high k_n), becomes:

$$\boldsymbol{\Delta}^c = -\left[(1 - e^{-i2a\boldsymbol{k}\cdot\boldsymbol{n}^c})\boldsymbol{u}_0 - (1 + e^{-i2a\boldsymbol{k}\cdot\boldsymbol{n}^c})\boldsymbol{l}^c \times \boldsymbol{\varphi_0}\right] e^{i(\omega t - \boldsymbol{k}\cdot\boldsymbol{r}^p)} \tag{3.10}$$

which can be rewritten as:

$$\boldsymbol{\Delta}^c = -\boldsymbol{D}^c \cdot \boldsymbol{U}_0 \cdot e^{i(\omega t - \boldsymbol{k}\cdot\boldsymbol{r}^p)} \tag{3.11}$$

where the (3x6) matrix $\boldsymbol{D}^c$ is defined as

$$\boldsymbol{D}^c = [(1 - e^{-i2a\boldsymbol{k}\cdot\boldsymbol{n}^c})\boldsymbol{I}^3 \quad - (1 + e^{-i2a\boldsymbol{k}\cdot\boldsymbol{n}^c})\boldsymbol{R}^{\times c}]. \tag{3.12}$$

The sum of all force-torque vectors, using (3.2), (3.7) and (3.11), reads:

$$\sum_{c=1}^{C} \boldsymbol{F}^c = -\sum_{c=1}^{C} \left[\begin{pmatrix} \boldsymbol{I}^3 \\ \boldsymbol{R}^{\times c} \end{pmatrix} \cdot \boldsymbol{S}^c \cdot \boldsymbol{D}^c \right] \cdot \boldsymbol{U}_0 \cdot e^{i(\omega t - \boldsymbol{k}\cdot\boldsymbol{r}^p)} \tag{3.13}$$

Using (3.9), the generalized acceleration, $\ddot{\boldsymbol{U}}$, equals

$$\ddot{\boldsymbol{U}} = -\omega^2 \cdot \boldsymbol{U}_0 \cdot e^{i(\omega t - \boldsymbol{k}\cdot\boldsymbol{r}^p)}, \tag{3.14}$$

Finally, using (3.13), (3.14),

$$\boldsymbol{K} = \sum_{c=1}^{C} \left[\begin{pmatrix} \boldsymbol{I}^3 \\ \boldsymbol{R}^{\times c} \end{pmatrix} \cdot \boldsymbol{S}^c \cdot \boldsymbol{D}^c \right], \tag{3.15}$$

and the equation of motion (3.6), we obtain,

$$\left[\boldsymbol{K} - \omega^2 \boldsymbol{M}\right] \cdot \boldsymbol{U}_0 = \boldsymbol{0} \tag{3.16}$$

This is a generalized eigenvalue problem with eigenvalues ω^2 and corresponding eigenvectors $\boldsymbol{U}_0$. Note that $\boldsymbol{K}(\boldsymbol{k})$ explicitly depends on the wavenumber $\boldsymbol{k}$, via Eq. (3.12).

3.2.3 Results

The obtained generalized eigenvalue problem (3.16) can be solved numerically. This problem can also be solved analytically, for special cases. Different symmetries of a lattice can make it possible to find an analytical solution. However, further investigations are needed before such analytical solutions can be presented.

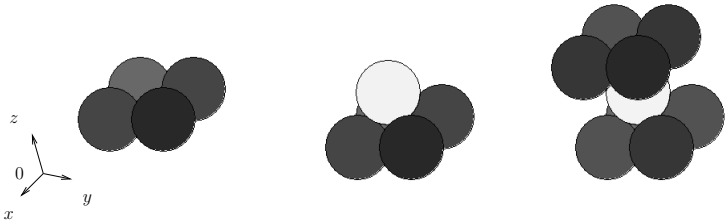

Figure 3.3: Detail of the Face Centered Cubic (FCC) lattice: square layers are piled up in a A-B-A-B sequence with the B-layer being shifted by $(a, a, \sqrt{2}a)$ as compared to the A-layer.

Lattice The first step is to choose a lattice. As we wish to compare directly the analytical and the simulation results (Sec. 3.3), the same Face Centered Cubic lattice (FCC) is chosen. The structure of the FCC lattice is described in Fig. 3.3. Each particle represents a unit-cell with 12 contacts. It has four contacts in the x-y-plane and four above and below.

Material parameters The material parameters are chosen identically to those of the simulations (Sec. 3.3). The radius $a = 0.001$ m, the normal stiffness $k_n = 10^5$ kg/s^2 and the material density $\rho = 2000$ kg/m^3. The tangential stiffness is given by the ratio k_t/k_n, for which different values are considered. The wavevector chosen is quantified by $\boldsymbol{k} = (0, 0, k)$.

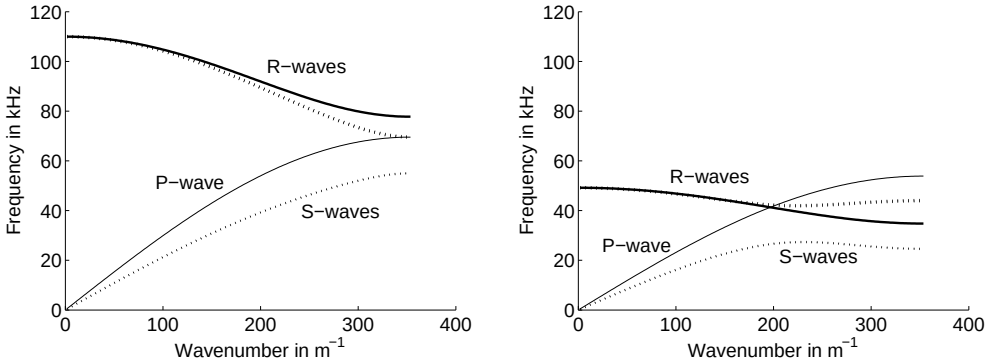

Figure 3.4: Dispersion relation $f(k)$, frequency as function of the wavenumber for two different k_t: (left) $k_t/k_n = 1$ and (right) $k_t/k_n = 1/5$. Six modes are observed, one purely translational compressive, two with strong shear and three with strong rotation amplitudes.

Dispersion relation The numerical result provides six eigenfrequencies and six eigenvectors for each given wavenumber k. The value six corresponds to the number of degrees of freedom present in the problem, three translations and three rotations. By plotting the obtained eigenfrequencies against the corresponding wavenumbers, we get the dispersion relation, see Fig. 3.4. Each branch corresponds to a mode. We observe one compressive (purely translational), two shear and three rotation modes. Due to the $x - y$ lattice symmetry, two shear modes and two of the rotation modes are identical (degenerate modes).

The compressive mode is given by the thin solid line and the two identical shear modes (x and y polarization) are given by the thin dotted lines. While for $k_t/k_n = 1$, the branches are relatively well separated, except for the smallest k, in the case of $k_t/k_n = 1/5$ the branches clearly cross each other as the tangential stiffness is five times lower. Hence, the corresponding eigenvalues are smaller too.

Also, a qualitative difference is observed as the degenerate shear and rotation modes (thin and thick dotted lines) are distorted for large wavenumber (small wavelength). The distortion in both cases (shear and rotation) starts (inflexion point) at around $k = 225$ m^{-1}. This underlines the expected strong coupling

between shear and rotation modes. Indeed, for example the x-polarized shear mode corresponds to a movement of the particles in the x-direction and if the displacements from layer to layer are different, particles rotate around the y-axis. An examination of the eigenvectors allows us to characterize the different modes as, for example, the coupling between the shear and rotation modes. However further investigations are needed for a complete understanding. In Fig. 3.4, the rotation modes are plotted with a thicker line. The thick solid line shows the rotation mode where the particles rotate around the z axis, and the two superimposed thick dotted lines show the rotation modes where the particles rotate around the x- and y-axis.
In the next section, these results are compared to the simulation results.

3.3 Comparison with simulations

A discrete element method (DEM) is used in order to simulate wave propagation through a dense packing with the same characteristics as theoretically investigated in the previous section. The method, the packing, the wave excitations and the signal analysis are described. Finally the results are compared to those of the previous section.

DEM model The model is based on solving the balance equations, for translational and rotational degrees of freedom, for each particle at each time-step of the simulation. The forces are determined by contact laws. In this case, the normal contact follows the simple linear spring model: $|f| = k_n\delta$ ($\delta = \mathbf{\Delta}_n^c$ in the previous section), with k_n the contact stiffness and δ the particle overlap. Tangential elasticity is introduced at the contacts between particles according to $f_t = k_t\Delta_t$, with f_t the contact force in the tangential direction. The chosen friction coefficient $\mu = 0.5$ is large enough to avoid sliding at the contact as the imposed wave amplitude is very small. The system is first prepared without friction such that $f_t = 0$ at $t = 0$. As soon as displacements and deformations occur, f_t can become non-zero. More details concerning the model are given in Sec. 4.1.2.

Initial packing The wave propagation simulations are performed on a dense, static packing of grains arranged in a Face Centered Cubic (FCC) structure (density ≈ 0.74), where square layers in the $x - y$ plane (4x4 particles) are stacked densely in the z-direction (200 layers), see Fig. 3.5. More details concerning the packing configuration are given in Sec. 4.1.2.

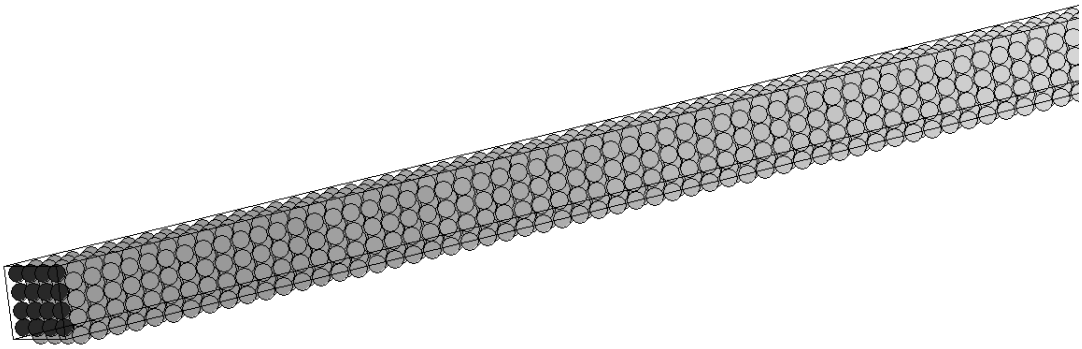

Figure 3.5: Face centered cubic (FCC) packing, thin (4x4 particles, periodic) in the $x-y$ directions, and elongated (200 layers, non-periodic) in the z-direction. Due to the length of the system relative to the particle size, only half of the system is showed.

Material parameters As stated before, radius $a = 0.001$ m, normal stiffness $k_n = 10^5$ kg/s^2 and material density $\rho = 2000$ kg/m^3 are chosen. The tangential stiffness is given by two different ratios: $k_t/k_n = 1$ and $k_t/k_n = 1/5$.

Wave agitation In order to agitate a plane wave in z-direction, an initial velocity $\boldsymbol{v}$ is given to all the particles that make up the source, i.e., the second x-y-layer, in contact with the first layer (fixed particles). Note that this initial condition, which is constant in the x-y-plane and is only variable in the z direction, determines the wave unit vector $\hat{\boldsymbol{k}} = (0, 0, 1)$. In order to obtain all different modes observed in the previous section, three different simulations are needed. First a compressive (P) wave is simulated by choosing a velocity $\boldsymbol{v}$ that points in the z-direction, $\boldsymbol{v} = v_z\hat{\boldsymbol{z}}$. In the second simulation the chosen velocity $\boldsymbol{v}$ points in the x-direction, $\boldsymbol{v} = v_x\hat{\boldsymbol{x}}$, creating a x-polarized shear (S) wave. Finally, a last simulation is performed by giving an angular velocity to the first layer, for the z component (rotation around the z axis), $\dot{\boldsymbol{\varphi}} = \dot{\varphi}_z\hat{\boldsymbol{\varphi}}_z$. Note that in order to realize an x-y-invariant perturbation, the same rotation direction is given to all the particles. This creates frustrated rotations. The rotation (R) wave propagates in the z-direction. A velocity $v = 0.01\,\mathrm{m/s}$ is used for the P and S waves, while an angular velocity $\dot{\varphi}_z = 10\,\mathrm{rad/s}$ is used for the R wave.

Results All displacements, velocities and angular velocities in all directions are recorded with a sufficient output frequency at each layer of the packing. The obtained space-time signals are analyzed by performing a double Fourier transform. The transform gives the dispersion relation: $f(k)$, see Sec. 4.1.3 for more details.

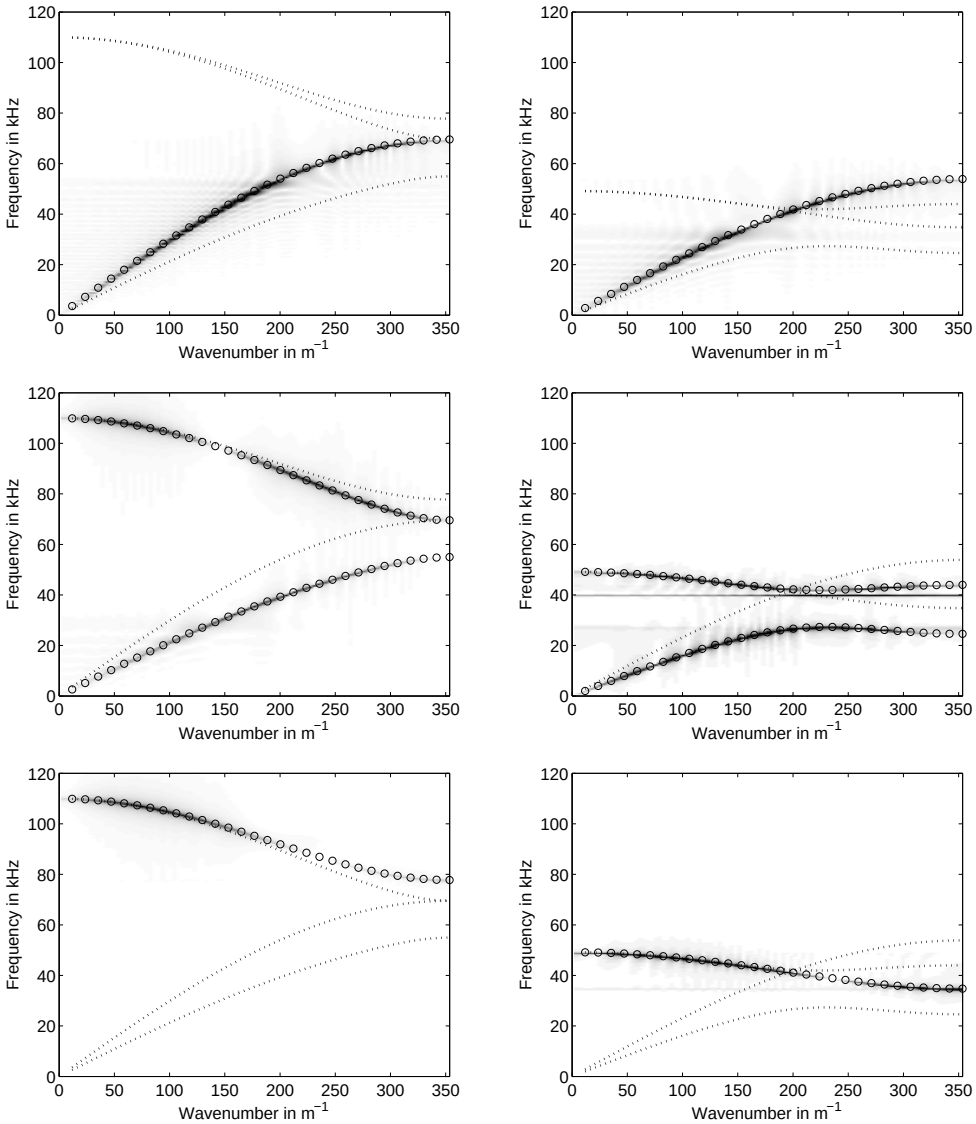

Figure 3.6: Dispersion relation $f(k)$, frequency as function of the wave number for the compressive mode (top), the coupled degenerate shear and rotation modes (middle) and the last rotation mode (bottom). Data from two different k_t: $k_t/k_n = 1$ (left) and $k_t/k_n = 1/5$ (right) are presented. A comparison is made between the theoretical results (open circles) and the simulations results (gray-scaled image), the other modes are indicated by the dotted lines as predicted by theory and discussed above.

The double Fourier transform of the velocity signal in the z-direction (v_z) for the P wave gives a branch which is a sinus over a quarter of a period, see Fig. 3.6 (top). This P-wave dispersion behavior is described in more detail in Sec. 4.1.3. The analysis of the velocity signal in the x-direction (v_x) and the angular velocity

signal around the y-direction $\dot{\varphi}_y$ for the S wave gives by superposition the full two branches of the degenerate shear and rotation modes, see Fig. 3.6 (middle graphs). In the following, this rotation branch will be designated by R_s (s for shear). In order to present the two branches together, the part with negative k of the double Fourier transform where the R_s branch was present has been flipped over to the positive k, see Sec. 4.1.3. The fact that the R_s branch was initially in the negative k part can be interpreted such that the rotation wave associated to this branch is traveling in the opposite direction to the S wave. Our interpretation so far is that the shear wave creates and ejects the rotation wave in its opposite direction.
Finally, by looking at the angular velocity signal around the z direction $\dot{\varphi}_z$ for the R wave, we get another rotation branch that we call R_p, see Fig. 3.6 (bottom). Note that this branch has been flipped as well over from the negative k part. We do not have a clear explanation for that yet.

3.4 Conclusion

In this chapter, the full dispersion relation of an FCC lattice has been calculated from a theoretically derived generalized eigenvalue problem involving translations and rotations. In parallel, wave propagation simulations with a DEM method including a elastic tangential contact law have been performed. The Fourier analysis of time signals for different translational and angular velocities for three different wave modes, P, S and R waves, lead to several dispersion relation branches which are in perfect agreement with the theoretical predictions.
Further investigations are needed in order to interpret in detail the eigen-vectors obtained in the theoretical derivation. Also, the addition of rolling and torsion resistance to the contact interaction will be studied deeper. Note that in ref. [104] it is shown that by adding rolling resistance, the rotation branch R_s can be flipped upwards and hence changes the dispersion behavior for this rotation mode.
Finally, it would be interesting to consider non-Bravais lattices as the Hexagonal Closed Packing (HCP) lattice where optical and rotational modes should co-exist.

4

Effect of contact properties on wave propagation

4.1 Regular systems

This article, with the original title "Sound wave acceleration in granular materials" *by Orion Mouraille, Wim Mulder and Stefan Luding, has been published in the Journal of Statistical Mechanics [79].*

Abstract

The goal of this study is a better understanding of the numerous sound propagation mechanisms in granular materials. In a static, regular (crystal), 3D packing, a small perturbation is created on one side and examined during its propagation through frictionless and frictional packings. The perturbation can be applied in longitudinal and shear direction in order to excite different modes of information propagation, including rotational modes as well. Wave speed and dispersion relation derived from simulation data are compared to those given by a theoretical approach based on a micro-macro transition. The detailed analysis of the wave velocity reveals an interesting acceleration close to the source. Finally a step towards real packings is made by introducing either friction or a tiny (but decisive) polydispersity in the particle size.

4.1.1 Introduction

The mechanisms of wave propagation through a given, possibly random, disordered material are strongly related to the properties of this material. These include the stiffness and the structure, where anisotropy comes into play, but also phenomena like dissipation or friction at the "micro-" or contact-level, see

Refs. [32, 48, 58]. Due to friction, particles rotate and hence the rotational degrees of freedom can also play an important role. Such "micro" phenomena can be modeled with a discrete approach [102, 104], but applications such as oil field exploration and the treatment of seismic data in general, involve larger ("macro") scales and hence do not allow us to view the material in such detail. A continuum description [30] is therefore needed and this leads to the issue of a "micro-macro" transition for information propagation in granular materials.

In the following, section 2 describes the discrete MD (Molecular Dynamics) model used, in particular, the implementation of contacts and friction, and the granular packing structure as well. Section 3 details the influence of dissipation and friction and the difference between modes of agitation and propagation (compressive/shear). The wave speed is analyzed and compared to the continuum theory approach. Also, the dispersion relation is extracted from the data and compared to theoretical predictions. In the last paragraph the influence of small perturbations in the ordered structure of the packing (applying a tiny size distribution to the particles) on the wave propagation is examined.

4.1.2 Description of the model

Discrete Particle Model

The elementary units of granular materials are mesoscopic grains, which deform under the stress developing at their contacts. Since realistic modeling of the internal deformation of the particles is much too complicated, we relate the normal interaction force to the overlap δ of two spherical particles. If the sum of all forces, $\boldsymbol{f}_i$, acting on particle i, either from other particles, from boundaries or from external forces, is known, the problem is reduced to the integration of Newton's equations of motion for the translational and rotational degrees of freedom:

$$m_i \frac{\mathrm{d}^2}{\mathrm{d}t^2}\boldsymbol{r}_i = \boldsymbol{f}_i \ , \quad \text{and} \quad I_i \frac{\mathrm{d}^2}{\mathrm{d}t^2}\boldsymbol{\varphi}_i = \boldsymbol{t}_i \ , \tag{4.1}$$

with the mass m_i of particle i, its position $\boldsymbol{r}_i$, its moment of inertia I_i, its angular velocity $\boldsymbol{\omega}_i = \mathrm{d}\boldsymbol{\varphi}_i/\mathrm{d}t$ and the total torque $\boldsymbol{t}_i$. Note that the above equation is only valid for isotropic bodies, like spheres as used in this study. The force acting on particle i from particle j can be decomposed into a normal and a tangential part.

Linear normal contact law:
If elasticity and dissipation are desired, the simplest force law in normal direction, $\boldsymbol{n} = (\boldsymbol{r}_i - \boldsymbol{r}_j)/|\boldsymbol{r}_i - \boldsymbol{r}_j|$, is a linear spring and a linear dashpot $f_i^n = k\delta + \gamma_0\dot{\delta}$, with

spring constant k and some damping coefficient γ_0. The half-period of a vibration around the equilibrium position leads to a typical response time $t_c = \pi/\omega$, with the eigenfrequency of the contact, $\omega = \sqrt{(k/m_{ij}) - \eta_0^2}$, the reduced mass, $m_{ij} = m_i m_j/(m_i + m_j)$, and the rescaled damping coefficient, $\eta_0 = \gamma_0/(2m_{ij})$. The energy dissipation during a collision, as caused by the dashpot, leads to a restitution coefficient $r = -v_n'/v_n = \exp(-\eta_0 t_c)$, where the prime denotes the normal velocity after a collision.

Tangential Contact Model:
The force in the tangential direction, $\boldsymbol{f}_t$ is implemented in the spirit of Ref. [24], where a tangential spring was introduced to account for static friction. For related literature, see Refs. [16, 63, 66]. In the static case, the tangential force is coupled to the normal force via Coulombs law, i.e., $f^t \leq \mu^s f^n$, whereas for the sliding case one has dynamic friction with $f^t = \mu^d f^n$. The dynamic and the static friction coefficients follow generally the relation $\mu^d \leq \mu^s$. The static case requires an elastic spring, related to the tangential displacement, to allow for a static restoring force, i.e., a non-zero tangential force in static equilibrium due to activated Coulomb friction.

If a contact exists with non-zero normal force, the tangential force is active too, and we project (rotate) the tangential spring, with deformation $\boldsymbol{\xi}$, into the actual tangential plane (this is necessary, since the frame of reference of the contact may have rotated since the last time-step)

$$\boldsymbol{\xi} = |\boldsymbol{\xi}'|\boldsymbol{t}^* \ , \quad \text{with} \quad \boldsymbol{t}^* = \boldsymbol{\xi}^*/|\boldsymbol{\xi}^*| \ , \quad \text{and} \quad \boldsymbol{\xi}^* = \boldsymbol{\xi}' - \boldsymbol{n}(\boldsymbol{n}\cdot\boldsymbol{\xi}') \ , \tag{4.2}$$

where $\boldsymbol{\xi}'$ refers to the tangential spring at the previous iteration, $\boldsymbol{\xi}^*$ is the spring projected into the tangential plane, and $\boldsymbol{n}$ ($\boldsymbol{t}$) are the normal (tangential) unit vectors. This action is relevant only for an already existing spring; if the spring is new, the tangential spring-length is zero anyway, however, its evolution is well defined as shown below. The tangential velocity,

$$\boldsymbol{v}_t = \boldsymbol{v}_{ij} - \boldsymbol{n}(\boldsymbol{n}\cdot\boldsymbol{v}_{ij}) \ , \tag{4.3}$$

is computed from the total relative velocity of the surfaces of the two contacting particles,

$$\boldsymbol{v}_{ij} = \boldsymbol{v}_i - \boldsymbol{v}_j + a_i\boldsymbol{n}\times\boldsymbol{\omega}_i + a_j\boldsymbol{n}\times\boldsymbol{\omega}_j \ . \tag{4.4}$$

Next, we calculate the tangential test-force as the sum of the tangential elastic and viscous forces (in analogy to the normal force model),

$$\boldsymbol{f}_{\mathrm{o}}^t = -k_t\,\boldsymbol{\xi} - \gamma_t\boldsymbol{v}_t \ , \tag{4.5}$$

with the tangential spring stiffness k_t and a tangential dissipation parameter γ_t. As long as $|\boldsymbol{f}_{\mathrm{o}}^t| \leq f_C^s$, with $f_C^s = \mu^s f^n$, one has the *static friction* case (1) and, on the other hand, if $|\boldsymbol{f}_{\mathrm{o}}^t|$ becomes larger than f_C^s, the sliding, *dynamic friction* case (2) is active with the (possibly lower) Coulomb limit $f_C^d = \mu^d f^n$. Sliding case (2) is active as long as, in the next steps, the test force remains $|\boldsymbol{f}_{\mathrm{o}}^t| > f_C^d$. If the tangential force drops below the dynamic Coulomb limit, $|\boldsymbol{f}_{\mathrm{o}}^t| \leq f_C^d$, static friction becomes active again, with the (possibly larger) Coulomb limit f_C^s, giving rise to stick-slip behavior. Typically, a contact starts with finite tangential velocity and $\boldsymbol{\xi} = 0$; during the first time-steps, the spring is stretched and the velocity decreases.

In the *static* case (1), the tangential spring is incremented

$$\boldsymbol{\xi}' = \boldsymbol{\xi} + \boldsymbol{v}_t \, \delta t_{\mathrm{MD}} \ , \tag{4.6}$$

with the time step δt_{MD} of the DEM simulation. The new value of $\boldsymbol{\xi}'$ is to be used in the next iteration in Eq. (4.2), along with the tangential force $\boldsymbol{f}^t = \boldsymbol{f}_{\mathrm{o}}^t$ as defined in Eq. (4.5).

In the *sliding* case (2), the tangential spring is adjusted to a length, which is consistent with the Coulomb condition,

$$\boldsymbol{\xi}' = -\frac{1}{k_t} \left(f_C^d \, \boldsymbol{t} + \gamma_t \boldsymbol{v}_t \right) \ , \tag{4.7}$$

with the tangential unit vector, $\boldsymbol{t} = \boldsymbol{f}_{\mathrm{o}}^t / |\boldsymbol{f}_{\mathrm{o}}^t|$, defined by the direction of the force in Eq. (4.5). Note that this guarantees that the force magnitude does not exceed the Coulomb limit: Inserting $\boldsymbol{\xi}'$ into Eq. (4.5) leads to $\boldsymbol{f}_{\mathrm{o}}^t \approx f_C^d \boldsymbol{t}$, where $\boldsymbol{f}_{\mathrm{o}}^t$ and $\boldsymbol{v}_t$ are not necessarily parallel to each other in 3D. In short notation the tangential force on particle i reads

$$\boldsymbol{f}_i^t = \min \left(f_C, |\boldsymbol{f}_{\mathrm{o}}^t| \right) \boldsymbol{t} \ , \tag{4.8}$$

where f_C follows the selection rules described above.

Model system

The configuration considered here is a dense, static packing of grains contained in a cuboid. In the following, mono-disperse, structured (crystal) packings are studied, and a few results obtained by introducing a small polydispersity in the particle size of 0.2%, is presented. A more detailed study where both (large) polydispersity and disorder are considered, will be presented elsewhere [78]. The mono-disperse structured packing used here is a Face Centered Cubic (FCC) packing: square-layers in the x-y-plane are stacked on top of each other (in z-direction), such that each layer fits into the holes of the one below, and each

second layer is just a z-shifted copy of the original. The distance between square layers is $l_0 = d/\sqrt{2}$ for a particle diameter d. In Fig. 4.1 a part of a packing with 3200 particles is displayed, with 4 times 4 particles in the x, y-planes ($l_x = l_y = 4d$) and 200 layers in z-direction ($l_z = 200l_0$ – only about 90 layers are shown). Based on a particle-centered square in the first layer, a unit-cell (cuboid) therefore has a volume $V_u = \sqrt{2}d^3$ and contains 2 particles with volume $2V_p = (\pi/3)d^3$ such that the volume fraction is $\nu = 2V_p/V_u = \pi/(3\sqrt{2}) \approx 0.74$. Each particle has four contacts inside each square-layer, and eight with particles in both neighboring layers, corresponding to a coordination number $\mathcal{C} = 12$. This structure will not change in the simulations described below (except for the results with polydispersity), i.e., the case of small amplitude perturbations is considered. Note that the packing is invariant by translation in the x- and y-directions, but different in the z-direction, hence it is an anisotropic system (see Fig. 4.1).
Polydisperse packings are obtained by using the regular structure where a tiny size distribution is given to the particles. The volume is kept constant, and since the deformations are tiny the polydisperse packings are still ordered.

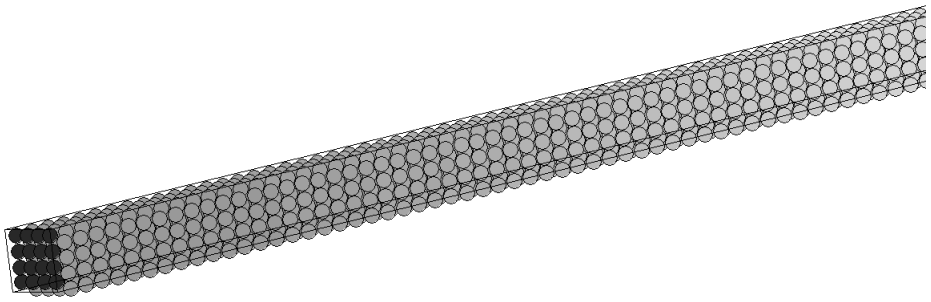

Figure 4.1: Snapshot of a part of the typical system used (long FCC packing). The dark particles belong to the fixed layer.

The packing is treated as piece of a larger sample via periodic boundaries, i.e., if a particle exits the simulation volume at one side, it enters at the opposite side at a corresponding position with the same velocity; particles feel each other across the periodic boundaries. While creating the regular structure, the position of particles is chosen such that the overlap is the same at all contacts in the system, hence giving an anisotropic stress, $\sigma^0_{xx} = \sigma^0_{yy} \neq \sigma^0_{zz}$ due to the anisotropic structure. The contact overlaps are chosen much smaller than the particle diameter, $\delta/d \approx 10^{-3}$. Before a small amplitude sound wave is excited (2), the system must be relaxed (1) first to a reasonable static equilibrium state.

(1) One possible criterion for a relaxed static state is the ratio of kinetic to potential energy. When this ratio becomes smaller than a given limit (10^{-7} in this study), the packing is said to be in a static state. For the regular, homogeneous

packings used in the following, the system can be prepared immediately in a static configuration, whereas for the polydisperse packing (last paragraph) the system has to be relaxed. Note that such a relaxation typically takes much longer than a typical wave propagation simulation.

(2) Waves are excited by applying a small perturbation at one side of the system, i.e., by shifting a layer of particles. The wave vector, $\boldsymbol{k}$, and thus the wave propagation direction are perpendicular to the excited layer. Compressive (P) and shear (S) modes can be triggered by directing the perturbation parallel or perpendicular to the wave propagation direction, respectively. The typical packing used is long in the z-direction ($200l_0$ with l_0 the distance between two layers), which allows to study the wave for a long time and large distances. We checked that the results do not depend on the extension in x- and y-direction by comparing simulations with different size l_x, l_y. Therefore $l_x = l_y = 4d$ was used in order to reduce the number of particles. Such a long but thin system contains only $N = 3200$ particles with radius $a = d/2 = 0.001$ m. The mass of a spherical particle is $m = \rho_0(4/3)\pi a^3$, with the material density $\rho_0 = 2.\,10^3$ kg m^{-3}. The total mass of the system is thus $M \approx 0.027\,\mathrm{kg}$. The stiffness material parameters in normal and tangential direction are $k = 10^5\,\mathrm{N\,m^{-1}}$ and k_t, given in units of k, e.g., $k_t = 0.2k$. Dissipation $\gamma_t = \gamma_0 = 0$ is used if not explicitly specified. This leads to a typical (two-particle) contact duration $t_c = 2.033\ 10^{-5}\,\mathrm{s}$ and collision frequency $\omega_c = 150\,\mathrm{kHz}$, (the equations used to calculate these values are given in section 2.1). Note that the oscillation frequency of a particle in a crystal, with more than one contact, is higher than the collision frequency based on only one contact. For reliable numerical results, the criterion for the integration time-step is $\delta t_{\mathrm{MD}} < \frac{t_c}{50} \approx 4.10^{-7}$ s.

4.1.3 Simulation results

In this section, a typical wave propagation simulation is presented. Then the effects of dissipation and friction are discussed. Also the wave propagation speed and the dispersion relations are determined and, finally, some irregularity is introduced in the crystal lattice.

A typical wave propagation simulation

As result of the strain-controlled perturbation of a layer, as described above in section 2.2, a plane compressive stress pulse (P wave) is created and propagates in the system in z direction, see Fig. 4.2. More specific, a x, y-layer is shifted by $\Delta z/d = 10^{-4}$. This displacement amplitude, Δz, that excites the wave is still small as compared to the typical overlap $\Delta z/\delta = 10^{-1}$. The traveling plane wave

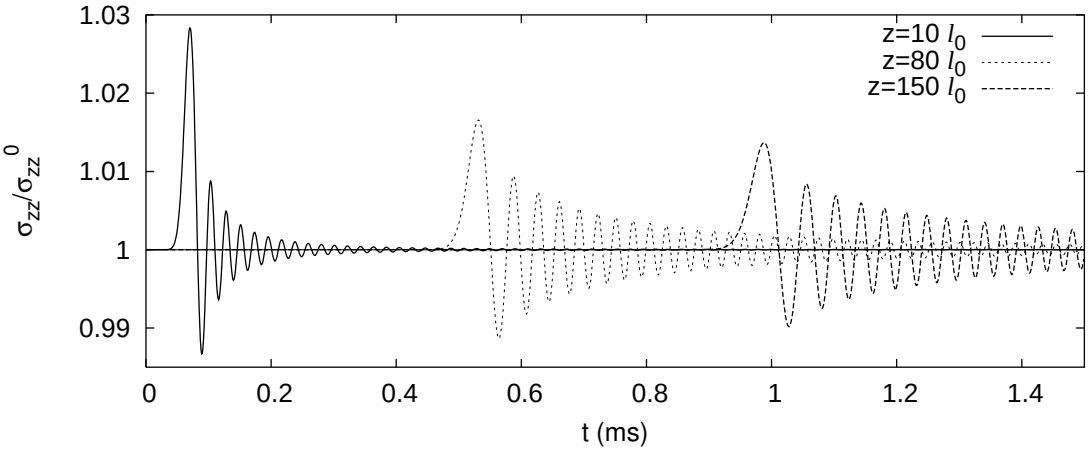

Figure 4.2: Normal stress (σ_{zz}) scaled by the equilibrium stress (σ^0_{zz}) as function of time at different positions $z/l_0 = 10$, 80, and 150, with the distance from the source, z, and the layer distance l_0.

can be observed in various quantities like stress, displacement, kinetic energy, etc. Since the system is made of layers, it is possible to "record" the pulse at each layer as a function of time. Fig. 4.2 shows the scaled normal stress versus time at different positions along the wave propagation direction. The advantage of periodic boundaries is that all particles are embedded in the same environment. As consequence, two opposite ends of the system are connected, and a tensile wave would travel in the direction opposite to the compressive pulse. The two waves will interfere after having traveled through half of the system. In order to avoid this, and to maximize the distance that can be traveled by a pulse, two layers of particles at the opposite ends of the system (z-direction) are fixed – the other two directions remain periodic. This avoids the tensile pulse, but not boundary reflections that lead to an oscillating "coda" traveling after the primary pulse, see Fig. 4.2. The alternative way of driving by specifying an initial velocity as perturbation of the layer (without controlling its displacement further on) excites a wave of the same nature and with the same properties, but a weaker primary pulse relative to the coda is observed.

With increasing distance from the exciting "source" layer the particles experience an increase in stress with a time delay and also with smaller amplitude and a slower rate of change, see Fig. 4.2. When the wave arrives at the other side, it is reflected from this "receiver" layer and travels back and forth between source and receiver several times, ever decreasing in amplitude (data not shown here). Modulations of the stress, much smaller than the agitation peak-stress, persist throughout the whole simulation. The analysis presented in the following

considers only the initial, undisturbed wave, since interference with the reflected wave would disturb the signal. The shape of the signals and the wave speed will be examined next.

Signal shape and damping

The pulse in Fig. 4.2 consists of two parts. The first strong peak corresponds to the increase of stress when the wave front arrives at the recording position. The second part, the "coda" of the signal, consists of secondary wave fronts created by the oscillation of the layer closest to the shifted layer (that stays fixed after the shift). During propagation, the first peak's amplitude decreases and its width increases. Note that there is no active dissipation, so that the described signal behavior is caused by the frequency-dependent nature of the wave (dispersion), and the particular boundary condition.

When two real particles interact or collide with each other, a part of the kinetic energy is transformed into thermal energy, due to the local plastic deformation at the contact. It is not clear whether this phenomenon can be described properly by a linear spring-dashpot model. However, it appeared relevant for the sake of completeness, to study the influence of the dissipation model parameter on our results. More advanced contact models will be studied elsewhere [78].

As result of dissipation in the contact law (setting $\gamma_0 > 0$ and $r < 1$, where γ_0 and r were defined in section 2.1), both the amplitude of the first wave front and of the coda decrease, see Fig. 4.3 (Left). Note that the first pulse is affected much less than the coda, i.e., for a strong enough dissipation $\gamma_0 > 0.1\,\mathrm{kg\,s^{-1}}$, the coda has almost disappeared after ten layers, while the first peak continues traveling.

Fig. 4.3 (Right) shows the dependence of the peak amplitude evolution on dissipation. The strongest decay rate is observed when the dissipation time-scale $t_\gamma = m_{ij}/\gamma_0$ and a typical contact duration time-scale (oscillation period) become comparable: $t_\gamma \approx 2t_c$. In summary, the wave is not affected by very weak dissipation. Stronger dissipation, however, lets the coda vanish but hardly changes the wave speed of the first peak, as discussed in the following paragraph.

The wave speed in frictionless packings

One way to define the wave speed is to measure the time it takes the peak of the first pulse to travel a certain distance. Plotting the z-position of the peak against the time t when it reaches that position (not shown here) gives an almost straight line. The slope of this line then gives the speed V_p during propagation, see Fig. 4.4. Just assuming a constant speed (a linear fit to the z,t-data) leads to $V_{p1} \approx 216\,\mathrm{m/s}$. This disregards the interesting acceleration

of the pulse early during propagation. In Fig. 4.4, the wave speed is compared to the simply fitted V_{p1} and to the theoretical prediction V_{pz} as obtained from a micro-macro transition next. Note that in the article by Somfai et al [102], such an acceleration is also observed.

In order to compare the measured propagation speed with existing theories, it is assumed that the granular material behaves like an *elastic continuum* [30,122]. The anisotropic relation between stress- and strain-increments involves a material tensor $\boldsymbol{C}$ of rank four. In symbolic and index notation (Einstein convention with summation over double indices) this reads in incremental form:

$$\dot{\boldsymbol{\sigma}} = \boldsymbol{C} : \dot{\boldsymbol{e}} \ , \quad \text{or} \quad \dot{\sigma}_{ij} = C_{ijkl}\dot{e}_{kl} \ , \tag{4.9}$$

with the stress- and strain-rates on the left and right, respectively. This describes the response of our packing to large wavelength perturbations and implies the assumption of a *constant, time-invariant* material tensor, which can hold only for *small* deformations, and does not allow for opening or closing of contacts or even large scale rearrangements. In our regular system, neither of these conditions is violated. The stiffness tensor of the material can be derived from the potential energy density via virtual displacement, see Refs. [64, 66],

$$C_{\alpha\beta\gamma\phi} = \frac{1}{V}\sum_{p\in V}\left(k\sum_{c=1}^{C}(l^2/2)n_\alpha^c n_\beta^c n_\gamma^c n_\phi^c + k_t\sum_{c=1}^{C}(l^2/2)n_\alpha^c t_\beta^c n_\gamma^c t_\phi^c \right) \ , \tag{4.10}$$

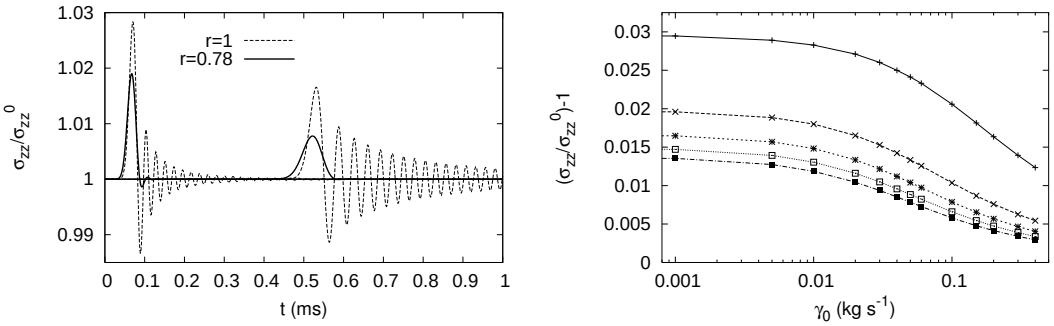

Figure 4.3: (Left) Two wave signals are plotted at $z/l_0 = 10$ and 80, as in Fig. 4.2, without damping (dashed line) and with damping (solid line). The dissipation strength is $\gamma_0 = 0.1\,\mathrm{kg\,s^{-1}}$, which corresponds to a restitution coefficient $r = 0.78$ and a contact duration $t_c = 2.039\ 10^{-5}$ s, comparable to the viscous damping time scale $t_\gamma = m_{ij}/\gamma_0 = 4.19\ 10^{-5}$ s.
(Right) The first peak amplitude at different positions ($z/l_0 = 10$, 45, 80, 115, and 150 from top to bottom) is plotted against the dissipation strength, displaying the decay of the wave amplitude with increasing dissipation and traveling time. The strongest decay rate is the point with the largest (negative) slope.

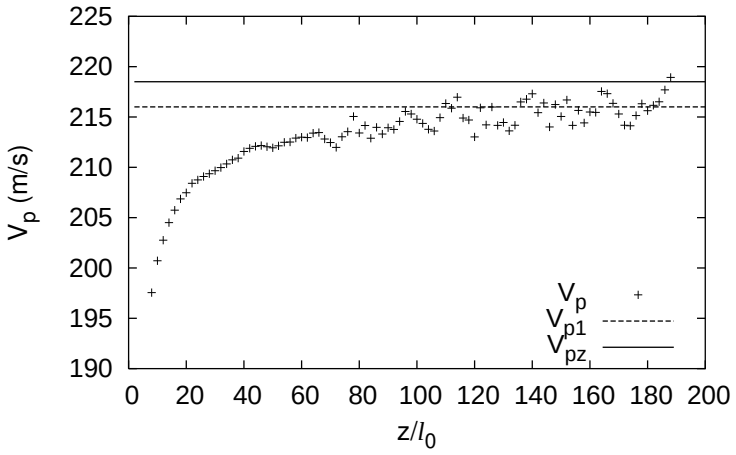

Figure 4.4: From the simulation without dissipation, see Fig. 4.3, the speed of the first peak maximum, V_p, is plotted as a function of the distance from the source. (A center-weighted average over five layers is used here. Also a higher output frequency was needed to obtain reliable data.) The dashed line indicates the average speed, V_{p1}, and the solid line is the theoretical prediction, V_{pz}.

with the branch vector $l \approx d$ and a representative volume V, e.g., the volume of the unit cell V_u. For a frictionless packing the second term involving k_t is of course disregarded. From continuum theory, the P wave speed in z-direction is expected to be ${V_{pz}}^2 = C_{zzzz}/\rho$ and, e.g., the S wave speed in the same direction is ${V_{sz}}^2 = C_{zxzx}/\rho$. In Ref. [77] the prediction for the ratio $(V_{pz}/V_{sz})^2 \approx C_{zzzz}/C_{zxzx} = 2$ was confirmed.

Inserting the contact normal and tangential vectors into Eq. (4.10), one can compute, e.g., C_{zzzz}, which leads to $V_{pz} = 218.5\,\mathrm{m/s}$ close to the linear fit estimate $V_{p1} \approx 216\,\mathrm{m/s}$ (see above section 3.3). This holds also for the plane S-wave propagating in the same direction (either polarized in the x or y direction), for which the theory gives $V_{sz} = 154.5\,\mathrm{m/s}$ and the linear fit $V_{s1} \approx 153\,\mathrm{m/s}$.

We performed a set of simulations exploring the anisotropy in the frictionless packing with P- and S-waves in other directions for the propagation and for the particle movements and obtained similar agreement concerning the wave speeds. The anisotropy is summarized by the ratios of coefficients of the material tensor, $C_{xxxx}/C_{zzzz} = 1.25$, $C_{zxzx}/C_{yxyx} = 2$ and $C_{zzzz}/C_{zxzx} = 2$.

Dispersion relation for frictionless packings

The frequency dependence of the waves in our system can be studied by performing a Fourier analysis in time and space. From a (t, x) data set in a system of length $l_z = 200\,l_0$, with spacing $\Delta z = l_0 = d/\sqrt{2}$, every layer position is taken into

account, i.e., 200 points in x-space are available. The time-window $0 \leq t \leq t_{max}$ (with time step $\Delta t = 10^{-6}\,\mathrm{s}$ and $t_{max} = 1199\Delta t$, i.e., 1200 data points), is chosen such that the wave has not yet arrived at the end of the system, so that reflections are not included in the signal. The dispersion relations are obtained for P and

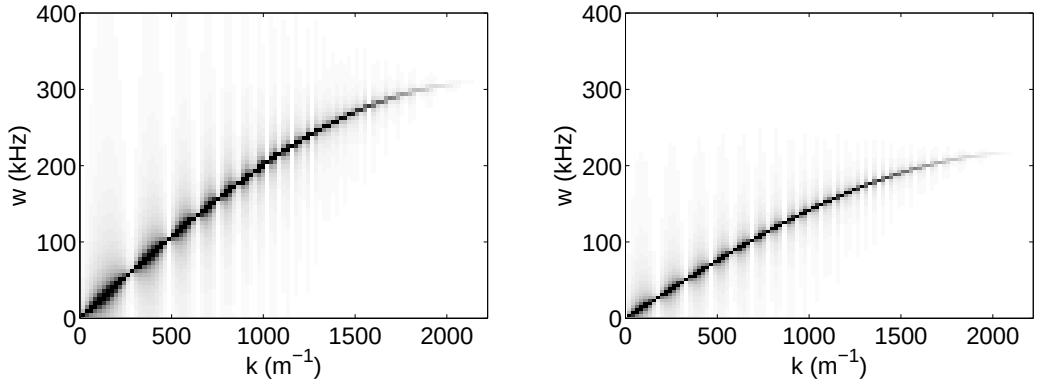

Figure 4.5: Dispersion relations (grey-scale corresponds to the amplitude, absolute value, of the Fourier coefficients) for P wave (Left) and S wave (Right) propagating in z direction in the anisotropic packing.

S waves propagating in z direction, see Fig. 4.5. The MATLAB function `fft2` has been used, which returns the Fourier coefficients in an indexed (ω, k)-field $F(\omega, k)$ of the same size as the input (t, x) data. Transformation to frequency and wave-number is performed by multiplying the index with $\Delta\omega = 2\pi/t_{max}$ and $\Delta k = 2\pi/l_z$. Special care has to be taken that the indices corresponding to $\omega = 0$ and $k = 0$ are properly shifted to zero.

In order to obtain a sine fit $\omega(k) = \omega_0 \sin(\frac{kl_0}{2})$ to the Fourier data, the locations of the maximal Fourier coefficients on the frequency axis are determined by a power-law weighted average, $\omega_{max}(k) = \Sigma F(\omega, k)^\phi\, \omega / \Sigma F(\omega, k)^\phi$, with $\phi = 4$. The quality of the fit is impressive with respect to both shape of the curve and magnitude of ω_0. The sine function is consistent with the theoretical work by Suiker et al. [104], where the dispersion relation for 2D lattices is discussed. According to the fits, the maximal frequencies are $\omega_0^{pz} = 309132\,\mathrm{s}^{-1}$, $\omega_0^{sz} = 218437\,\mathrm{s}^{-1}$, and the minimal wavelength is $2l_0$. The largest wave speed is obtained for $V_{pz}^{\omega}(k = 0) = \frac{d\omega}{dk}|_{(k=0)} = \omega_0 l_0/2 = 218.59\,\mathrm{m/s}$, and $V_{sz}^{\omega}(k = 0) = 154.45\,\mathrm{m/s}$. These values have to be compared to the prediction based on the micro-macro transition: $V_{pz} = 218.50\,\mathrm{m/s}$ and $V_{sz} = 154.50\,\mathrm{m/s}$, respectively, in order to appreciate the perfect agreement between an effective continuum theory and the discrete simulation.

The acceleration of the wave observed above can now be quantitatively related to an increasing wave-length during propagation. As crude approximation, the duration T of the first oscillation of a signal (based on first-arrival time – one per-cent peak level), see Fig. 4.2, at a given position (z), multiplied by the corresponding speed V, see Fig. 4.4, gives an estimated wavelength $\lambda = VT$, for this part of the signal at the given position. We obtain $\lambda/l_0 \approx 8$, 9, 10, 16, and 19, with error-margin ± 1, at $z/l_0 = 10$, 15, 20, 80, and 150, respectively.

Using the dispersion relation, a typical wave-number can be related to a local wave propagation speed. In subsection 3.3, the wave is excited with a minimal wave-length and rapidly adapts to a speed of $V^{\omega}_{pz}(z/l_0) \approx 208\,\mathrm{m/s}$ at $z/l_0 \approx 20$, and accelerates further on, see Fig. 4.4. The dispersion relation leads to a prediction of the wave-number as function of the local wave-speed at position z/l_0,

$$k\left(\frac{z}{l_0}\right) = \frac{2}{l_0} \arccos \frac{V^{\omega}_{pz}(z/l_0)}{V^{\omega}_{pz}(k=0)} \ ,$$

an expression that works well for short and intermediate distances. At different positions one finds the wavelengths $\lambda = 2\pi/k$ with $\lambda_{10} \approx 8.3\,l_0$, $\lambda_{15} \approx 9.2\,l_0$, $\lambda_{20} \approx 10.1\,l_0$, $\lambda_{80} \approx 13.9\,l_0$, $\lambda_{150} \approx 17.0\,l_0$, consistent with the crude average obtained from the oscillation duration of the signal for the shorter distances. At longer distances from the source, the strong fluctuations and the fact that the slope of the dispersion relation only weakly changes for small k, leave the prediction with too large error margin to be useful.

The typical wavelength is increasing while the wave (slightly) accelerates. The dispersion relation acts such that low-frequency/long wavelength components are faster than the high-frequency wave components with smaller wavelength. With other words, narrow pulses can not travel fast, and high frequency perturbations ($\omega \approx \omega_0$) will practically not propagate at all, so that the larger wave-lengths remain traveling after long distances.

This detailed quantitative study of the classical dispersion relation in a crystal (see literature in solid state physics) is only the reference basis for more detailed research on sound propagation in polydisperse, disordered, frictional and anisotropic granular media.

The influence of friction

Friction is now introduced in the same system as described previously. The new parameters are μ, the friction coefficient, which is kept constant to $\mu = 0.5$ and k_t the tangential stiffness for which we performed a parameter study with the following values: $k_t/k = 0, 0.2, 0.5, 1, 1.5$ and 2. Since there are no sliding

contacts, due to the small amplitude perturbation, neither are differences of static and dynamic friction coefficients, or different magnitudes of μ, relevant here (data not shown). Of course by choosing an artificially low value for μ ($\mu = 0.001$), see [77], sliding contacts occur and influence the results. This was checked by performing several simulations with $\mu_d \neq \mu_s$ and different magnitudes. Since details of the friction model are not relevant here, we use $\mu_d = \mu_s = \mu = 0.5$ in the following.

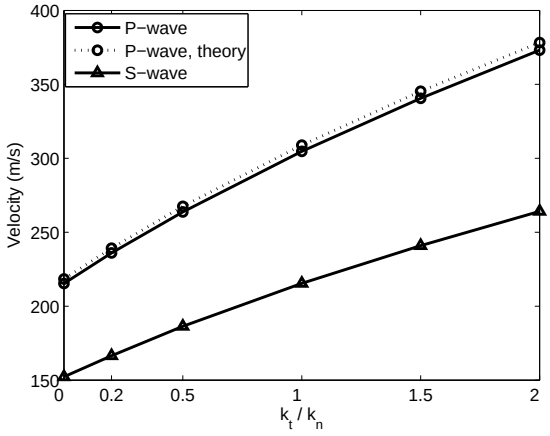

Figure 4.6: Wave velocities as function of the ratio k_t/k_n, with the normal stiffness, $k_n = k$, as introduced in section 2 (simulation and theory as described in the text).

The system is prepared *without* friction such that $f_t = 0$ (f_t is the contact force in the tangential direction) at $t = 0$ and $f_t \neq 0$ as soon as displacements and deformations occur. Note that a different preparation procedure (data not shown) will lead to a different initial condition, with contacts close to the sliding limit, and thus to different observations and conclusions.

The same analysis is performed as before (without friction) for both P- and S-waves. In both cases (P- and S-wave) the first peak amplitude decreases as the tangential stiffness (k_t) is increasing. Also the "coda" tends to decay stronger and vanishes. The velocity increases with k_t increasing and it is pretty well predicted for the P-wave by using Eq.(10) for the stiffness tensor and using the simulation data in order to get the direction of both contact normals and tangential springs, see Fig. 4.6 (theory). However for the S-wave it is not possible to use the same formula for the stiffness tensor, since the influence of rotations is strong and irregular in the tangential direction of contacts and renders Eq. (10) inappropriate. A more complete model like introduced in [104, 105] is needed in order to take rotations into account.

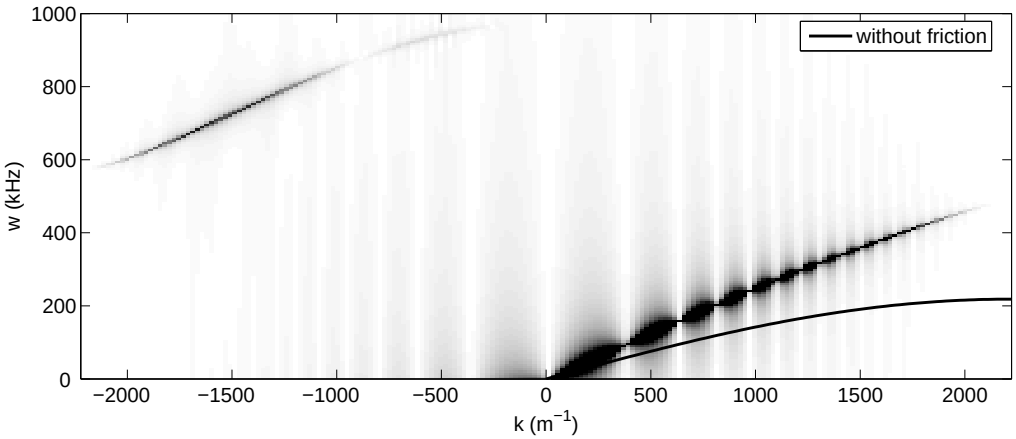

Figure 4.7: Dispersion relation (grey-scale corresponds to the amplitude of the Fourier coefficients) for the S-wave with $k_t/k_n = 2$. The solid line gives the best fit to the P-wave dispersion relation from the system without friction, as discussed earlier.

The same agreement as in section 3.4, between theory and simulations, is obtained for the dispersion relation for the P-wave with friction. For the S-wave, a new branch appears in the $\omega(k)$ picture for negative wave numbers, see Fig. 4.7, and the original branch deviates from the sine shape towards higher frequencies and higher wave velocities. Larger wave numbers (smaller wavelength) modes can propagate with higher speed (slope of the dispersion relation), dependent on the magnitude of k_t. The frequency range of the new branch is tuneable, i.e., smaller k_t leads to smaller frequencies. The positive trend of this branch indicates that it is related to a wave traveling in the same direction as the S-wave. However, we still have no clear interpretation for this branch. Presumably it is a trace of the rotational degree of freedom of the particles. A more quantitative study of wave propagation in frictional, rotating systems will be presented elsewhere [78].

Frictionless, slightly polydisperse and ordered systems

Some polydispersity is now introduced in the crystal structure, by applying a size distribution to the particles. The distribution is homogeneous, centered at the original monodisperse value of the radius ($a = 0.001\,\mathrm{m}$) and has a width ($2\Delta a$) of the order of the overlap ($\delta/a = 10^{-3}$).

More precisely we studied three different cases with $\Delta a = \frac{\delta}{2}, \delta$ and 2δ. The simulations are performed with the same parameters as in the ordered, elastic case (section 3.1). The difference is that a preparation-simulation is needed in

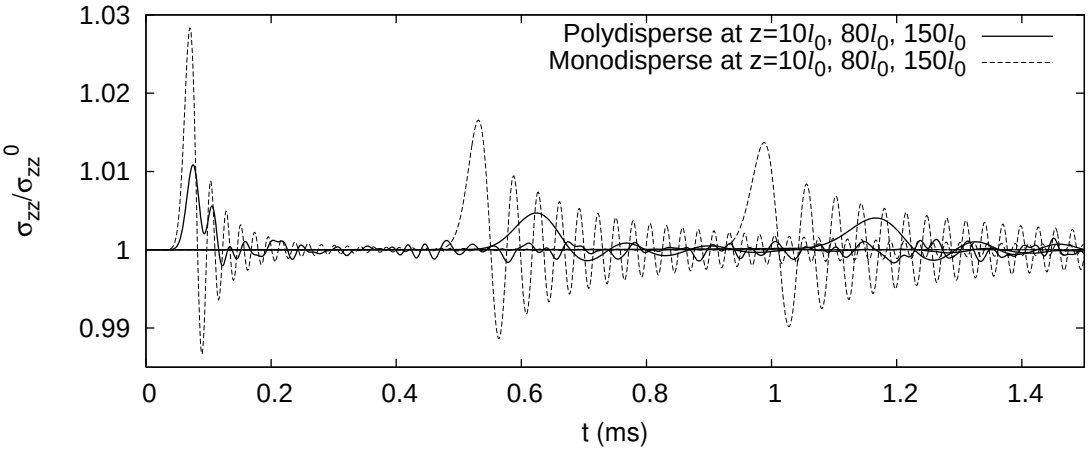

Figure 4.8: Normal stress (σ_{zz}) scaled by the equilibrium stress (σ_{zz}^0) as function of time at different positions $z/l_0 = 10$, 80, and 150, with the distance from the source, z, and the layer distance l_0. Comparison between the monodisperse system (see Fig. 4.2) and the polydisperse system with $\Delta a = 2\delta$.

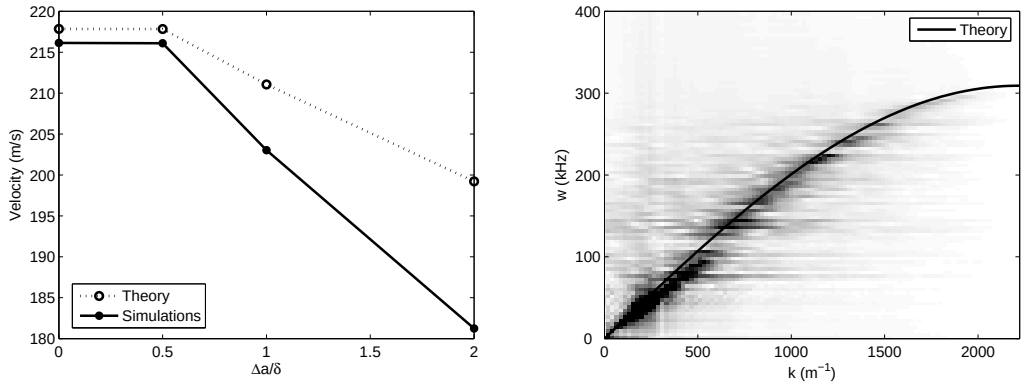

Figure 4.9: (Left) P-wave velocities as function of polydispersity (simulations and theory). (Right) Dispersion relation (grey-scale corresponds to the amplitude of the Fourier coefficients) for the P-wave in the polydisperse system, $\Delta r = 2\delta$. The solid line corresponds to the dispersion relation from the monodisperse, ordered system.

order to relax the system, as mentioned in section 2.2. As one can see from Fig. 4.8, the signal is strongly affected for $\Delta a = 2\delta$. For $\Delta a = \delta/2$, the signal is practically unchanged, and for $\Delta a = \delta$ we obtained something in between the two other cases (data not shown). In the case of $\Delta a = 2\delta$, the size variation is 0.2% of the radius but 200% if related to the overlap (δ).

The fact that polydispersity has to be related to the overlap rather than the particle size was already reported in [62]. As consequence, strong non-linear

effects at the contacts, such as opening and closing, are evidenced. Note that the coordination number of the relaxed, disordered packing ($\Delta a = 2\delta$) is $C \simeq 9.975$. This represents a loss of 17% of the contacts as compared to the ordered system ($C = 12$). During the wave propagation the coordination number is oscillating (as result of opening and closing of contacts), by less than 0.01%. In this non-linear context, the linear theory used to predict the wave velocity fails (discrepancies up to 9% for $\Delta a = 2\delta$). For a theoretical approach on the moduli, that considers random arrays, see Ref. [47]. Also the dispersion relation is much broader, more noisy, and random gaps seem to appear, although the sine shape is still visible (see Fig. 4.9).

4.1.4 Conclusions

Wave propagation was examined in three dimensional regular (crystal) monodisperse packings of spheres, for compressive (P) and shear (S) propagation modes. Different dissipation strength and friction coefficients were used and an interesting acceleration of the wave during propagation was observed for both P- and S-waves in frictionless systems.

For the wave speeds, quantitative agreement was obtained between simulations and theoretical predictions based on a micro-macro computation of the stiffness material tensor for the anisotropic lattice. Also the dispersion relation agrees perfectly well with theory and the observed acceleration of the traveling wave can be related to the dispersion and widening of the pulse: the initially narrow pulse travels slower than the wider, more developed pulse. Close to the source, the major wave number (wave length) can be well predicted as function of the wave speed.

The study of frictional packings indicates the importance of rotations, and also the limitations of the proposed theory for the wave speed. In the dispersion relation, the S-wave branch becomes steeper and more straight (the sine-shape is lost), and a second branch at higher frequencies occurs.

Finally in the last paragraph, weak polydispersity was introduced and more generally, non-linearity effects are evidenced already for rather small disorder. The dispersion relation becomes more noisy but the shape is maintained.

All this shows that by capturing already a certain amount of relevant and interesting features of wave propagation in granular materials, the model proposed seems to be an appropriate starting point in order to investigate quantitatively and more deeply the phenomenon of wave propagation in polydisperse, inhomogeneous, anisotropic, dense, frictional granular materials.

Acknowledgments

Helpful discussions with G. Herman and A. Suiker are appreciated. This work is part of the research programme of the Stichting voor Fundamenteel Onderzoek der Materie (FOM), financially supported by the Nederlandse Organisatie voor Wetenschappelijk Onderzoek (NWO) and the Stichting Shell Research.

4.2 Cohesive, frictional systems and preparation history

This article, with the original title "Sound propagation in isotropically and uniaxially compressed cohesive, frictional granular solids" *by Orion Mouraille, Olaf Herbst and Stefan Luding, will be published (in press) in Engineering Fracture Mechanics [82].*

Abstract

Using an advanced contact model in DEM simulations, involving elasto-plasticity, adhesion, and friction, pressure-sintered tablets are formed and prepared for unconfined tests. Sound propagation in such packings is studied under various friction and adhesion conditions. Small differences can be explained by differences in the structure that are due to the sensitivity of the packing on the contact properties during preparation history. In some cases the signals show unexpected propagation behavior, but the power-spectra are similar for all values of adhesion and friction tested. Furthermore, one of these tablets is uniaxially and unconfined compressed and the sound propagation characteristics are examined at different strains, (i) in the elastic regime, (ii) during failure, and (iii) during critical flow. Similarly, the results do vary astonishingly little for packings at different externally applied strains.

4.2.1 Introduction

Granular Materials in general [11, 12, 34, 38–40, 43–45, 60, 94, 99] and especially cohesive, frictional, fine powders show a peculiar flow behavior [18,64,67,89,114]. Adhesionless powder flows freely, but when adhesion due to van der Waals forces is strong enough, agglomerates or clumps form, and can break into pieces again [51,108,109,111]. This is enhanced by pressure- or temperature-sintering [65] and, under extremely strong pressure, tablets or granulates can be formed [69–72] from primary particles. Applications can be found, e.g. in the pharmaceutical industry.

The basic question is how to understand such cohesive, frictional, fine powders and whether one can use sound propagation measurements from simulations to gain additional insight.

In contrast to crystalline materials [77, 79], information propagation in disordered and inhomogeneous granular media is far from well understood, especially when friction and other realistic contact mechanisms are taken into account [66,80,81]. Understanding better the sound propagation in granular media

will improve the interpretation of ultrasound measurements in soil as a non-intrusive way to detect and measure underground structures. This has applications in archeology, seismology and – because of its cost efficiency – for the discovery and exploitation of natural resources such as ores, coal, or oil

Stress-wave or sound propagation through dense granular matter is the superposition of many complex phenomena, which are caused by the discrete, inhomogeneous, anisotropic and dissipative structure of this class of materials. The properties of such waves are strongly affected by phenomena like attenuation, scattering, and dispersion [49]. Ballistic pulse propagation co-exists with slower, multiply scattered coda-like signals [48,49]. The stress- and frequency-dependence of the wave propagation features are subject of ongoing discussion [42,49] in static and shaken packings as well.

Many-particle simulations methods like discrete element models (DEM) [9,24, 40,92,110,112,122] complement experiments on the scale of small "representative volume elements" (RVEs) [122]. Deep and detailed insight into the kinematics and dynamics of the samples can be obtained since the information about all particles and contacts is available at all times. Discrete Element Models require the contact forces and torques as the basic input, to solve the equations of motion for all particles in a granular system. From this, the macroscopic material properties as, among others, elastic moduli, cohesion, friction, yield strength, dilatancy, or anisotropy can be measured from such RVE tests.

The macroscopic properties are controlled by the "microscopic" contact forces and torques [19,42,49,58,101]. Non-linear contacts [92,106], frequency-dependence [85,118] and also scattering and attenuation in other "particle type" materials [27] have been reported.

Research challenges involve not only realistic DEM simulations of many-particle systems and their experimental validation, but also the transition from the microscopic contact properties to the macroscopic flow behavior [1, 64, 67, 122, 123]. This so-called micro-macro transition [64, 67] should allow to better understand the collective flow behavior of many particle systems as a function of the particles' material and contact properties. A continuum description ("macroscopic") of (dense) granular materials can be highly useful for field applications (like oil discovery), since particle simulations ("microscopic") are not applicable due to the huge system sizes. Some empirical descriptions are available also for dynamic and possibly non-linear deformation and propagation modes [42,49,120].

The paper is organized as follows. After introducing the simulation method in section 2, the preparation of our samples is discussed in section 3. Sound propagation through densely packed granular systems and its dependence on friction and adhesion is examined in section 4.1, while sound propagation for

different states of compression and failure is reported in section 4.2. Summary and Conclusions are given in section 5.

4.2.2 Discrete Particle Model

To simulate packing, failure and sound propagation in a granular material we use a Discrete Element Model (DEM) [9,24,40,56,71,110,112]. Such simulations can complement experiments on small scale by providing deep and detailed insight into the kinematics and dynamics of the samples examined. In the following we briefly introduce the method that allows us to simulate wave propagation in (damaged) packings. The numerics and algorithms are described in text-books [2, 87, 88], so that we only discuss the basic input into DEM, i.e., the contact force models and parameters. More details on the the contact model can be found in Ref. [71] and references therein.

The pairwise inter-particle forces typically used are based on the overlap and the relative motion of particles. This might not be sufficient to account for the inhomogeneous stress distribution inside the particles and possible multi-contact effects. However, this simplifying assumption enables us to study larger samples of particles with a minimal complexity of the contact properties, taking into account phenomena like non-linear contact elasticity, plastic deformation, and adhesion as well as friction, rolling resistance, and torsion resistance. In the following we will neglect rolling and torsion resistance however.

Normal Contact Forces

Realistic modeling of the deformations of two particles in contact with each other is already quite challenging. The description of many-body systems where each particle can have multiple contacts is extremely complex. We therefore assume our particles to be non-deformable perfect spheres. They shall interact only when in contact. We call two particles in contact when the distance of their centers of mass is less than the sum of their radii. For two spherical particles i and j in contact, with radii a_i and a_j, respectively, we define their overlap

$$\delta = (a_i + a_j) - (\boldsymbol{r}_i - \boldsymbol{r}_j) \cdot \boldsymbol{n} > 0 \tag{4.11}$$

with the unit vector $\boldsymbol{n} := \boldsymbol{n}_{ij} := (\boldsymbol{r}_i - \boldsymbol{r}_j)/|\boldsymbol{r}_i - \boldsymbol{r}_j|$ pointing from j to i. $\boldsymbol{r}_i$ and $\boldsymbol{r}_j$ denote the position of particle i and j, respectively.

The force on particle i, labeled $\boldsymbol{f}_i$, is modeled to depend pairwise on all particles j with which particle i is in contact, $\boldsymbol{f}_i = \sum_j \boldsymbol{f}^c_{i|j}$, where $\boldsymbol{f}^c_{i|j}$ is the force on particle i exerted by particle j at contact c. The force $\boldsymbol{f}^c_{i|j}$ can be decomposed into a normal and a tangential part, $\boldsymbol{f}^c_{i|j} = f^n_{i|j}\boldsymbol{n} + f^t_{i|j}\boldsymbol{t}$, where $\boldsymbol{n} \cdot \boldsymbol{t} = 0$.

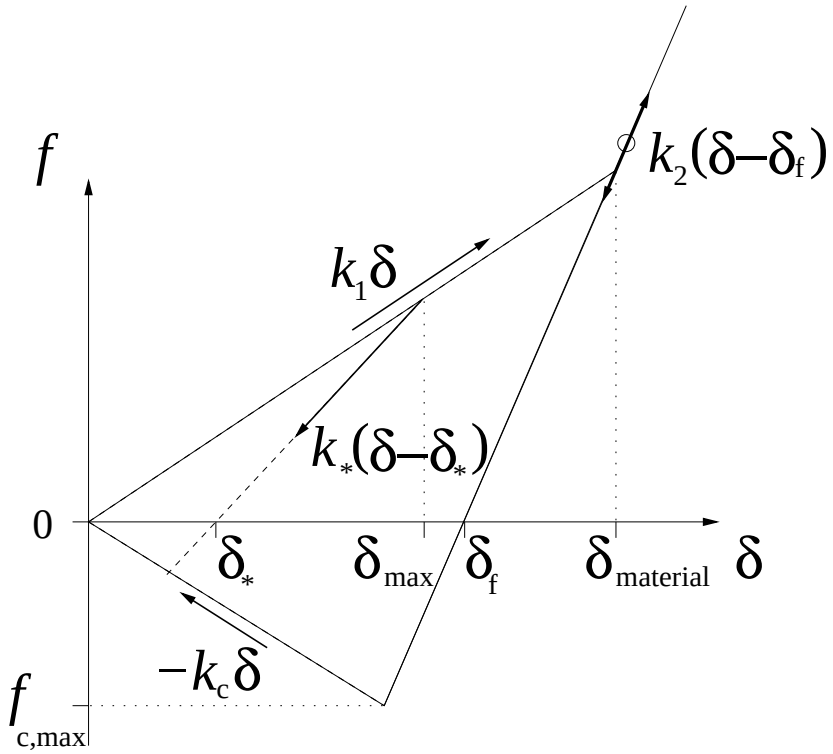

Figure 4.10: Spring part of the normal component of the contact force f^n, i.e. the part that is a function of the overlap δ. (The viscous normal forces are not included in this plot.) k_1, k_2, k_c, and δ_{material} are material constants. $\delta_{\max}$ is the maximum overlap this contact has encountered in the past and accounts for the history dependence of the contact law. δ_* is the (history dependent) overlap at which the force becomes zero when loading or unloading with the current (history dependent) stiffness k_*. δ_f is the overlap at which the force vanishes when the stiffness constant k_2 is used (at large overlaps).

To model the force $\boldsymbol{f}^c_{i|j}$ we use an adhesive, elasto-plastic, history-dependent contact law that depends on three variables only and is described in more detail in Ref. [71]: The force between two spheres is modeled to depend only on their overlap δ, the relative velocity of their surfaces, and the maximum overlap $\delta_{\max}$ this contact has suffered in the past. We will leave out the index $i|j$ from now on.

For the normal force f^n we apply a modified spring-dashpot model: The dashpot part is, as usual, a viscous damping force that depends on the normal component of the relative velocity. The spring "constant" k, however, is only temporarily constant and depends on the history of the contact, changing the force from linear in the overlap to piecewise linear: The repulsive force during

initial loading is governed by the initial loading stiffness constant k_1, see Fig. 4.10. When the contact is unloaded the maximal overlap $\delta_{\max}$ is kept in memory as a history variable. The forces during un- and reloading can be either repulsive or attractive and are determined using a linear interpolation k_* between the initial loading stiffness constant k_1 and the maximal elastic stiffness constant k_2. For overlaps greater than δ_{material} the stiffness constant k_2 is used. When reloading starts after unloading $\delta_{\max}$ is reset to the then current value of δ and it is subsequently increased again during loading. If a contact breaks $\delta_{\max}$ is set to zero. Each contact can be unloaded into the attractive regime with the current stiffness k_*. This models adhesion. The attractive forces are limited by $-k_c\delta$, with the adhesion "stiffness" constant k_c.

Tangential Contact Forces

In the tangential direction, the forces and torques depend on the tangential displacement and the relative rotations of the particle surfaces. Dynamic (sliding) and static *friction* depend on the tangential component of the relative velocity of the contact points,

$$\boldsymbol{v}_t = \boldsymbol{v}_{ij} - \boldsymbol{n}(\boldsymbol{n}\cdot\boldsymbol{v}_{ij}) \ , \text{ where } \quad \boldsymbol{v}_{ij} = \boldsymbol{v}_i - \boldsymbol{v}_j + a_i'\boldsymbol{n}\times\boldsymbol{\omega}_i + a_j'\boldsymbol{n}\times\boldsymbol{\omega}_j \tag{4.12}$$

is the relative velocity of the particle surfaces at contact. Here $a_\alpha' = a_\alpha - \delta/2$, for $\alpha = i, j$, is the corrected radius relative to the contact point. $\boldsymbol{v}_i$, $\boldsymbol{v}_j$, $\boldsymbol{\omega}_i$, and $\boldsymbol{\omega}_j$ are the linear and rotational velocities of particles i and j, respectively.

Tangential forces f^t acting on the contacts are modeled to be proportional to the accumulated sliding distance of the contact points along each other with a (tangential) stiffness constant k_t, i.e. $f^t = k_t \int v_t dt$, where v_t is the tangential component of the relative velocity of the contact point. Including also a viscous damping constant, γ_t, the tangential force is limited by the product of the normal force and the contact friction coefficient μ, according to Coulombs law, $f^t \le \mu f^n$. For more details see Ref. [71].

Background Friction

Viscous dissipation as mentioned above takes place localized in a two-particle contact only. In the bulk material, where many particles are in contact with each other, this dissipation mode is very inefficient for long-wavelength cooperative modes of motion, especially when linear force laws are involved [61]. Therefore, an additional damping with the background is introduced, such that the total force $\boldsymbol{f}_i$ and torque $\boldsymbol{q}_i$ on particle i are given by

$$\boldsymbol{f}_i = \sum_j \left(f^n\boldsymbol{n} + f^t\boldsymbol{t}\right) - \gamma_b\boldsymbol{v}_i \quad \text{ and } \quad \boldsymbol{q}_i = \sum_j \boldsymbol{q}^{\text{friction}} - \gamma_{br}a_i^2\boldsymbol{\omega}_i \ , \tag{4.13}$$

where the sums take into account all contact partners j of particle i, and γ_b and γ_{br} are the (artificial) background damping viscosities assigned to the translational and rotational degrees of freedom, respectively. The viscosities can be seen as originating from a viscous inter-particle medium and enhance the damping in the spirit of a rapid relaxation and equilibration. Note that the effect of γ_b and γ_{br} should be checked for each set of parameters: it should be small in order to exclude artificial over-damping.

Contact model Parameters

In the following we measure lengths in units of millimeters (mm), masses in milligrams (mg) and times in units of one hundred microseconds (100 μs). Note that only a few parameters have to be specified with dimensions, while the others are expressed as dimensionless ratios in Tab. 4.1.

Property	Symbol	Value	dimensional units	SI-units
Time unit	t_u	1	$100\,\mu$s	10^{-4} s
Length unit	x_u	1	1 mm	10^{-3} m
Mass unit	m_u	1	1 mg	10^{-6} kg
Particle radius	a_0	0.005	$5\,\mu$m	5.10^{-6}m
Material density	ρ	2	2 mg/mm^3	2000 kg/m^3
Max. load/unload stiffness	k_2	5	$5\,\text{mg}/(100\mu\text{s})^2$	5.10^2 kg/s^2
Initial loading stiffness	k_1/k_2	0.5		
Adhesion "stiffness"	k_c/k_2	0.2		
Tangential stiffness	k_t/k_2	0.2		
Coulomb friction coefficient	$\mu = \mu_d = \mu_s$	1		
Dynamic to static friction	$\phi_d = \mu_d/\mu_s$	1		
Normal viscosity	$\gamma = \gamma_n$	5.10^{-5}	5.10^{-5} mg/100μs	5.10^{-7} kg/s
Tangential viscosity	γ_t/γ	0.2		
Background viscosity	γ_b/γ	4.0		
Background viscous torque	γ_{br}/γ	1.0		
Fluid overlap	ϕ_f	0.05		

Table 4.1: Microscopic material parameters used (third column), if not explicitly specified. The fourth column contains these values in the dimensional units, i.e., when the time-, length-, and mass-units are 100 μs, mm, and mg, respectively. Column five contains the parameters in SI-units. Energy, velocity, force, acceleration, and stress have to be scaled with factors of 10^{-4}, 10^{-1}, 10^{-1}, 10^5, and 10^5, respectively, for a transition from reduced to SI-units.

A maximal stiffness constant of $k_2 = 5$, as used in our simulations, corresponds to a typical contact duration (half-period) $t_c \approx \sqrt{m/(2k)} \approx 6.5 \times 10^{-4}$, for a normal collision of a large and a small particle with $\gamma = 0$. Accordingly, an integration time-step of $t_{\mathrm{MD}} = 5 \times 10^{-6}$ is used in order to allow for a "safe" integration of the equations of motion. Note that not only the normal "eigenfrequency" but also the eigenfrequencies for the rotational degrees of freedom have to be considered, as well as the viscous response times $t_\gamma \approx m/\gamma$. All of the (inverse) eigenfrequencies should be considerably larger than t_{MD}, while the viscous response times should be even larger, so that $t_\gamma > t_c \gg t_{\mathrm{MD}}$. A more detailed discussion of all the effects due to the interplay between the model parameters and the related times is, however, far from the scope of this paper. Details can be found in Ref. [71] and references therein.

4.2.3 Tablet preparation and material failure test

Tablet preparation

Having introduced the model and its parameters in the last section here we describe the experimental idea and the steps of our simulations. We prepare a "tablet" (granule) consisting of primary particles that behave according to the contact force laws mentioned above. A four-step process is applied:

- creation of a loose initial sample
- pressure sintering by isotropic compression
- removal of the pressure
- relaxation

On the resulting unconfined "tablet", or material sample, tests can be performed, e.g. controlled compression or tensile tests as well as sound wave propagation tests. Care has to be taken to perform first the preparation and later the tests in a symmetric way (see below) to avoid artifacts.

Initial sample: Before sintering the first step is to *create a loose configuration* of $N = 1728$ spherical (granular) particles with a Gaussian distribution of radii with average $a = 0.005$. The tails of the distribution are cut off at 0.003 and 0.0075 to ensure that all particles are comparable in size [26], i.e. neither too large nor too small particles are desired. For the situations presented in this paper, the half-width of the distribution is $w_a = \sqrt{\langle a^2 \rangle - \langle a \rangle^2} = 0.0007213$. In addition, the initial velocities are drawn from a Gaussian distribution in each direction.

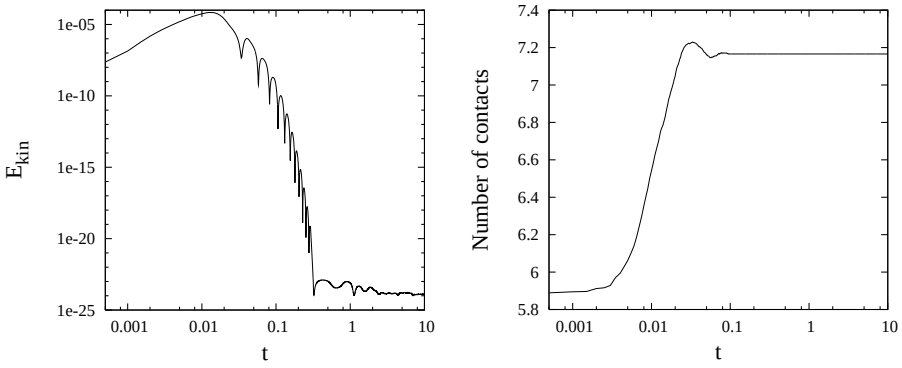

Figure 4.11: Kinetic energy E_{kin} (left) and coordination number [number of contacts per particle] (right) as a function of time t during isotropic pressure sintering with final pressure $p_s = 10$. Here the particle contacts are adhesionless, $k_c = 0$, while the other parameters are given in Tab. 4.1

In the initial preparation stage the particles are arranged on a regular cubic lattice with wide spacing so that particles are not in contact – neither with each other nor with a wall – and have space to move and become disordered. Then the system is compressed with a pressure of $p_1 = 0.5$ to create a loose initial packing with a coordination number $\mathcal{C} = 5.89$ and volume fraction, $\nu = \sum_i V(a_i)/V = 0.607$, with the particle volume $V(a_i) = (4/3)\pi a_i^3$.

Pressure sintering: The second step is *pressure sintering*: The system is compressed by keeping one wall in each spatial direction fixed while applying a constant pressure of $p_s = 10$ to the other (three) walls. During compression, the particles are frictional with a friction coefficient $\mu = 1$, and have zero adhesion amongst each other, i.e. $k_c = 0$. Four of the six walls are frictionless $\mu^{\text{wall}} = 0$ and cohesionless ($k_c = 0$). The remaining two (opposing) walls are already prepared for the tests to come. These two walls define the uniaxial direction and are strongly adhesive, with $k_c^{\text{wall}}/k_2 = 20$, so that the sample sticks to them, while all other walls can be easily removed in the third step. The wall-adhesion has no visible effect here, since the sample is strongly confined. In contrast, friction has an effect, i.e. friction with the walls would hinder the pressure to be transferred completely to its opposite wall. Frictional walls carry part of the load – an effect that is known since the early work of Janssen [46, 103].

During the compression the kinetic energy first increases and then decreases, see the left graph of Fig. 4.11, due to the energy dissipation in the system. We keep the pressure constant until the kinetic energy has very well reached a small constant value, within fluctuations, determined only by the numerical accuracy.

The right graph of Fig. 4.11 shows the mean coordination number as a function of time. The number of contacts increases during pressure sintering, overshoots, and finally settles to a constant value of $\mathcal{C} \approx 7.17$. Not surprisingly, a rather high volume fraction, $\nu = 0.6754$, is reached during the pressure sintering. After stress-relaxation (see below), these values decrease considerably to $\nu \approx 0.626 \pm 0.005$ and $\mathcal{C} \approx 6.2 \pm 0.2$, depending on the material parameters used.

Pressure release: Using this pressure sintered sample, the third step is to *remove the pressure* from the walls. Before we do so both k_c and μ are set to the desired values ($k_c/k_2 = 0.2$ or 1.0 and $\mu = 1.0$, 0.1, or 0.0). The combination of material parameters and their identification codes are summarized in Tab. 4.2.

Type	A	B	C	D	E	F
k_c	1	5	1	5	1	5
μ	1	1	0.1	0.1	0	0
ν	0.6270	0.6280	0.6296	0.6294	0.6273	0.6216
$\mathcal{C}$	6.097	6.183	6.020	6.191	6.122	6.454

Table 4.2: Adhesion and friction parameters used during stress-release and for the further tests of the samples A-F. The densities and coordination numbers are realized after relaxation, after stress-release, before the subsequent compression and/or sound tests.

The control pressure is smoothly released from the walls in a co-sinusoidal way, starting from its sintering value, $p_s = 10$, down to a residual value, p_0, that is five orders of magnitude lower, i.e. $p_0/p_s = 10^{-5}$. The half period of the co-sinusoidal pressure release is $t_0 = 12.5$, but relaxation is continued further until the kinetic energy is dissipated and reaches tiny values, see Fig. 4.12. The small residual pressure keeps single particles from leaving the sample and also keeps the walls in place. This is important in order to not spoil the efficiency of our linked cell algorithm, where the cell size is a fraction of the system size between the walls. However, this confining stress p_0 is not big enough to affect the dynamics of the tests performed, it is just a convenient way to keep the walls rather close to the sample. ($p_0/p_s = 10^{-3}$ leads to very similar results.)

There are qualitative differences for the short time behavior between the samples A and B on the one hand and samples C – F on the other hand. In the latter samples the friction coefficient is suddenly reduced from $\mu = 1$ to smaller values just before the walls are removed. As an example, in Fig. 4.12 samples A and C are compared, which have $\mu = 1$, and 0.1, respectively. The kinetic energy of sample C increases instantaneously due to the "failure" of several contacts and

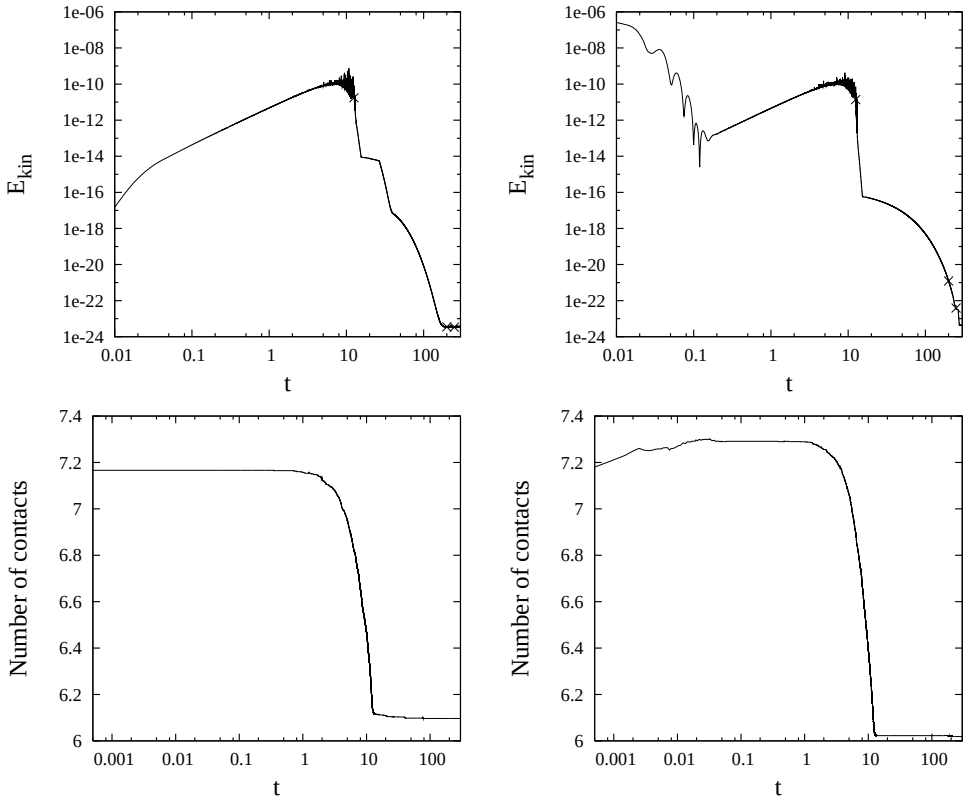

Figure 4.12: Kinetic energy E_{kin} (top) and coordination number [number of contacts per particle] (bottom) as a function of time t during stress-removal from the walls and subsequent relaxation. The material parameters are given in Tab. 4.1, for sample A (left), with $\mu = 1$, while the friction is reduced to $\mu = 0.1$ for sample C (right). The markers (top) show the the changes discussed in the text at times 12.5, 200, and 250.

subsequent dynamic reorganization. During this reorganization also the coordination number, see bottom panels in Fig. 4.12, increases slightly, as well as the density (data not shown). For sample E, the increase in kinetic energy, coordination number and density is larger, since the friction is reduced to an even smaller value $\mu = 0$ (data not shown).

A comparison of samples B, D, and F leads to qualitatively similar observations as did the comparison of samples A, C, and E discussed above. The sudden reduction of friction has the same effect when $k_c = 5$ instead of $k_c = 1$. The increase in adhesion from $k_c = 1$ to $k_c = 5$ does not show a strong effect initially. Only for larger times, i.e. lower pressure, the effect of contact adhesion manifests itself in slightly shorter relaxation times. All densities are very similar, only the coordination number is systematically slightly larger for stronger adhesion.

Final relaxation: The fourth preparation step is the *final relaxation* of the system. This is done in three sub-steps. First, immediately after the control pressure on the wall has reached its low residual value, the system is relaxed further until time $t_{r1} = 200$ with three fixed walls and three walls with the residual pressure reached at the end of the wall removal procedure. Second, after the kinetic energy has reached a small value, within fluctuations, for a long time, the system is further relaxed and symmetrized with the same pressure of 10^{-4} applied from *all* sides for another time interval of $t_{r2} = 50$. In the final relaxation step, again a time interval of $t_{r3} = 50$, the two walls in the x-direction are fixed and the other four walls are kept at the residual pressure. We now have an unconfined sample with fixed walls in the x-direction and negligible stresses in all directions. The tests to be performed are uniaxially deforming the walls in the x direction only.

The prepared sample can now be used for all sorts of further tests. In this paper we will show compression tests in the next subsection 4.2.3 and sound wave propagation on different samples in section 4.2.4, as sketched in Fig. 4.13.

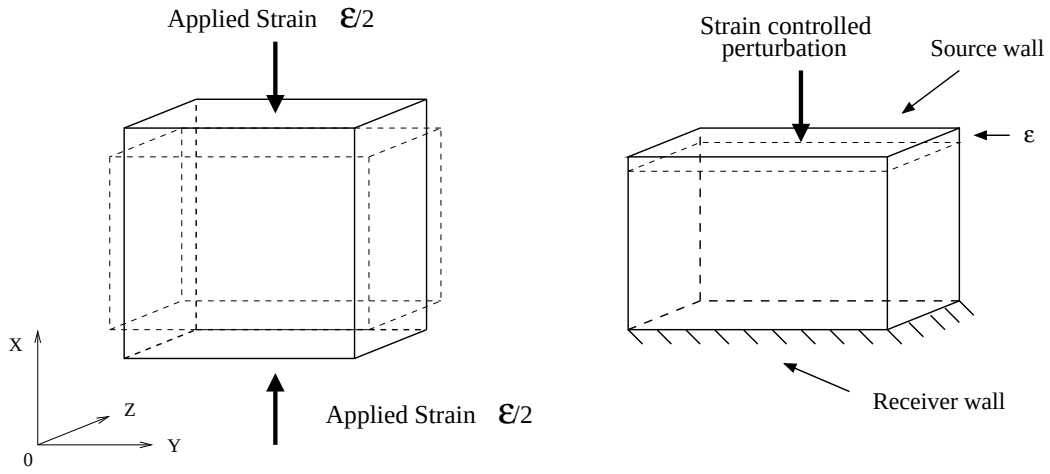

Figure 4.13: Sketches of the compression (left) and the wave propagation (right) tests

Compression test

In this section we describe an uniaxial unconfined compression test, starting from the final configuration of sample A from the previous subsection. This test resembles a direct measurement of the unconfined yield-strength, as applied in mechanical engineering and particle technology, see [97]. However, we apply the strain in several rather small steps. After each small step we relax the system

in the compressed state, i.e. we run the simulation for a while without changing the pressure (y- and z-directions) on and positions (x-direction) of the walls. We later perform tests on these "relaxed" states. This must not be confused with a test performed after the stress has been removed.

Instead of applying the target-strain of $\epsilon_{max} = 0.0217$ in one sweep, the deformation is divided into 10 steps, with $\epsilon_s \approx 0.00217$ each (measured relative to the initial system size). This leads to states with $\epsilon_m = m\epsilon_s$, with integer $m = 0, 1, 2, ..., 10$. During each of the ten strain-steps, the system is compressed in a co-sinusoidal way for one half-period, during a time interval of $t_\epsilon = 0.5$, and then relaxed for a time interval of $t_{\epsilon r} = 4.5$. Note that the results are rate dependent (where the rate is proportional to $1/t_\epsilon$). A small enough rate has to be chosen in order to stay in the quasi-static regime. Fig. 4.14 gives a comparison with a ten times higher rate (left graph). A four times higher rate does not change qualitatively the stress-strain behavior (data not shown here). The "relaxed" sample (which is still under anisotropic pressure) is then further deformed and relaxed and this is repeated again and again. The reason for this intermediate relaxation is that we want to perform sound wave propagation tests on well-defined "relaxed", static samples after those have suffered from different levels of deformation.

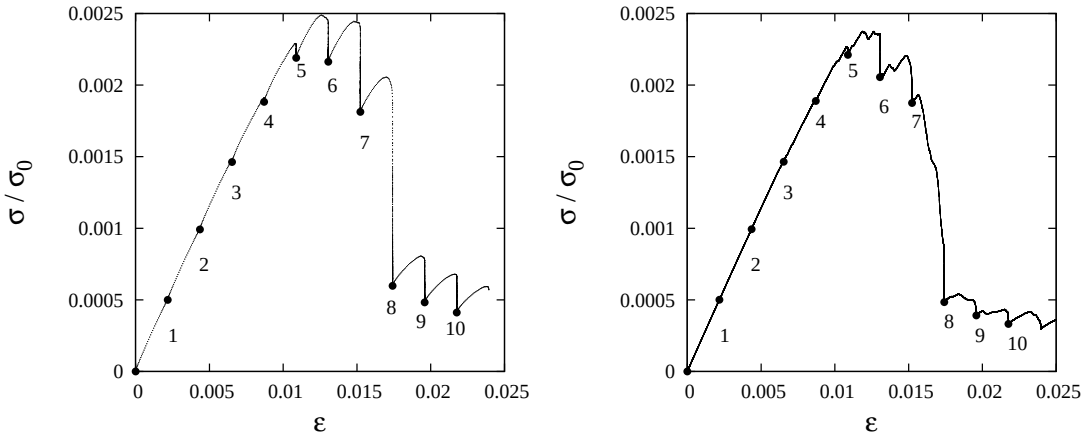

Figure 4.14: Normalized axial stress σ/σ_0 plotted against the axial strain ϵ from a step-wise uni-axial compression test. The reference stress, $\sigma_0 = k_2/a$, is used to get a dimensionless stress. The left graph shows the results for a rate ten times faster than the one used in the following (right graph). The points indicate the configurations on which sound propagation tests are performed in Sec. 4.2.4.

The stress-strain diagram of this compression test is shown in Fig. 4.14. The initial stress-strain relation is very close to linear, with a slope of $D = \partial\sigma/\partial\epsilon = 225.6$. The maximal stress in is approximately 1/4 of the previously applied

sintering pressure p_s. Additionally, we see that relaxing the system in the elastic regime, at intermediate strains of ϵ_{1-4}, leads to samples very close to the elastic branch. Thus up to a strain of about one percent the system behaves almost like an elastic solid. Tab. 4.3 summarizes the strains, coordination numbers, and volume fractions for all ϵ_m investigated.

	ϵ_0	ϵ_1	ϵ_2	ϵ_3	ϵ_4	ϵ_5	ϵ_6	ϵ_7	ϵ_8	ϵ_9	ϵ_{10}
ϵ	0	0.22	0.43	0.65	0.87	1.09	1.30	1.52	1.74	1.95	2.17
C	6.097	6.098	6.093	6.090	6.086	6.001	5.810	5.592	4.679	4.612	4.556
ν	0.627	0.627	0.627	0.624	0.620	0.613	0.594	0.578	0.546	0.537	0.526

Table 4.3: Strain steps ϵ_m and corresponding coordination numbers and volume fractions. The round-off error for the given values is $\pm 10^{-3}$

At larger deformation, ϵ_5, the sample starts to fail: Here the stress is close to its maximum and during the relaxation the stress decreases, i.e. we have left the elastic regime. The coordination number and density decrease considerably when the sample starts to fail. At the next strain levels, ϵ_6, and ϵ_7, the stress remains large but the stress decreases more and more during relaxation. At $\epsilon_8 \approx 0.017$ the system fails and becomes almost fluid-like with an enormous decay of stress during relaxation. Also for later compression steps the stress is significantly reduced, relative to the maximum, during the relaxation process, though it never reaches zero.

4.2.4 Sound wave propagation tests

The goal of this section is to characterize how the propagation of sound waves is influenced by, on the one hand, the "microscopic" parameters such as the inter-particle cohesion and friction and, on the other hand, the material state (uncompressed, uniaxially compressed in the elastic regime, close to failure, or in the fluidized softening regime). This is done by analyzing the wave propagation, phase velocities, damping, and Fourier spectra of the sound waves propagating through the system.

The "microscopic" inter-particle interaction laws (material properties) have an influence on the propagation of sound. Therefore we first probe packings with different "microscopic" adhesion and friction parameters. When a tablet undergoes strain, both microscopic (contact scale) and macroscopic (multi-grain scale) changes occur in the structure. In order to investigate the change of the macroscopic material properties due to these reorganizations we probe the packing at various externally applied uniaxial strains, corresponding to the different

regimes mentioned above. Note that a piecewise linear contact law with history-dependent stiffness (see Sec. 4.2.2) allows to decouple the non-linearity of the contact forces (as in the case of the Hertz contact model for example) from the influence of reorganizations and opening or closing of contacts.

For the sound propagation tests we start with the tablets prepared as described in Sec. 4.2.3. The tablet has two fixed walls in the $x-$ direction and virtually free boundary conditions in the other two directions. Now a signal is sent through the sample by applying a time-dependent variation of the position (according to the desired signal) to one of the two walls, see left sketch of Fig. 4.13. After some time the opposite wall will feel a stress variation which we analyze and interpret, right sketch of Fig. 4.13. The wave form is a full period of a co-sine, moving the wall in and out, with an amplitude, $A = 10^{-7}$ and a time period $T = 3.\,10^{-3}$. This stress amplitude is much smaller than the maximum stress in Fig. 4.14.

Influence of cohesion and friction on sound propagation

In this subsection the influence of the microscopic parameters adhesion and friction on the sound propagation of an uncompressed tablet is studied. In Tab. 4.2 the values used for inter-particle adhesion k_c and friction μ are given along with the sample names A, B, C, D, E, or F. In Fig. 4.15, the source (left) and receiver (right) signals (stress at the wall) are plotted versus time. Tab. 4.4 gives the wave velocities, calculated for different reference points as specified below, and the damping ratios between the source and receiver signals.

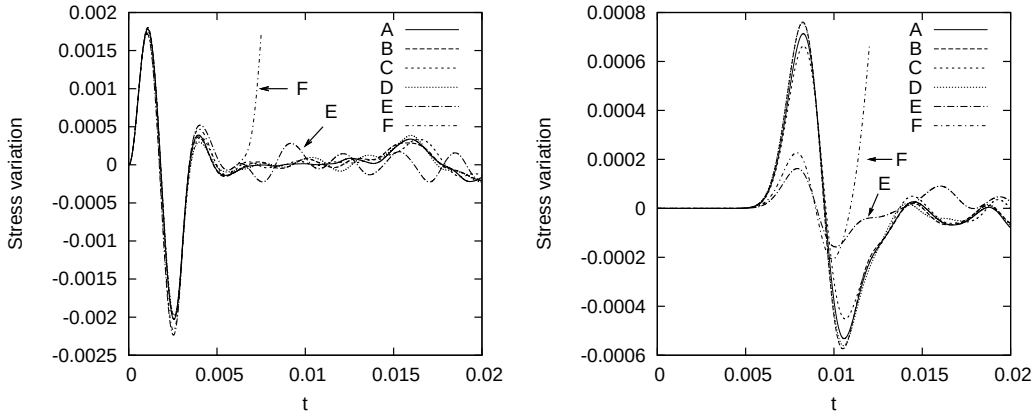

Figure 4.15: Stress variation $\sigma(t) - \sigma(0)$ as function of time t at the source and receiver walls for the samples prepared in Sec. 4.2.3. Here $\sigma(0)$ denotes the pressure at the wall just before the sound propagation test started. Note the different vertical axes. The signal for sample F has been cut off as it oscillates strongly later on.

	A	B	C	D	E	F
v_5	19.6	19.63	19.6	19.69	20.23	20.24
v_{10}	18.89	18.94	18.91	18.99	19.52	19.55
v_m	15.99	16.05	15.95	16.07	16.62	16.7
v_0	14.94	15.04	14.84	15.03	15.71	15.86
σ_d	2.49	2.37	2.65	2.35	10.59	7.67

Table 4.4: Velocities, v, as defined in the main text and damping σ_d.

Wave velocities are deduced from the time of flight (TOF). Therefore a reference point is chosen at the maximum of the peak (leading to the velocity v_m), at 5% of that maximum (v_5), at 10% of that maximum (v_{10}) or finally when the signal reaches for the first time zero amplitude after the peak (v_0). The ratio of the distance between the two walls (source and receiver) and the time difference between the two signals gives the desired wave velocities. Note that since the medium is dispersive, the calculated velocities are an approximation of the group velocity for the range of propagating frequencies.

The damping ratios σ_d are calculated by dividing the maximum of the peak of the source signal by the corresponding peak of the receiver signal. Those ratios depend on the distance between the two walls and on the dispersion.

The results show a clear difference between the specimens with friction (A, B, C, and D) and the frictionless cases (E and F) concerning both damping and velocities. The damping (as defined above) is significantly stronger for cases E and F. This may be due to the fact that friction strengthens the specimen and hence enhances the wave transmission, i.e. reduces damping in accordance with previous results [79]. The strong reduction in the peak amplitude of the frictionless samples might also be related to the different configuration structure of the samples. For the frictional specimens (A – D) the damping is lower for higher adhesion (B and D). The same is observed for frictionless specimens, which means that stronger adhesion enhances the wave transmission as well.

Concerning the velocities, for the same inter-particle adhesion, A, C & E and B, D & F, all velocities are systematically lower in the frictional cases (A – D) than in the frictionless samples (E and F). In a previous study [79] the velocity of sound was higher in the frictional case, where identical samples were prepared without friction before activating the desired friction coefficient. This is in contrast to our results, where all samples are different. However, a complex interplay between frictional and cohesion effects might be the explanation for this unexpected result. Finally, when comparing specimens A and C with specimens B and D, there is a slight increase of velocities with higher cohesion. The same is

observed when comparing specimens E and F. This suggests again that adhesion increases the effective stiffness of the material and thus the wave speed. The fact that adhesion increases the tensile strength was examined and reported in [71,72]. Note that the increase of velocity is correlated with the increase of coordination number for increasing contact adhesion and thus depends on the history of the sample.

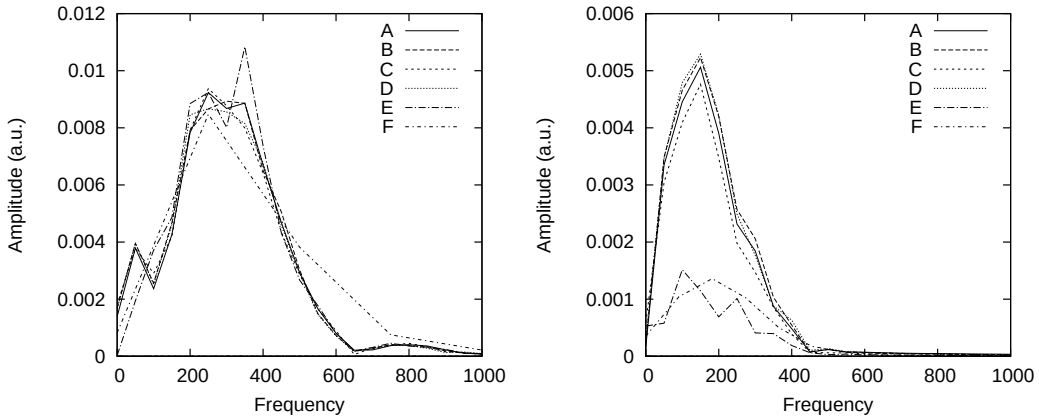

Figure 4.16: Power spectrum from (left) source- and (right) receiver-signals, taken from the simulations in Fig. 4.15 in arbitrary units (a.u.). Only signals E and F behave differently from the others, reflecting their higher damping rates (see right graph).

From the power spectra, obtained by applying the Fourier transform to the time signals, the dispersive and filtering behavior of the system can be identified by the observed significant shift of the main frequency from about 330 down to 150 (corresponding to 33 kHz and 15 kHz in SI-units), see Fig. 4.16. The granular, and hence inhomogeneous and discrete, nature of the system leads to its dispersive behavior. High frequencies are very sensitive to the details at the grain scale because their wavelengths are small, and hence they travel more slowly and less far than lower frequencies. The latter ones are less sensitive to the details at the grain scale because their wavelengths are much larger and average over many grains. Note that the main frequency at around 330 comes from the chosen period for the wave form, $T = 3.\,10^{-3}$, see the beginning of Sec. 4.2.4. Besides the evidently strong damping of signals E and F, no further striking differences are observed for the different specimens' spectra. Even though there are differences in the power law tail of the spectra (data not shown), we could not correlate those to the different parameters.

Uncompressed versus compressed states

In the following, the compressed specimen A (uniaxially, from both sides) is used. In that special direction the wall movement is strain controlled and the other two directions are virtually free boundaries, see Sec. 4.2.3 for details. At each step of the compression test, after relaxation, see Fig. 4.14, a sound wave is sent through the system the same way as in the previous subsection. Fig. 4.17 shows the signals at the source and receiver walls.

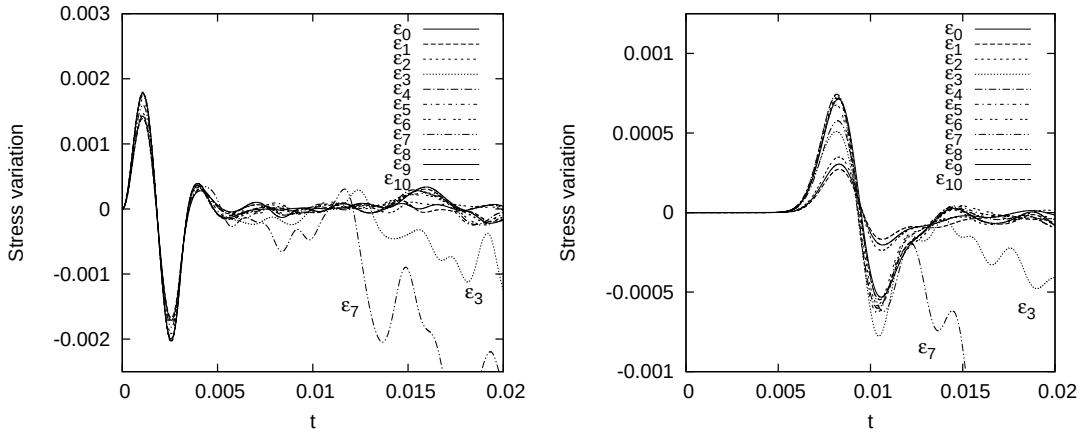

Figure 4.17: Stress variation $\sigma(t) - \sigma(0)$ as function of time t at the source and receiver walls, where the ϵ_3 and ϵ_7 signals display a different coda. Note the different vertical axes.

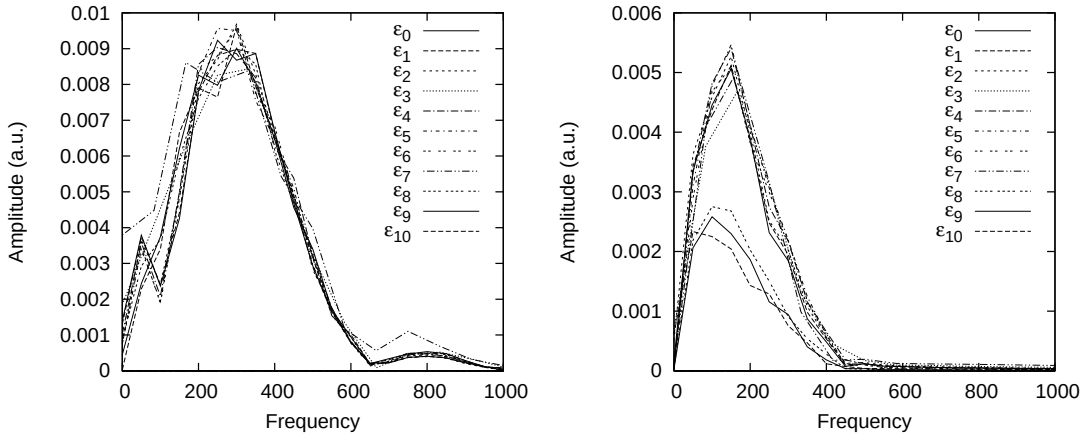

Figure 4.18: Power spectra from source- and receiver-signals, taken from the simulations in Fig. 4.17 in arbitrary units (a.u.).

	ϵ_0	ϵ_1	ϵ_2	ϵ_3	ϵ_4	ϵ_5	ϵ_6	ϵ_7	ϵ_8	ϵ_9	ϵ_{10}
v_5	19.6	19.59	19.6	20.00	19.58	19.56	19.55	19.45	19.26	19.24	19.14
v_{10}	18.89	18.89	18.89	19.31	18.88	18.87	18.85	18.74	18.55	18.52	18.45
v_m	15.99	16.01	16.03	16.13	16.05	16.06	16.04	15.84	15.66	15.58	15.54
v_0	14.94	14.99	15.05	15.22	15.10	15.14	15.14	14.81	14.56	14.46	14.39
σ_d	2.49	2.47	2.47	3.47	2.37	2.37	2.45	2.76	4.21	4.68	5.11

Table 4.5: Velocities, v, as defined in the main text and damping σ_d

Regarding v_m and v_0, see Tab. 4.5, the velocities seem to increase a little as the system is further compressed until state ϵ_3. Then they slightly decrease until state ϵ_6 and finally the decay is stronger until the last state ϵ_{10}. This variation correlates with the three regimes observed on the stress-strain curve, see Fig. 4.14, i.e. first the close-to-linear regime, second, the start-of-failure regime, and finally the critical-flow regime. The damping strongly increases for the last steps, ϵ_8 to ϵ_{10}, as the sample is not really a solid any more. These observations correlate with the given coordination numbers C and the density ν, see Tab. 4.3. Similar observations are made concerning the power spectra of those signals, see Fig. 4.18, noting a stronger damping at steps ϵ_8 to ϵ_{10}. Additional studies are needed to determine whether the sound pulse method could allow for a sensitive material state characterization at all.

4.2.5 Conclusions

We have performed particle simulations of sound propagation in isotropically pressure sintered powder samples at very small confining stress. Using a recently proposed piecewise linear contact model for particle-particle interactions we probed different values of friction and adhesion during preparation. In particular, we applied a P-wave on one end of the sample and measured and analyzed the signal on the opposing receiver wall. Surprisingly we found only very weak differences except for the frictionless case, where the velocity of sound was higher and the damping was stronger. Even though the samples were prepared using the same preparation protocol they evolved to different initial configurations due to different values of the contact parameters. The material behavior is history dependent but mostly determined by the sintering pressure p_s rather than by those material parameters varied here.

In addition, one of the samples was subjected to strain-controlled uniaxial unconfined compression and the sound propagation properties were studied at various levels of strain: In the elastic regime, at the onset of and during failure,

and in the softening and flowing regimes. Even though in the elastic regime we found astonishingly little variation in the wave propagation velocity as a function of the strain, one particular sample behaved qualitatively different. In the softening regime all samples were unstable even though the amplitude of the probing pulse was 100 times smaller than the typical particle-particle overlap.

Having observed rather small differences between the different uniaxial strain states, the expected dependence of sound propagation on the uniaxial anisotropic stress states studies was not observed.

The quantitative tuning of the DEM model to real experimental data remains a challenge for future research. The results presented here have units that are not supposed to mimic a real material. Some tuning can be done by re-scaling, but a real fine-adjustment will require a more systematic study of other contact model parameters.

Acknowledgements

Valuable discussions with J. Tomas, A. Suiker, L. Brendel, and W. Mulder are appreciated. This study was supported by the Delft Center for Materials Self-Healing program, the research institute IMPACT of the University of Twente, and the Stichting voor Fundamenteel Onderzoek der Materie (FOM), financially supported by the Nederlandse Organisatie voor Wetenschappelijk Onderzoek (NWO), through the FOM-SHELL program and the Granular Matter program.

5

Effect of disorder on wave propagation

5.1 Systems with tiny polydispersity

This article, with the original title "Sound wave propagation in weakly polydisperse granular materials" *by Orion Mouraille and Stefan Luding, has been published in the Journal Ultrasonics [81].*

Abstract

Dynamic simulations of wave propagation are performed in dense granular media with a narrow polydisperse size-distribution and a linear contact-force law. A small perturbation is created on one side of a static packing and its propagation, for both P- and S-waves, is examined. A size variation comparable to the typically tiny contact deformation already changes sound propagation considerably. The transmission spectrum becomes discontinuous, i.e., a lower frequency band is transmitted well, while higher frequencies are not, possibly due to attenuation and scattering.

This behavior is qualitatively reproduced for (i) Hertzian non-linear contacts, for (ii) frictional contacts, (iii) for a range of smaller amplitudes, or (iv) for larger systems. This proves that the observed wave propagation and dispersion behavior is intrinsic and not just an artifact of (i) a linear model, (ii) a frictionless packing, (iii) a large amplitude non-linear wave, or (iv) a finite size effect.

5.1.1 Introduction

The stress-wave (sound) propagation through dense granular matter is the superposition of many complex phenomena, which are caused by the discrete, in-

homogeneous, anisotropic and dissipative structure of this class of materials on the microscopic, contact scale [20, 42, 49, 58, 101]. Non-linear contacts [92, 106], force-chains [66], frequency-dependence [85, 118] and also scattering and attenuation in other "particle type" materials [27] are reported. Ballistic pulse propagation can co-exist with a slower multiply scattered, coda-like signal [48, 49], and the stress- and frequency-dependence of the wave propagation features are subject of ongoing discussion [42, 49] in static and shaken packings as well.

A continuum description of granular materials is generally needed in field applications (like oil recovery) due to the huge system-size. On this macroscopic scale, the properties of such waves are strongly affected by phenomena like attenuation, scattering, and dispersion [49]. Starting from simulations at the particle level, which are necessary to gain insight into the role of the micro-parameters, a "micro-macro" transition [1, 63] can provide a continuum, macroscopic description (at least for quasi-static deformations). The ultimate goal is to find micro-based macroscopic constitutive relations, superior to the empirical ones typically used, also for dynamic and possibly non-linear deformation and propagation modes [42, 49, 120].

The use of a three-dimensional discrete element method (DEM) [24, 71, 77, 79, 80, 92] allows the study of the role of various micro-parameters in detail. Except for a regular crystal structure of exactly equal sized particles, geometrical (and hence contact) disorder is intrinsic to granular systems. The wave propagation properties are examined in the following, starting from a regular structure and slowly increasing the amount of disorder involved. The system size and the amplitude are varied as well as the non-linearity and friction in order to understand their effect on the wave-propagation characteristics.

5.1.2 Simulation setup

Discrete particle Model

The elementary units of granular materials are mesoscopic grains, which deform locally under the forces/stresses acting at their contacts. Since the realistic modeling of the internal deformation of the particles is too expensive, the normal interaction force is only related to the "overlap" of two (spherical) particles, while the tangential forces involve an elastic and a frictional element. If the sum of all forces, f_i, acting on particle i, either from other particles, from boundaries or from external forces, is known, the problem is reduced to the integration of Newton's equations of motion for the translational and rotational degrees of freedom:

$$m_i \frac{\mathrm{d}^2}{\mathrm{d}t^2} \boldsymbol{r}_i = \boldsymbol{f}_i \ , \quad \text{and} \quad I_i \frac{\mathrm{d}}{\mathrm{d}t} \boldsymbol{\omega}_i = \boldsymbol{t}_i \ , \tag{5.1}$$

with the mass m_i of particle i, its position $\boldsymbol{r}_i$, its moment of inertia I_i, its angular velocity $\boldsymbol{\omega}_i$, and the total torque $\boldsymbol{t}_i$. Note that the above equation is only valid for isotropic bodies, like spheres as used in the following [71, 79].

A simple linear spring model is used for the normal force $|f| = k\delta$, with the contact stiffness k (=10^5 N/m), corresponding approximately to the stiffness of a Plexiglas bead, detailed below (Wave agitation paragraph). If the overlap is positive, the force acts, if the overlap is negative the force is $f \equiv 0$. For the simulations where friction is active, the force in the tangential direction, $\boldsymbol{f}_t$, is implemented in the spirit of Ref. [24] and in section 3.1.2, where a tangential spring (with stiffness $k_t = 0.2k$) was introduced to account for static friction [71]. The tangential contact forces are related to the normal forces via Coulomb's law, i.e., $f^t \leq \mu f^n$, with $\mu = 0.5$ for both sliding and sticking. In some simulations, a non-linear spring model (according to Hertz) was used, with the normal force $|f| = k_H \left(\delta^{3/2}\right)$, with $k_H = 4.5\ 10^7$ N/m$^{3/2}$.

Particle packing

The geometrical configuration considered in this study is a dense, static packing of grains, with radii a_0 (=0.001m), arranged in a Face Centered Cubic (FCC) structure (with density, i.e., volume fraction of $\nu \approx 0.74$), where square layers in the x-y-plane (4×4 particles) are stacked in the z-direction (200 layers), see Fig. 5.1 for a snapshot of a part of the system. The larger systems examined are double-sized in the cross-section (8×8 particles). This regular, ordered system is rather thin but elongated in the z-direction in order to allow the wave to propagate for some time, before it hits the wall on the opposite side. Each particle has four contacts inside each square-layer, and eight with particles in the neighboring layers (4 each), corresponding to a coordination number of $C = 12$. All particles have the same overlap $\overline{\delta}/a_0 \approx 10^{-3}$ and (due to periodic boundaries) "see" the same environment (except those in the first and last mobile layer).

Polydisperse packings are obtained by randomly changing the particle sizes according to a narrow size distribution, which is homogeneous, centered at a_0, and has a width $2(\Delta a)$ of the order of the mean overlap $\overline{\delta}$ and then allowing the system to relax to a new, slightly disordered equilibrium configuration with the same volume. More precisely four different cases, with $(\Delta a) = 0$, $\overline{\delta}/2$, $\overline{\delta}$ and $2\overline{\delta}$ are compared. Note that the polydisperse systems conserve their original FCC structure at the grain scale (almost), since the radius variation is much smaller than the particle sizes. However, strong differences are observed at the contact level. This is because a radius variation of $(\Delta a) = 2\overline{\delta}$, represents only a small change of 0.2% at the grain level, but a large change of 200% at the contact level. This has a direct influence on the coordination numbers, which drop down from

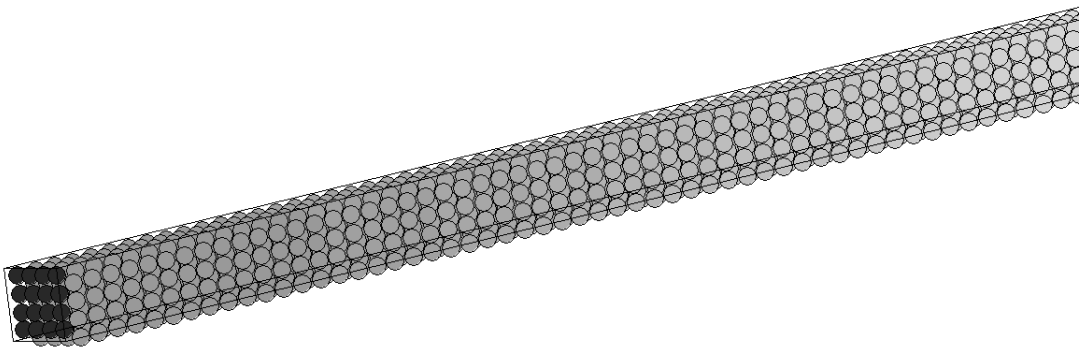

Figure 5.1: FCC-structured packing, thin (4×4 periodic) in the x- and y-directions, and elongated (non-periodic) in the z-direction; the black particles indicate the "zero-th" layer of fixed particles that make up the $z = z_0$ boundary.

$C = 12$ to $C \approx 11.99$, 11.22, and 9.97, for the three (Δa), respectively. For the last case this means a non-negligible reduction of about 17% of the total contacts of the monodisperse system. Since the effect of this "tiny" radius variation is so strong, polydispersity should be seen as related to the overlap rather than the particle size, as noted already in Ref. [62].

In order to examine the effect of more realistic contact models, one packing with $(\Delta a) = 2\overline{\delta}$ was relaxed with friction active, leading to an even smaller coordination number of $C \approx 9.64$. Another packing, also with $(\Delta a) = 2\overline{\delta}$ was relaxed using the Hertz contact-model, see section 5.1.2, so that, the coordination number was $C \approx 9.77$, somewhat lower than for the packing with the linear model ($C \approx 9.97$). Note that all these packings are still much more coordinated and denser than the theoretical isostatic limit cases of $C = 6$ and $C = 4$ for frictionless and frictional packings, respectively.

Wave agitation

In order to agitate a plane wave in z-direction, an initial velocity $\boldsymbol{v}$ is given to all the particles that make up the source, i.e., the first x-y-layer with $z = z_1$, in contact with the fixed particles at $z = z_0$. This velocity either points in z-direction, $\boldsymbol{v} = v_z\hat{\boldsymbol{z}}$, or in x-direction, $\boldsymbol{v} = v_x\hat{\boldsymbol{x}}$, creating a compressive (P), or a x-polarized shear (S) wave, respectively. If not mentioned explicitly, $v_z = v_x = 0.01\,\mathrm{m/s}$ are used, which create a maximum particle displacement $u_{max} \approx 5\,10^{-8}\,\mathrm{m}$ during the simulations. Relating the layer distance $l_z = z_1 - z_0 = \sqrt{2}a_0$ and the "contact duration" (Ref. [71]) $t_c \approx 2.03\,10^{-5}\,\mathrm{s}$, leads to a velocity $v_c = l_z/t_c \approx 70.7$ m/s. The chosen contact stiffness, k (=$10^5\,\mathrm{N/m}$), as mentioned earlier, corresponds to the stiffness of a Plexiglas bead. Meaning that this value is close to the stiffness

of the non-linear spring model (using Plexiglas elastic constants), calculated at the packing overlap in the monodisperse case, here $\overline{\delta}/a_0 \approx 10^{-3}$. At this overlap, the stiffness and the contact duration of a particle-particle collision appear to be of the same order for both linear and non-linear model.

5.1.3 Results

In the following, the stress-time response to the initial perturbation is recorded at each layer with a large binning rate, $\Delta t = 10^{-6}\,\mathrm{s}$, in a time-window of $T = 0.0015\,\mathrm{s}$, to be further analyzed for all systems described above in section 5.1.2. Note that even though the boundary conditions and the excitation method both influence the stress-time signal shape (data not shown), we only use the velocity-pulse method in this study for convenience; a detailed study of different pulse methods will be published elsewhere.

Linear model

From order to weak disorder:

The stress-response – ten layers from the source – is plotted against time in Fig. 5.2 (Left) for the monodisperse and the polydisperse situation with $(\Delta a) = 2\overline{\delta}$ (for more details see Refs. [77, 79, 80]). Only these two last cases will be shown in this study, since the case $(\Delta a) = \overline{\delta}/2$ resembles the monodisperse system, and the case $(\Delta a) = \overline{\delta}$ behaves similar to the case $(\Delta a) = 2\overline{\delta}$. Qualitatively, signals arrives later in the polydisperse system, which is consistent with a lower propagation speed (see Ref. [80]) due to the smaller coordination number, as compared to the monodisperse system. The signal amplitude is smaller in the polydisperse system, which indicates that some energy has been transferred (scattered) to other types of motion (waves of different nature, like shear waves, and/or with different propagation direction). Finally, the coda of the signal in the polydisperse packing is clearly irregular, while it is periodic in the monodisperse case.

In order to analyze the two signals in more detail, the frequency content is examined from the Fourier power spectrum in time, see Fig. 5.2 (Right). The monodisperse system shows a smooth spectrum, while in the polydisperse system, due to the disorder present at the contact level, some frequencies seem to be filtered stronger than others, i.e., the spectrum shows peaks and valleys.

In order to understand the propagation properties of the wave-components with different frequencies, the frequency power spectra are plotted (vertical) against the position in z-direction (horizontal) in Fig. 5.3 in grey-scale.

In the monodisperse case (Left), frequencies above about 49 kHz are immediately attenuated, since the packing cannot transmit frequencies higher than the

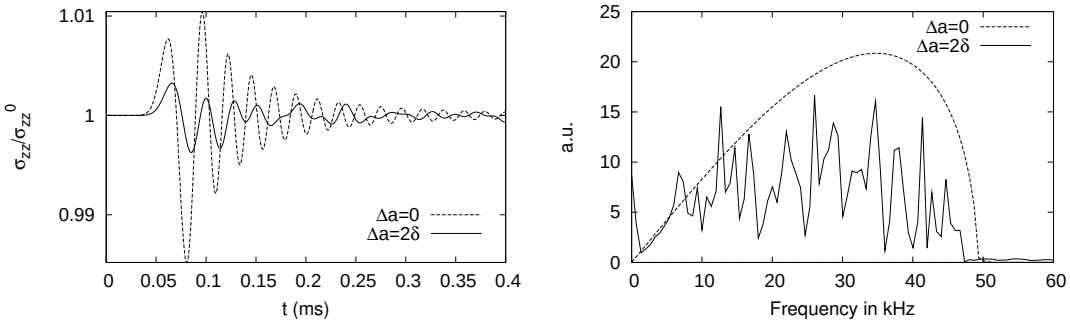

Figure 5.2: (Left) Normal stress (σ_{zz}) scaled by the equilibrium stress (σ^0_{zz}) as function of time at a distance of 10 layers from the source for the monodisperse (dashed line) and a polydisperse (solid line) system. (Right) Fourier power spectrum of the two stress-time signals from the left figure.

(largest) eigen-frequency of a single layer. From the third layer on, the range of frequencies present in the time signal is conserved during the propagation. Note that the bending observed, beginning at about 50 layers from the source, is only due to the limited time window of the collected data, i.e., for larger time windows, the bending starts later. This bending, top right, is consistent with a smaller propagation speed of higher frequency wave components.

In the polydisperse case (Right), the power spectrum shows a strongly reduced range of transmitted frequencies as the wave propagates away from the source. Frequency transmission over large distances is observed under about 8 kHz and the higher frequencies (about $8 - 46$ kHz), present near the source, decay exponentially (data not shown) between layers 20-40. Note that some special frequencies propagate deeper into the system than others, as the band around 35 kHz (eigen-frequency of a double layer) for example.

In order to understand possible relations between frequencies and wave-numbers, the two-dimensional Fourier transform in time and space is calculated from the same data as before. The dispersion relation in the monodisperse packing (angular frequency $\omega = 2\pi f$ versus angular wave-number $\overline{k} = 2\pi k = 2\pi/\lambda$) has a perfect sine-shape $\omega(\overline{k}) = \omega_0 \sin(l_z\overline{k}/2)$, with layer-width in z-direction, $l_z = \sqrt{2}a_0$, and P-wave speed, $V_P = \omega_0(l_z/2) \approx 219$ m/s, where $\omega_0 = 2\pi f_0$, with $f_0 \approx 49$ kHz, see Fig. 5.4 and Refs. [79, 80]. The minimal wave-length can be obtained from the maximum of the dispersion relation, $l_z\overline{k}_{\max}/2 = (\pi l_z)/\lambda_{\min} = \pi/2$, so that $\lambda_{\min} = 2l_z$.

For the polydisperse packing, with $(\Delta a) = 2\overline{\delta}$, the dispersion relation has generally smaller intensity, is smeared out much broader, and is more noisy, even though the sine-shape is still visible. Some band gaps appear, and one of them

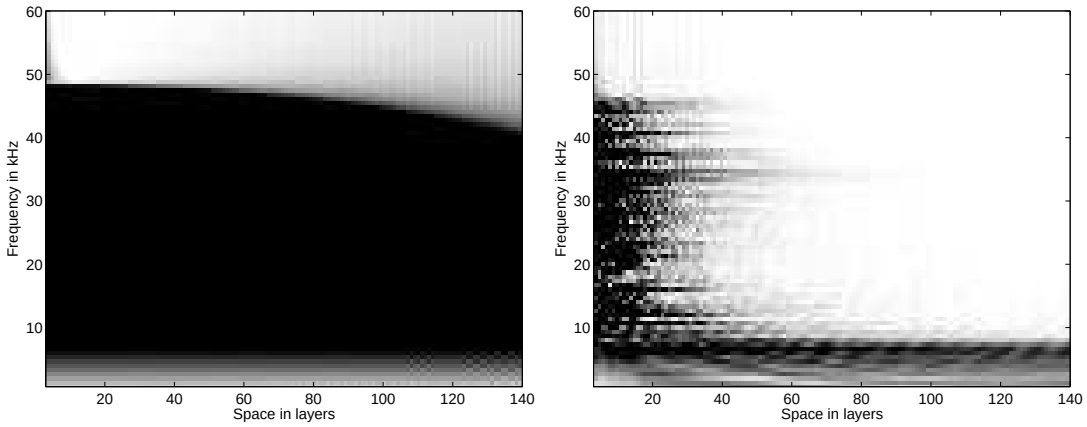

Figure 5.3: Frequency-space diagram (darkness corresponds to the amplitude, absolute value, of the Fourier coefficients, black is large and white is small) for a P-wave propagating in z-direction in the monodisperse (Left) and the polydisperse (Right) packing from Fig. 5.2.

indicates the definite end of the linear behavior (with a corresponding wave speed $V_P \approx 174\,\mathrm{m/s}$) in the "low frequency/large wavelength" regime, somewhat smaller than for the monodisperse packing.

In order to analyze this peculiar dispersion relation, the mean wave-number corresponding to a certain frequency, weighted only above a suited cut-off (here six times the average value of all Fourier-coefficients), is plotted on top of the dispersion relation as white dots in Fig. 5.4 (Right). The dots underline the linear regime, corresponding to the transmission-band at small frequencies, and also indicate the band-gaps in the cases where all Fourier coefficients corresponding to one frequency are smaller than the cut-off value. In the frequency range from $2 - 8\,\mathrm{kHz}$ the dots are nicely linear, with a slope $V_P \approx 174\,\mathrm{m/s}$. At higher frequencies, the dots (mean wave-numbers) are no longer falling on a straight line and band gaps as well as transmission bands appear. The clear band gap observed between $18 - 21\,\mathrm{kHz}$ is also visible in Fig. 5.3 in so far that these frequencies penetrate least into the system.

System size:

In order to study the influence of the system size on the wave propagation, simulations have been performed in systems with a four times larger area in the x-y-plane. The z-system size determines the smallest wave-number (largest wavelength) present in the system: $k_{\mathrm{min-z}} = 1/\lambda_{\mathrm{max}} \approx 1.77\ \mathrm{m}^{-1}$ with $\lambda_{\mathrm{max}} = 2L_z$, where L_z is the length of the system. The x-y-system-size ($L_x = L_y = 8a_0$ or $16a_0$) corresponds to the wave-numbers $k_{\mathrm{min-x}} = 1/(2L_x) \approx 62.5\,\mathrm{m}^{-1}$ and $\approx 31.25\,\mathrm{m}^{-1}$ for the small and large systems, respectively. If the x-y system size has an

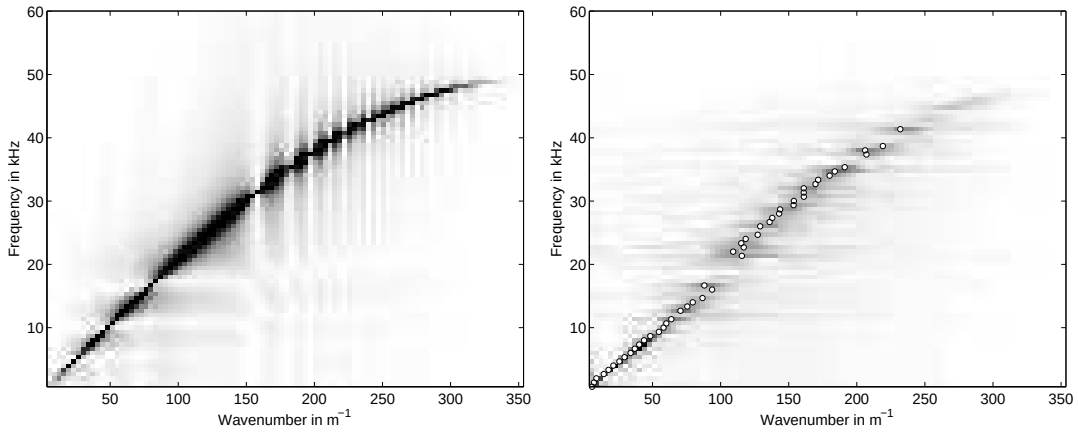

Figure 5.4: Dispersion relation (darkness corresponds to the amplitude, absolute value, of the Fourier coefficients, black is large and white is small) for the same data as in Fig. 5.3, for the (Left) monodisperse, and the (Right) polydisperse cases. The amplitude of the left sine is 49 kHz, while the slope for small frequencies and large wave-lengths, is $V_P \approx 219\,\mathrm{m/s}$. The white dots in the right figure indicate the cut-off-weighted averaged wave-number per frequency, and their slope from 2-8kHz is $V_P \approx 174\,\mathrm{m/s}$.

effect, one should expect special features at these wave-numbers, or the shift of features to smaller wave-numbers when the system size is increased. However, the results obtained with the larger system are much similar to those obtained with the smaller system, see Fig. 5.5. The band of transmitted frequencies is about the same, up to 8 kHz, and also the band-gap around 18 kHz is obtained independent of the system-size. Most differences are observed in the higher frequency range, where the signal is more noisy anyway. Due to the better statistics, the plots look smoother and less noisy for the larger system. In conclusion, changing the system size by a factor of two should reveal finite size effects of the dispersion relation: transmission bands and band-gaps should be found at different wave-numbers, however, the size of the system perpendicular to the P-wave propagation direction has no visible effect.

P- and S-waves:

The propagation of a S-wave in the (classical) monodisperse system was discussed in Ref. [79]. The ratio of P- to S-wave speeds was found to be $V_{Pz}/V_{Sz} \approx \sqrt{2}$ – as expected from wave mechanics in crystals. The frequency range of possible S-waves ends at about 35 kHz (eigen-frequency of a single particle in the x-direction) and, for a given wave-number, the corresponding frequency is higher for the P-wave than for the S-wave (data not shown).

The propagation of a S-wave in the polydisperse system, with $(\Delta a) = 2\overline{\delta}$, leads to the same dispersion behavior as observed for the P-wave. The band of

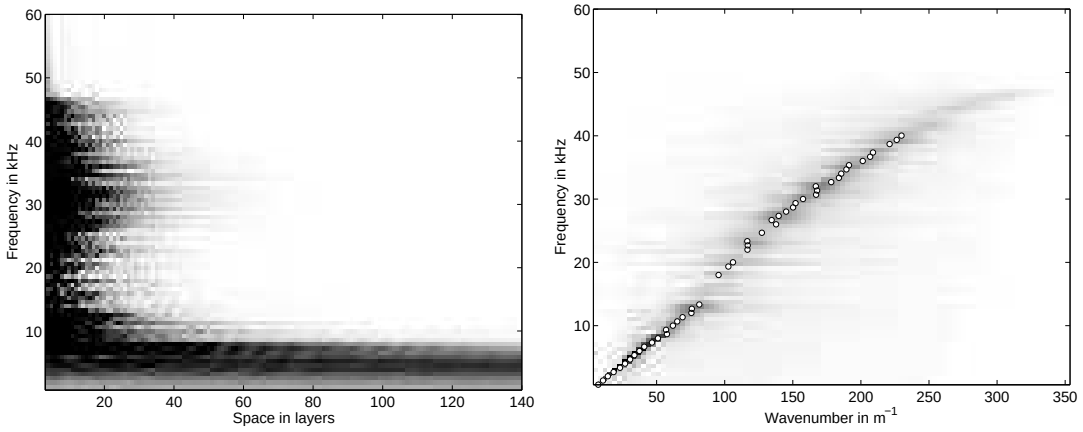

Figure 5.5: Frequency-space diagram (Left) and dispersion relation (Right), (darkness corresponds to the amplitude, as in Figs. 5.3 and 5.4) of a P-wave for the polydisperse packing $(\Delta a) = 2\overline{\delta}$ with a larger section area of 8×8 particles. The slope of the dispersion relation leads to $V_P \approx 174\,\mathrm{m/s}$ in agreement with the smaller system from Fig. 5.4.

transmitted frequencies is also below 8 kHz and the higher frequencies are limited by 35 kHz, like in the monodisperse case. More explicitly, the wave speeds are $V_S \approx 125\,\mathrm{m/s}$ and $V_P \approx 175$ m/s for S- and P-waves, respectively, which is consistent with $V_P/V_S \approx \sqrt{2}$; thus no surprises are evidenced for S-waves in slightly polydisperse systems.

Finally, mode conversion was observed in the simulations, where S- to P-wave conversion appeared to be stronger than the P- to S-wave conversion. Since wave conversion contributes to the attenuation behavior (especially of the S-wave), a future more detailed study is needed to analyze this issue further, including a possible frequency-dependence.

Frictional packing

When the particle contacts are frictional, i.e., a tangential spring, $k_t = 0.2k$, with Coulomb friction criterion, $\mu = 0.5$, is added, see section 5.1.2 and Ref. [71], the overall frequency spectrum extends to higher frequencies, around 54 kHz, as a consequence of the tangential spring at the contact, which induces a higher particle (or layer) "eigenfrequency". However, the higher frequencies of the wave vanish earlier than in the frictionless case (between layers 15-25), while the remaining low frequency band is broader and extends until about 12 kHz, see Fig. 5.6 (Left). The linear regime of the dispersion relation corresponds to a wave speed of $V_P \approx 200\,\mathrm{m/s}$, i.e., somewhat slower than in the monodisperse case.

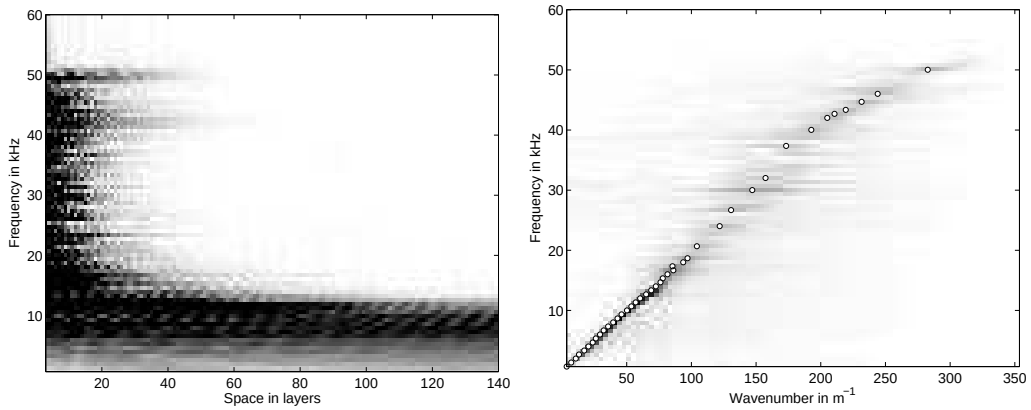

Figure 5.6: Frequency-space diagram (Left) and dispersion relation (Right), (grey-scale and symbols as in Fig. 5.5), for a P-wave in the polydisperse packing $(\Delta a) = 2\overline{\delta}$ with friction.

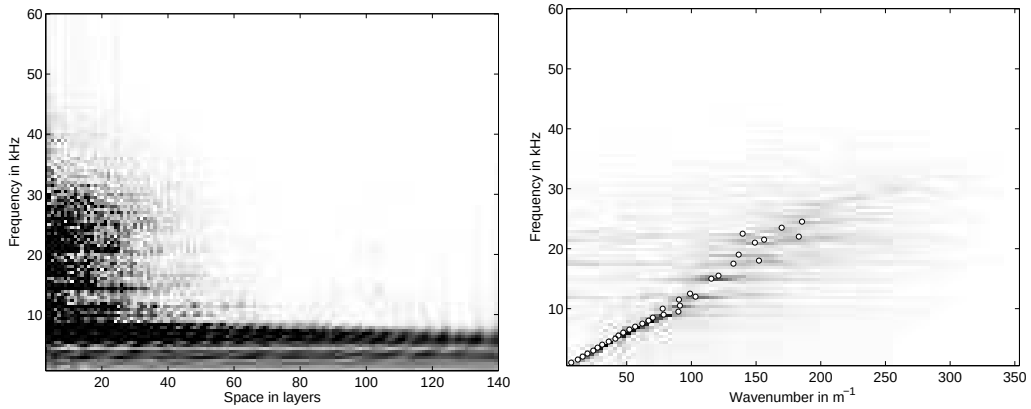

Figure 5.7: Frequency-space diagram (Left) and dispersion relation (Right), (grey scale and symbols as in Fig. 5.5) of a shear wave for the polydisperse packing with $(\Delta a) = 2\overline{\delta}$.

The presence of friction, see Fig. 5.6, seems to extend or stabilize the linear dispersion regime for P-waves. The non-linear, non-propagating regime with friction, is characterized by a relatively weaker signal. This might be due to the fact that in addition to the geometrical dispersion, which is also present in the frictionless case, friction enhances the compressive- to shear-mode conversion and also activates rotational modes to which part of the energy is lost. For shear waves in the monodisperse packing, in Ref. [79], an additional branch (rotational modes) in the dispersion relation was found (data not shown here), however, for the polydisperse packing $(\Delta a) = 2\overline{\delta}$ this could not be confirmed – thus remaining an issue for future studies.

The Hertz contact model

As is reported in Refs. [92, 93], the choice of the contact model has an influence on the frequency-dependent response of the system. Therefore, a simulation with another packing, prepared with the Hertz contact model, is performed. Qualitatively, the same wave propagation characteristics is observed as for the linear model. However, as a consequence of a different initial state and due to the different nature (non-linear) of the contact model, the results obtained are quantitatively different. Due to a somewhat lower coordination number, $C \approx 9.77$, and thus some decreased packing stiffness in the z-direction, the wave travels a little slower, both for the P-wave, $V_P \approx 156\,\mathrm{m/s}$, see Fig. 5.8, and for the S-wave $V_S \approx 106\,\mathrm{m/s}$ (data not shown). Whether the ratio, $V_P/V_S \geq \sqrt{2}$, has a meaning, cannot be evidenced from our data. A more detailed study of the shape of the wave-front and coda, e.g., under different stress conditions is far beyond the scope of this study.

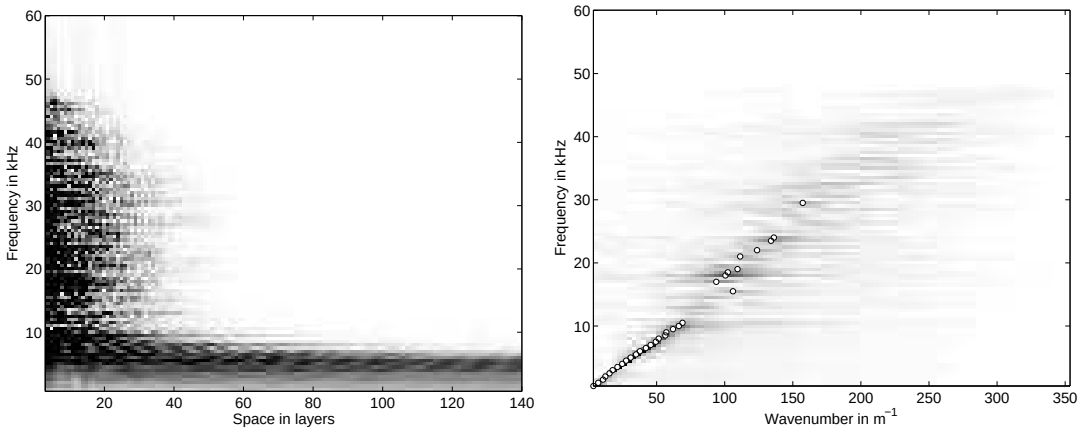

Figure 5.8: Frequency-space diagram and dispersion relation (grey-scale and symbols as in Fig. 5.5), for a polydisperse packing with $(\Delta a) = 2\overline{\delta}$ and the Hertz contact model.

Discussion of non-linearity and disorder

The attenuation of frequencies, when the wave is propagating in a slightly polydisperse system, is a consequence of the change of the geometry and the corresponding material properties. The polydisperse systems are characterized by two main features: (i) a local (contact level) geometrical disorder, and (ii) the presence of clapping contacts, opening and closing while a wave is passing by.
This strong non-linearity at the contact level is specific to granular materials. It has, according to Ref. [119,120], its signature in the frequency content of the wave,

closing contacts can generate high frequency signals, but opening contacts also interfere. In order to study the influence of the clapping contacts on the wave-propagation, in parallel to the polydisperse simulation from Figs. 5.3 (Right) and 5.4 (Right), two additional simulations have been performed. Everything was identical, only a 10 and 100 times smaller initial velocity v_z was used, leading to fewer clapping contacts. In the case of the smallest velocity, only two contacts are clapping in the whole system, while for the largest velocity it is about 20 contacts (0.1%).
The analysis of the frequency-space diagrams of these simulations shows no qualitative difference for the dispersion, as compared to the previous simulations. The smaller v_z, the larger are (relatively) the lowest frequency and lowest wave-number Fourier coefficients, so that the cut-off averaging is applied in the range $f > 3\,\mathrm{kHz}$ and $k > 12\,\mathrm{m}^{-1}$ only. The corresponding cut-offs used are proportional to the velocity amplitude and lead to cut-off weighted wave-numbers per frequency that are slightly decreasing with the initial velocity. However, this effect is very weak (comparable to the spacing between the data) and the dispersion curve (dots) always remains below the envelope of the monodisperse case. Thus, even though clapping contacts contribute to the non-linear response of the system, they do not play a key role in the observed attenuation of the higher frequency bands, given the present conditions (small amplitude $u_{max}/\overline{\delta} \approx 5\,10^{-2}$ with only 0.1% of clapping contacts).
Having reduced the non-linearity due to clapping contacts by using smaller amplitudes and also having used linear as well as non-linear contact laws, the conclusion is that the geometrical disorder at the contact level is responsible for the attenuation of the higher frequencies of waves in weakly polydisperse packings. Since more strongly disordered (polydisperse or not) packings would imply this same local (contact level) geometrical disorder, similar results are expected for such, more realistic, packings – as to be studied in future.

5.1.4 Summary and Conclusions

Wave propagation was examined in three-dimensional ordered (crystal) packings with monodisperse, and with slightly polydisperse packings of spheres. The latter involve contact level geometrical disorder, but are still close to a crystal structure. Compressive (P) and shear (S) waves were examined with and without friction; the system size and the initial agitation amplitude were varied and a non-linear Hertz type contact law was applied.
In all disordered cases (with size variation comparable to or larger than the typical contact deformation), a low frequency band transmits waves well, while most higher frequencies are attenuated or scattered within several tens of layers.

Disorder (fewer contacts) leads to a reduced propagation speed of the wave, whereas friction (due to tangential elasticity) leads to an increased wave speed – and also to a broader transmission band. Also, the confining pressure, directly related to the static deformation of the contacts, should have an influence on the results. This will be analyzed in a future study.

Having started with monodisperse situations and slowly increasing polydispersity, the natural next step is to confirm these observations also in the case of full disorder and wider size-distributions. The interesting transmission behavior in such more realistic granular packings can then be studied concerning friction, cohesion and rotational degrees of freedom.

Acknowledgements

This work is part of the research program of the "Stichting voor Fundamenteel Onderzoek der Materie" (FOM), financially supported by the "Nederlandse Organisatie voor Wetenschappelijk Onderzoek" (NWO) and the Stichting Shell Research.

5.2 Mode conversion in the presence of disorder

A novel multi-scale theory for non-linear wave propagation in inhomogeneous systems is presented. Wave-mode conversion, or wavenumber evolution, is studied in a weakly polydisperse granular bar using DEM (Discrete Element Method) simulations. Different single (or double) discrete wavenumbers are "inserted" as standing wave initial condition in the granular packing and the system is then free to evolve. For large wavelengths (small wavenumber), the original standing wave remains, oscillating in time. For shorter wavelengths the original wave disappears as it is converted to other wavelength modes. The insight on this wavenumber (wavelength) evolution, i.e., the non-linear transfer of energies from the agitated wavenumber to all others, will lead to a novel theoretical model based on a Master-equation in wavenumber-space.
This non-linear energy transfer is mainly due to the inhomogeneous nature of the particulate material, in this case the contact disorder in the weakly polydisperse packing. Indeed the effect of large amplitude non-linearities, like the opening of contacts, is reduced by using very small amplitudes in the simulations. Additional non-linearities, like the cross-talk between two waves with different wavenumbers, are another issue to be examined.

5.2.1 Introduction

In the field, usually, only low frequency modes are observable and open questions concern the non-linear nature of wave-propagation in general, and the mechanisms of momentum- and energy-transfer in particular. In a linear medium, at small wave-amplitude, the spectral components of a wave would propagate independently from each other. Dispersion occurs due to the faster propagation of lower frequencies and larger wavelengths. Small inhomogeneities and the particulate nature of the medium mostly affect the short wavelengths, while the large wavelengths propagate across a quasi-homogeneous medium. Effects like attenuation and scattering also influence the characteristics of the measured signals. However, even for small amplitudes, the classical theories are not able to explain the non-linear wave propagation in real materials.

Why low frequency components are stronger in signals observed in granular materials is still an open question: There is an ongoing discussion whether the low frequency component of the signal is linear (ballistic/coherent propagation), according to Jia et al. [49], or if it is due to a non-linear effect of self-demodulation, according to Tournat et al. [118] where the interaction between higher frequencies (those sent in), lead to a low frequency component as the result of the difference

of two high frequencies (see Ref. [118] for more details). The coda, corresponding to the high frequency part of the signal, arriving after the main pulse, is non-coherent (due to scattering) and only recordable at short distance from the source and under relatively high pressure. One possible reason for the difference in the above interpretations is that in some experiments [49], low frequencies are already present at the source and hence behave linearly as their wavelengths are large enough to "see" the sample as a homogeneous medium. The second interpretation deals with nonlinear effects and frequency- (wave-mode-) mixing: These are also observed in the field: Shell has recently performed exploratory studies in which the nonlinear mode originating from wave mixing of two sources, with different frequency and location, were found to propagate anomalously far.

Inspired by previous numerical results on the dispersive behavior of the wave propagation in weak polydisperse granular packings, see section 5.1.3, the purpose of this study is to understand how each single wavelength or wavenumber evolves in time and explore the wavenumber space. In other words, how energy is transfered between different frequency- (or wavenumber) bands.

In the following, an adapted Master equation theory will be presented first. Then, the granular packing and the simulation procedure will be described. The results for a single or "mono-chromatic" wavenumber insertion are analyzed and discussed in detail. A simulation with a "bi-chromatic" wavenumber insertion, leading to non-linear cross-talks between the bands, is also studied. Finally, the eigen-mode analysis of the packing will be discussed with respect to the dispersion effects observed in the simulations.

5.2.2 Theory

The linear Master Equation, derived from the framework of population balance, is adapted for sound propagation without considering position or propagation-speed, only assuming an energy probability distribution. The quantity $q(k_i) = e(f_i)/E$, with $E = \sum_{i=1}^{B} q(k_i)$, describes the probability that the band i with wavenumbers around k_i contains a fraction of energy $q(k_i)$ of the total energy, E. The time evolution of the energy spectrum, divided in $i = 1, ..., B$ bands, is described by:

$$\frac{d}{d\tau} q(k_i) = -b^i q(k_i) + \sum_{j \neq i} b^i_j q(k_j) \quad \text{with} \quad b^i = \sum_{j \geq 1} b^i_j \tag{5.2}$$

where the rate b^i_j quantifies how much energy from band (j), during time interval $d\tau$, is dispersed/attenuated/transferred into band i. This implies that energy is distributed from one band (i) to the other bands, independently of the energy in the other bands, i.e., a simplifying assumption which has to be tested. Note that

τ is not time, but equivalent to time with $\tau = t^2$, as it will be discussed below. In experimental practice, it is impossible to find the rates b_j^i , however, using discrete particle simulations, as described below, one can directly measure the rates using the following procedure: Agitate the system by a single wave with wavelength λ and examine, e.g., the wavenumber spectrum evolution after short time intervals. The change of the spectrum allows for the determination of the rates b_j^i and to test and, if necessary, improve the assumptions made.

In a more general framework, it is possible to generalize the approach to a non-linear Master Equation with terms of the form

$$\frac{d}{d\tau}(k_m) = \sum_{j,k} a_m^{i,j} q(k_i) q(k_j) \pm ... \tag{5.3}$$

with the rates $a_m^{i,j}$ at which energy from bands i and j interact constructively and feed energy into band k, during time $d\tau$. Note that the product of q makes the terms non-linear, because energy from both bands has to be present, in order to allow for the constructive interference. An implicit assumption for this first-order non-linearity is the "pair-wise" interference - which has to be tested by future simulations.

Furthermore, the master equation also can contain energy-dissipation and -source terms, as well as different additional energy densities for standing waves, propagating waves, and scattering (change of direction). However, this is beyond the scope of this study. Before we can discuss the Master equation and its solution, we first present the simulation results.

5.2.3 Simulations

Particle packing

The geometrical starting configuration considered in this study is a dense, static packing of grains, with radii a_0 (=0.001m), arranged in a Face Centered Cubic (FCC) structure (with volume fraction of $\nu \approx 0.74$), where square layers in the x-y-plane (4×4 particles) are stacked in the z-direction ($L = 200$ layers), see Fig. 5.9 for a snapshot of a part of the system. Note that periodic boundary conditions are chosen in order to avoid wall effects. Based on the regular packing, weak polydisperse packings are obtained by randomly changing the particle sizes according to a narrow size distribution, which is homogeneous, centered at a_0, and has a width $2(\Delta a)$ of the order of the mean overlap $\overline{\delta} \sim \Delta a$. Then the system is allowed to relax to a new, slightly disordered equilibrium configuration with the same volume but with a significantly lower coordination number $C \sim 9.8$. More detailed information about these packings is given in section 5.1.2.

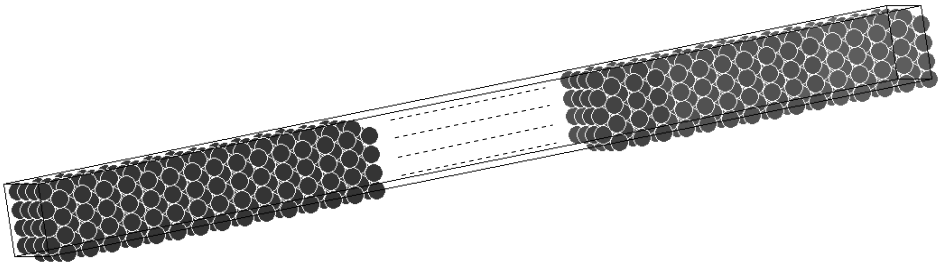

Figure 5.9: FCC-structured packing, thin 4×4 in the x- and y-directions, and elongated in the z-direction (200 particles).

Wave mode agitation

Standing plane waves in z-direction with different wavenumbers $k = L/\lambda = 1$, 2, 4, 5, 8, 10, 15, 20, 25, 33, 40, 50, 60, 75 and 100 are agitated, with $L = 200$ layers the system length and λ the wavelength. For this an initial velocity v_z with a sinusoidal profile, $v_z \sin((2\pi z_{layer})/\lambda)$, with z_{layer} the layer position in the z-direction is given to the particles in the system as shown in Fig. 5.10.
For the analysis of the data it is important to avoid or reduce any "numerical" noise. Therefore, the amplitude of the velocity for the particles must be chosen carefully, even though the disorder present is rather small. The maxima and minima of the sine are chosen to fall exactly on the center of a layer. Moreover the particle velocity is assigned according to the average position of a layer and not to the single particle positions, as this leads to cleaner signals. Since the positions of the particles in a pseudo-layer are only slightly dispersed, the overall wavelength shape is well conserved.

Results

In both regular and polydisperse packings, several simulations have been performed for different wavenumbers $k = L/\lambda$, where the system length $L = 200$ layers and λ the wavelength.

The time evolution of the space signals, in this case the average velocity of the $(x - y)$ layers, is analyzed by considering their Fourier transform (wavenumber space). Hence the wavenumber content evolution of an "inserted" "monochromatic" wavenumber can be followed in time.
For the regular packing nothing astonishing is observed as the modes (wavenumbers) stay stable in time (data not shown here). In fact, a standing wave has been created. Due to the regular structure of the packing and the absence of attenuation, the initial wave form is conserved. It shows a nice and regular "breathing" of

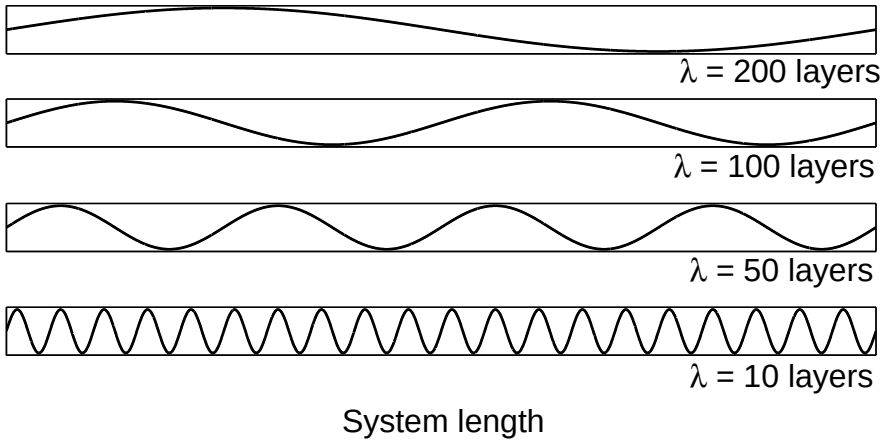

Figure 5.10: Schematic of the inserted wavelengths in the system for $k = L/\lambda = 1, 2, 4$ and 20 with corresponding wavelengths of $\lambda = 200, 100, 50$ and 10 layers, respectively, and system length $L = 200$ layers.

the wave form in time with the frequency corresponding to this wavenumber, according to the dispersion relation in Sec. 4.1.3. These results are consistent with the good propagation characteristics for all frequencies, as reported in section 5.1.3.

In the case of a slightly polydisperse system more interesting results are observed. In figure 5.11 the wavelength (or its corresponding wavenumber) spectrum is plotted against time. For large wavelengths, $\lambda \geq 40$ layers, the inserted wave form is more or less conserved in time. This is visible by the clean black line over the whole time window while the rest of the spectrum remains almost white. For $\lambda = 20$, the line resembling the input wavenumber remains sharp, but more energy is transferred to the other modes. In contrast, for smaller wavelengths, as for example $\lambda \sim$13.34, 8, and $\sim$6.06 layers, two main features are observed. First, the energy from the inserted wavenumber is transformed rapidly into adjacent bands. The shorter the wavelength the faster this occurs. Second, the energy of these adjacent bands is then rapidly transferred to the small wavenumber bands $\lambda \geq 40$. The inserted wavelength $\lambda = 2$ is a remarkable case as the above described energy transfer is occurring somewhat later.

From those observations it is clear that probing the weakly disordered packing with different wavelengths in a quasi-standing-wave procedure reveals the dispersive nature of such a material. We consider the contact disorder to be the main cause for the dispersive behavior, since it is by far the most significant source of dispersion and attenuation in this system, see section 5.1.2.

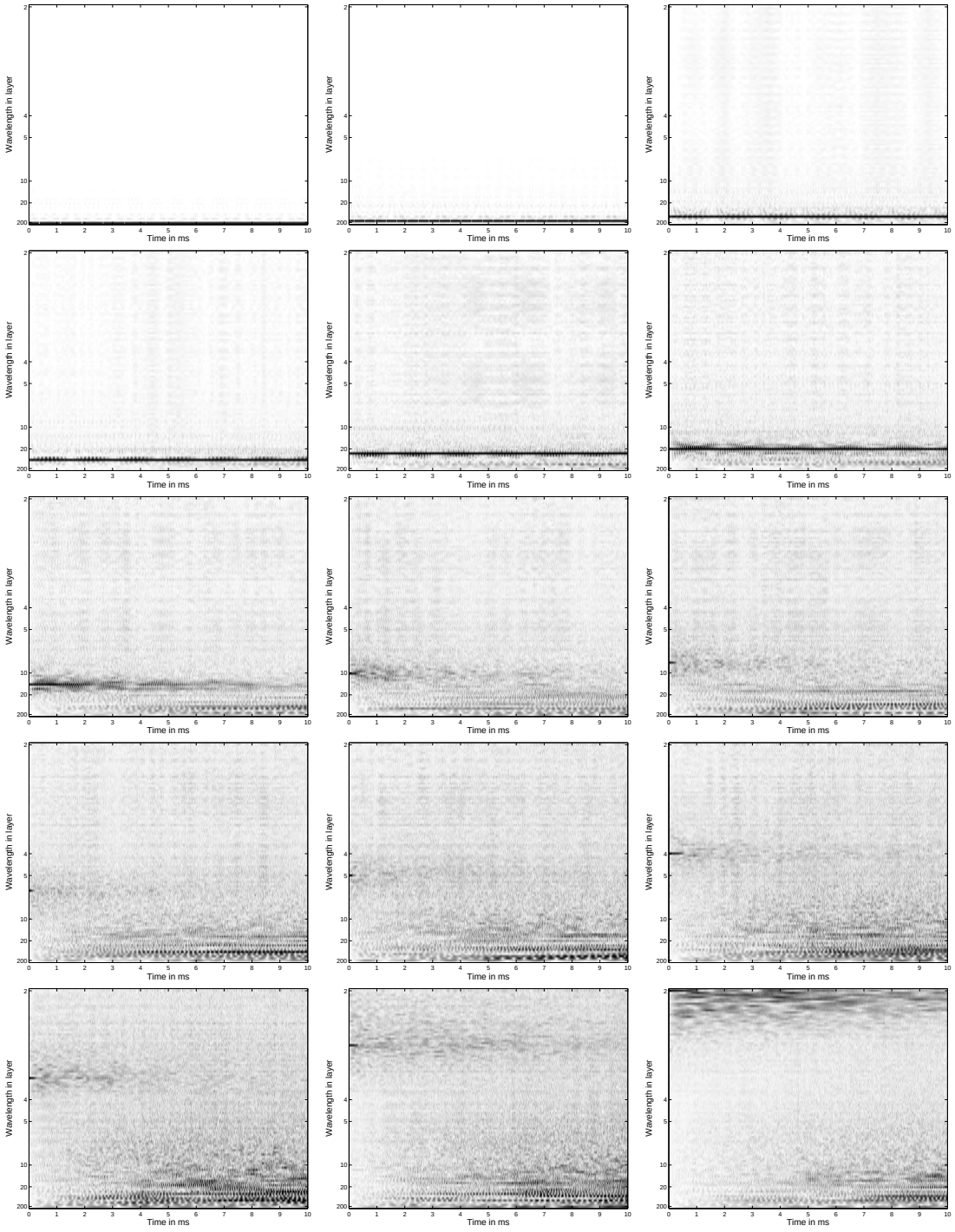

Figure 5.11: Wavelength (vertical, in units of layers) as function of time (horizontal, in units of ms). The inserted "mono-chromatic" wavelengths $\lambda = L/k = 200$, 100, 50, 40, 25, 20, $\sim$13.34, 10, 8, $\sim$6.06, 5, 4, $\sim$3.34, $\sim$2.67 and 2 layers, from top-left to bottom-right. White, gray, and black correspond to low, medium and high intensity (absolute value of the Fourier components).

The simulations were performed at rather small amplitudes, so that amplitude-related non-linear effects should not play a too important role in these observations. However the occurrence of opening and closing contacts is not excluded completely here. Neither the amplitude nor the randomness and material parameter dependence has been studied in detail yet.

The observed decay of the intensity for the inserted wavenumber can be extracted from these data and provides the input-parameters, b^i, for the theoretical model. The other input-parameters, b^i_j, are provided by the increase of the intensity for the other, initially not inserted wavelengths. This will be described in the next section after a short look at the dispersion relation.
Applying a second time a Fourier transform to the data shown in Fig. 5.12, leads to a frequency-wavenumber relation. In Fig. 5.12, left graph, the dispersion for a single inserted wavenumber, $k_i = 10$ ($\lambda = 20$ layers) is shown. It is also possible to extract the "full" dispersion relation from these data, by applying the Fourier transform to all the inserted k simulations and subsequent superposition. Fig. 5.12, right graph, reproduces nicely the same dispersion relation obtained previously by a single dynamical pulse propagation simulation in the same system, see section 5.1.3.

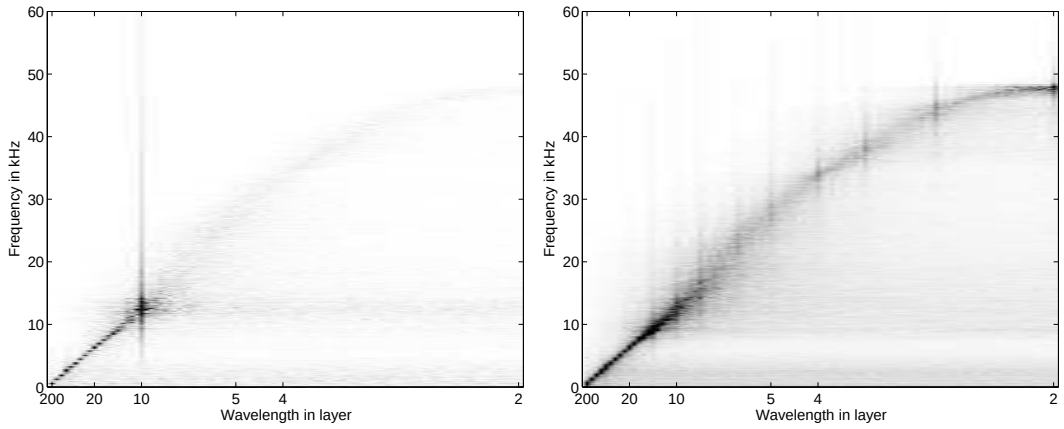

Figure 5.12: (Left) The Fourier transform in time of the data shown in Fig. 5.11, for the inserted "mono-chromatic" wavelength $\lambda = 10$ layers, with the frequency (vertical, in kHz) as function of wavelength (horizontal, in layers). White, gray, and black correspond to low, medium and high intensity (absolute value of the Fourier components). (Right) Superposition of the Fourier transform in time of all the data shown in Fig. 5.11.

Energy transfer rates

The theoretical approach described in section 5.2.2, the Master Equation, requires transfer rates for all wavenumbers for each inserted wavelength. This matrix of transfer rates can be determined from the simulations. The first step is to examine the signals in the wavenumber-time space by applying a Fourier transform to the space-time signals obtained from the simulations.

Several signal amplitudes have been examined. The average potential energy, the average displacement, and the average velocity per layer. For unknown reasons, only the latter gives the most suitable results for the following analysis, as the peak for the inserted wavenumber in the wavenumber space is the highest relative to the initial noise ratio, and thus well detached from the other wavenumbers. Also, the first term of the Fourier transform, the integral of the signal over space, is lowest with respect to the signal integral over space and thus gives unperturbed amplitudes for the low wavenumbers. Those choices lead in the following to data that are nicer to fit, and that give the most objective parameters.

In the following, for each inserted wavenumber, the Fourier transform is applied to the average velocity per layer $v_z(z,t)$. The obtained spectra are expressed in terms of wavenumbers, $A^i(k)$, with A the amplitude of the Fourier transform, $k = 1, 2, ..., 100$ the wavenumber and i =1, 2, 4, 5, 8, 10, 15, 20, 25, 33, 40, 50, 60, 75 and 100, the indices over the inserted wavenumbers. The wavenumber amplitudes can be separated in two categories:
(1) the "diagonal" elements, the $A^i(k_i) := A^i(k = i) = A^i_i$, which correspond to the decreasing wave-modes, giving energy to the other modes.
(2) the other elements, the $A^i(k_j) := A^i(k = j) = A^i_j$ for $j \neq i$, which correspond to the wave-modes that are increasing, getting energy from the inserted mode k_i. This description is only true for very early times when the interactions between the modes are still negligible.

Figure 5.13 (left) shows the Fourier transform of the space signal for the inserted wavenumber $k_i = 15$ at three different times, $t_1 = 0$, $t_2 = 1$ and $t_3 = 40$ timesteps (with $dt = 2.10^{-7}$s), $A^{15}(k)$. A large peak amplitude is visible for the inserted wavenumber $k_i = 15$, and very small amplitudes for the other wavenumbers. However, those are increasing by orders of magnitude within a few simulation timesteps. Furthermore, the wave-form in the system is clearly "breathing", as described earlier. Fig. 5.13 (right) shows the time evolution of the spectral amplitude for the wavenumber $k = 15$, $A^{15}(k = 15, t)$. As the kinetic energy transforms to potential energy and vice-versa (and so on) with a frequency corresponding to the inserted wavenumber ($k = 15$ in the figure), the time evolution shows an oscillating behavior with a frequency of $\sim$10 kHz. Therefore, in order to eliminate of the "breathing", the time evolution of the spectral amplitudes,

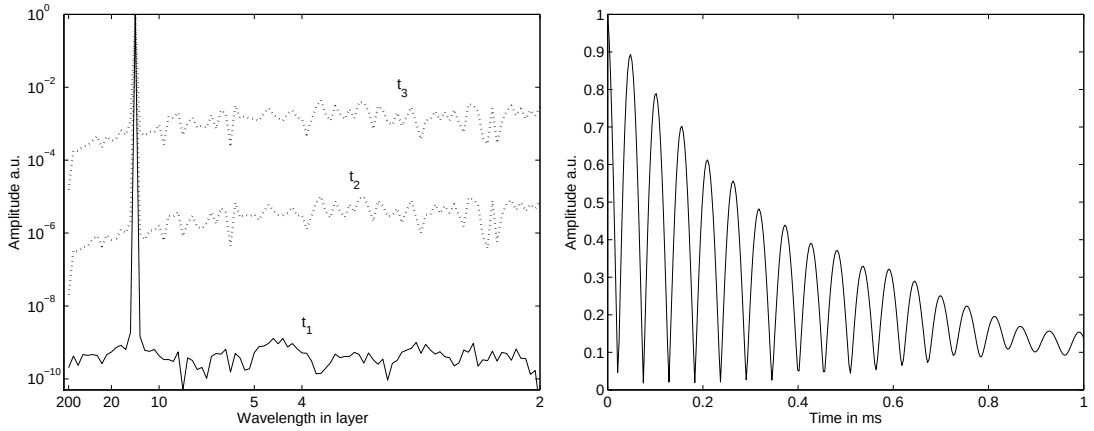

Figure 5.13: (Left) The power spectrum, wavenumber-space, of the average velocity signal for the the inserted "mono-chromatic" wavenumber $k_i = 15$, or wavelength $\lambda = L/k \sim 13.34$ layers, at very short times $t_1 = 0$, $t_2 = 1$ and $t_3 = 40$ time-steps with $dt = 2.10^{-7}$, $(A^{15}(k))$. (Right) The long time evolution of the wavenumber amplitude, $A^{15}(k_{15})$, displays the "breathing".

$A^i(k = j, t)$, needs to be scaled by the total amount of "power" related to the total particle velocity present in the spectrum. The quantity realizing this is the sum of the amplitudes of the spectrum, $\sum_{j=1}^{B} A^i(k_j, t)$. This gives the time evolution of the scaled spectral amplitudes:

$$\tilde{A}^i(k,t) = \frac{A^i(k,t)}{\sum_{j=1}^{B} A^i(k_j,t)}. \tag{5.4}$$

Now, in order to extract the desired rates for the Master equation, the $\tilde{A}^i(k_{j\neq i}, t)$ are fitted by a power law, $b^i_j\, t^2 = b^i_j\, \tau$. The power 2 seems to be consistent over all the data and has been fixed in order to keep the fitting-approach most simple in a first step. The b^i_j quantify the energy transferred from mode i to mode $j \neq i$. In the case of the inserted and thus decreasing modes (for $i = j$), the fitted rate b^i, comes from $\tilde{A}^i(k_i, t) = 1 - b^i\, t^2 = 1 - b^i\, \tau$. If not mentioned explicitly, the fits are performed for the first 50 times-steps only, with $dt = 2.10^{-7}$s.

For the complete picture the unscaled b^i, thus also including the early "breathing" effects are plotted as well. Figure 5.14 (top-left), shows the unscaled b^i as function of wavelength λ. A non-linear increase of the rates for increasing wavenumbers k^i is observed as could be expected from Fig. 5.11. Small wavenumbers transfer little energy to other modes and "breath" quite slowly. With increasing wavenumber the transfer to other modes becomes stronger and the decrease due to breathing becomes stronger, simultaneously leading to non-linear $b^i(k_i)$.

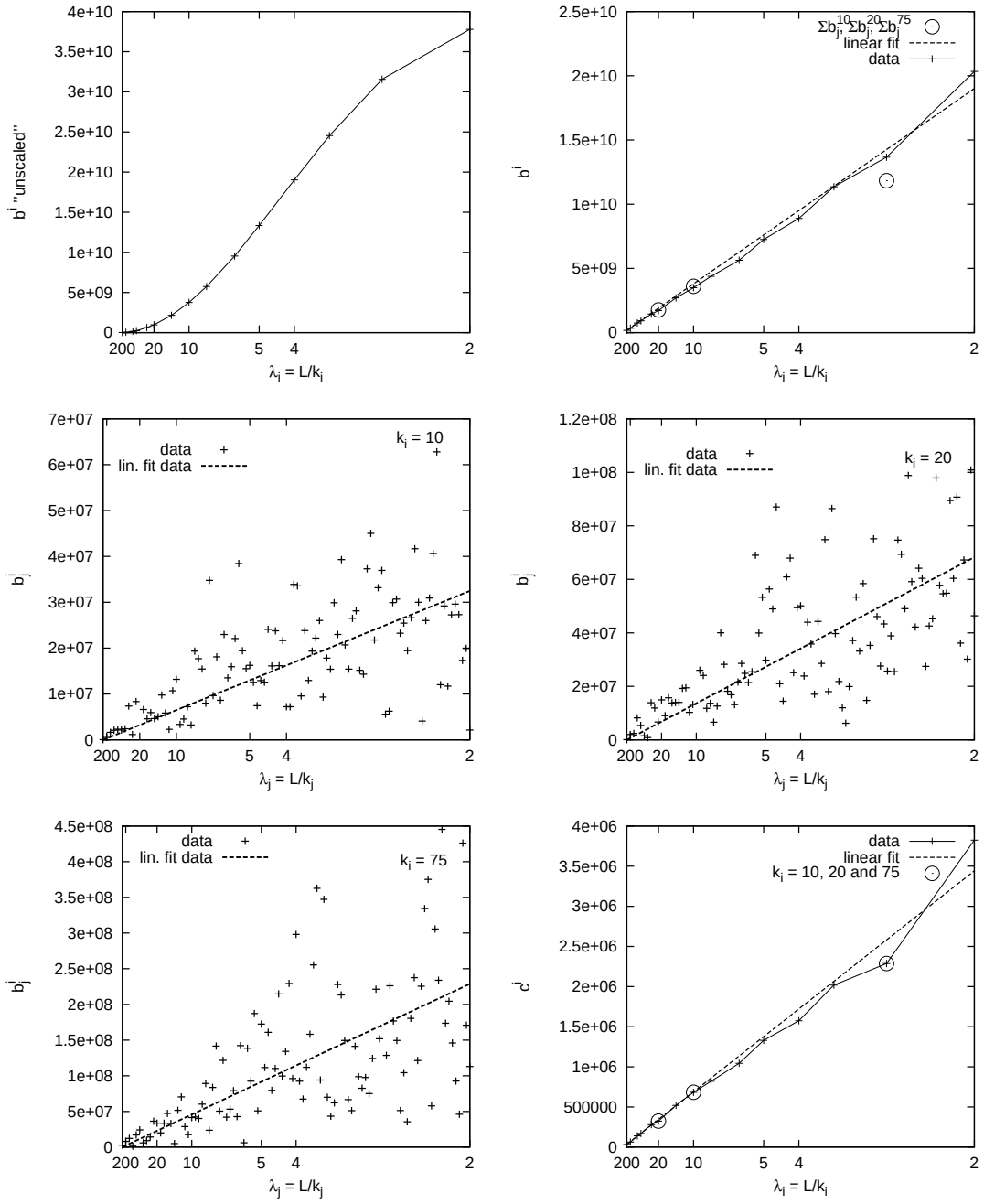

Figure 5.14: (Top-left) The "unscaled" b^i, (top-right) the b^i after scaling according to Eq. (5.4) with the linear fit $b^i = \hat{b}^i k_i$ with $\hat{b}^i \sim 1.9\,10^8$. (middle-left-right) and (bottom left) Fourier transform amplitudes scaled by the time to the power two, $A^i(k_j)/t^2$ at $t = 10$ which are in fact the $b^i_j = b^i(k_j) := b^i(k = j)$, for $i = k_i = 10, 20$ and 75 and $k = 1, 2, ..., B = 100$. The dashed line gives the linear fit: $b^i_j = c^i k_j$. (Bottom-right) The c^i for the 15 inserted wavenumbers, where the c^i with i =10, 20 and 75 are highlighted by circles. The dashed line gives the fit $c^i \approx \hat{c} k_i$ with $\hat{c} \sim 3.5\,10^4$.

The scaled b^i, objective with respect to the "breathing", are plotted in figure 5.14 (top-right). Here the increase with wavenumber is close to linear. As a check of consistency, the b^i and b^i_j must fulfill the relation $b^i = \sum_{j \neq i} b^i_j$ as indicated by the circles.

Figure 5.14 (middle-left/right and bottom-left) shows the rates $b^i_{j \neq i}$ for the full range of wavenumbers for $k^i = 10, 20$ and 75. The scaled amplitudes are divided by time squared, $b^i_j = \tilde{A}_i(k_j, t)/t^2$, at a time-step, $t/dt = 10$, within the fit time-window ($5 \leq t/dt \leq 50$). Note that the amplitudes strongly fluctuate within one graph and from one graph to the other for a given k_j. A linear fit, $b^i(k_j) = c^i k_j$, is proposed to capture the apparent monotonic linear increase of $b^i_{j \neq i}$ for increasing j. The set of c^i is plotted in figure 5.14, (bottom-right) also showing a linear increase.

From all these data, we conclude

$$b^i_j = \hat{c} k_i k_j, \tag{5.5}$$

with $\hat{c} \approx 3.5\,10^4$ in the framework of a linear growth assumption, $b^i_j = c^i k_j = \hat{c} k_i \sum k_j$. Note the symmetry $b^i_j = b^j_i$ from Eq. 5.5. The consistency relation $b^i = \sum_{j \neq i} b^i_j$ is nicely fulfilled and leads to $b^i = \sum_{j \neq i}^{B} c^i k_j = c^i(B(B+1)/2 - i)$, see the dotted line in Fig. 5.14 (top-right).

The same simulation and analysis procedure has been performed for eight different initial packings. Namely a different random number sequence has been chosen for the distribution of radii among the particles. The analysis results for each different packing are compared to the average over the packings in figure 5.15. Note that the average is performed on the data after applying the Fourier transform to the signals. Averaging the signals before the Fourier transform leads to different results, since the absolute value used for the power spectra is non-linear and makes it impossible to compare objectively the single results with the average. Averaging the signals before the Fourier transform in general smoothes out the out-of-phase high frequency components.

In general, the observations and the trends are the same for all the different packings and for the average. The latter however, shows a nice narrowing in the scatter of the data, see Fig. 5.14 (middle-left/right and bottom-left), which points out that a larger statistical study with 100 or even 1000 different packings may give even better and sharper results. The discussion of another possible functional behavior (e.g. a sine function) replacing the linear growth assumption, $b^i_j = c^i k_j$, is postponed until more simulations lead to better statistics.

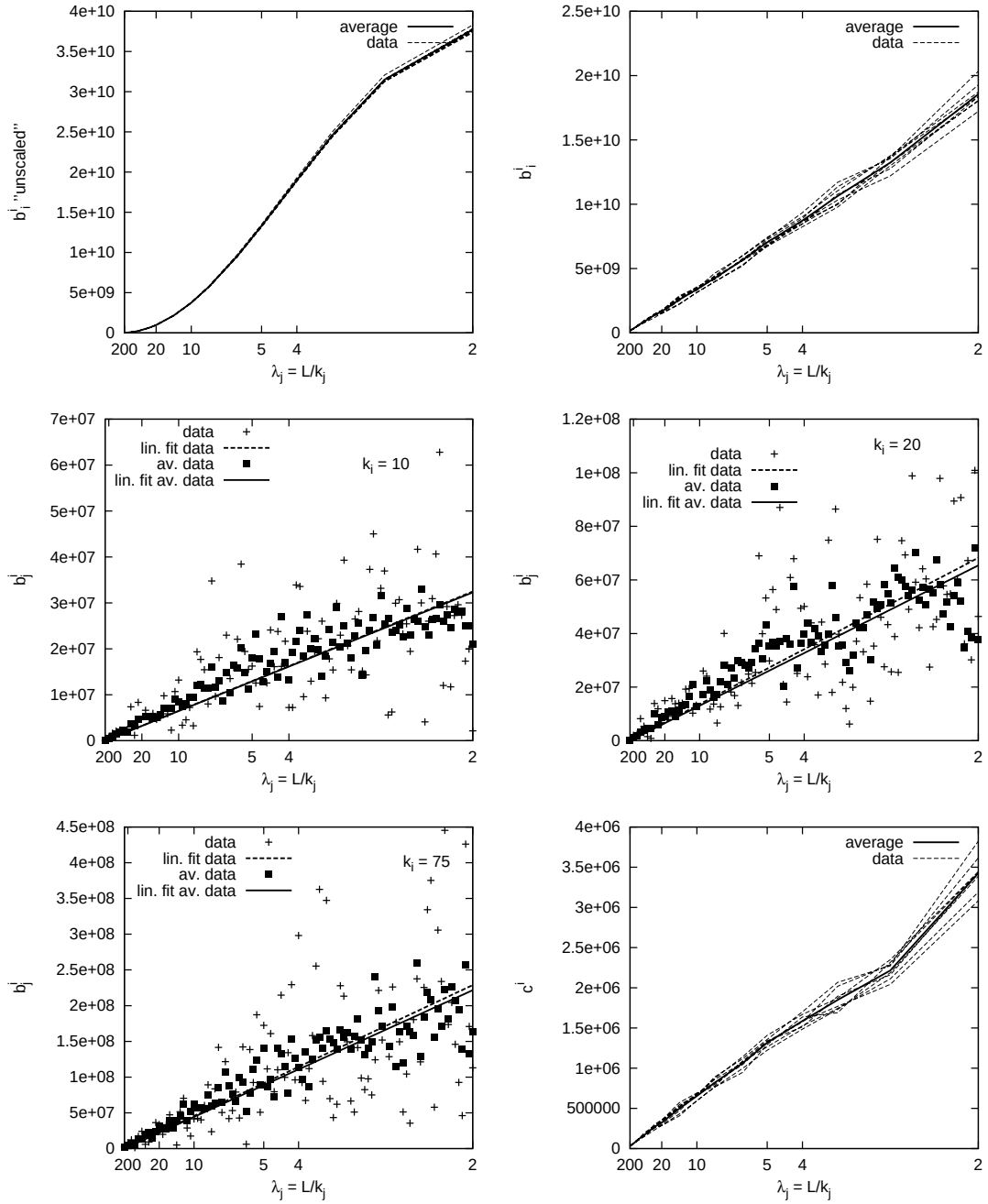

Figure 5.15: Comparison between the data for eight different packings (dotted lines or plus signs) and the average (solid lines or solid squares). (Top-left), the "unscaled" b^i, (top-right), the b^i after scaling according to Eq. 5.4, (middle-left-right) and (bottom left), the $b^i(k)$, for $i = k_i = 10, 20$ and 75 and $k = 1, 2, ..., 100$. This together with a linear fit, $b^i(k_j) = c^i k_j$. (Bottom-right) The c^i for the 15 inserted wavenumbers.

"Bi-chromatic" mode mixing nonlinearity

In order to study the non-linear effects due to the interactions between the wave-numbers, some simulations have been performed using the same wave agitation procedure as described in section 5.2.3, but this time with two inserted wavenumbers superimposed initially. The wave-form given as initial condition is then:

$$v_z \left(\sin((2\pi z_{layer})/\lambda_1) + \sin((2\pi z_{layer})/\lambda_2)\right),$$

as sketched in Fig. 5.16.

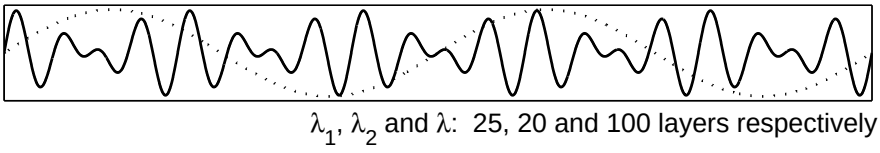

Figure 5.16: Schematic graph of the inserted superimposed wavelengths $k_8 = L/\lambda = 200/25$ and $k_{10} = L/\lambda = 200/20$ (solid line) and the created or amplified wave-number $k_2 = k_{10} - k_8$ corresponding to the wavelength $\lambda = 100$ (dotted line).

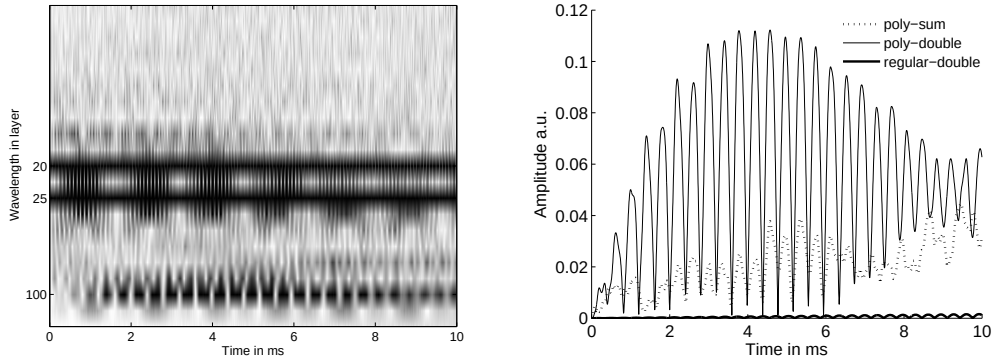

Figure 5.17: (Left) Wavelength (vertical, in units of layers) as function of time (horizontal, in units of ms). The inserted "bi-chromatic" wavelengths $\lambda = 25$ and 20 (in units of layers) from top-left to bottom-right (white, gray, and black correspond to low, medium and high intensity for the absolute value of the Fourier components). (Right) The time evolution of the amplified/created wavelengths ($\lambda = 100$ layers) for the "bi-chromatic" agitation given by the solid line, labeled as poly-double. The sum of the contributions from the "mono-chromatic" agitations from the previous section, is given by the dotted line, labeled as poly-sum. And the 'bi-chromatic" agitation in a fully regular packing is given by the thick solid line, labeled as regular-double.

In the presented results two wave-numbers $k_8 = L/\lambda = 200/25$ and $k_{10} = L/\lambda = 200/20$ are "beating" (constructive interference) with each-other amplifying significantly the wave-number $k_2 = k_{10} - k_8$ corresponding to the wavelengths $\lambda = 100$ as Fig. 5.17 (Left) nicely shows it. The term amplified has been used here as Fig. 5.17 (Right) shows that this wavelength is also present in the single inserted wavelengths $\lambda = 25$ and $\lambda = 20$ simulations from the previous section (the sum of the contributions have been plotted). Also for the regular packing, Fig. 5.17 (Right, thick solid line) a tiny but clear "beating" is observed. However for the "bi-chromatic" excitation of the weakly polydisperse system the low wavelength $\lambda = 100$ is clearly stronger. This interesting result allows, in a future study, to use the simulation results as input for the generalized non-linear problem dealing with the mixing of modes, see Eq.(5.3).

5.2.4 Solution of the Master-Equation

In this section, we numerically solve the Master-Equation (ME) using the values extracted from the simulations.

$$b_j^i = \hat{c} k_i k_j \ , \tag{5.6}$$

with $\hat{c} = 3.4\,10^4\,\mathrm{s}^{-2}$, which implies the linear growth assumption $c^i = \hat{c} k_i$.

Note that τ in Eq. (5.2) had to be replaced by t^2 in order to capture the functional behavior of the early time evolution $A_j^i \propto t^2$. With other words, the ME is solved with τ, but then $t = \sqrt{\tau}$ is plotted on the time axis. There is no physical explanation for this re-scaling of the time-axis so far.

In Fig. 5.18 the wavenumber intensity $q(k_j)$ is plotted against time for four inserted wavenumbers. Like in the simulations, the intensity remains rather long in the inserted bands for small i =2. It remains for some time, before it is transferred to all other bands for intermediate bands i =10 and 20. And it remains for some short time, before it is also transferred to all other bands for i =75.

In Fig. 5.19 the wavenumber intensity $q(k_j)$ is plotted against time for two pairs of inserted wavenumbers $i_1 = 8$ & $i_2 = 10$, and $i_1 = 10$ & $i_2 = 15$. Like in the particle simulations, the intensity remains in the inserted bands for some time before it is transferred to all other bands. In the solution of the linear Master-Equation, there is no trace of the constructive interference observed in the particle simulations.

In conclusion, the Master-Equation (ME) predicts qualitatively the early stage evolution of monochromatic standing waves with time. The Fourier components intensity of the inserted wavenumber is slowly transferred to other modes.

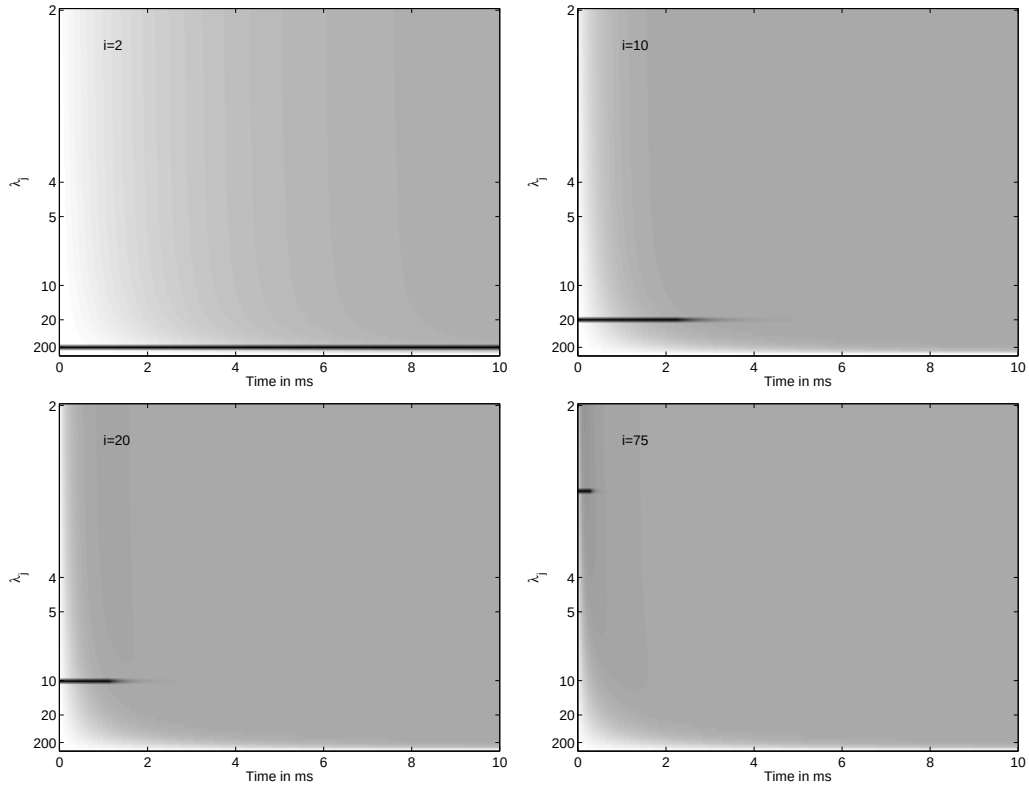

Figure 5.18: Wavenumber spectrum as function of time obtained from Eq. (5.2) using $\hat{c} = 3.4\,10^4\,\mathrm{s}^{-1}$, for different inserted wavenumbers k_i, with i =2, 10, 20 and 75. Dark, grey and white correspond to high, medium and low intensity.

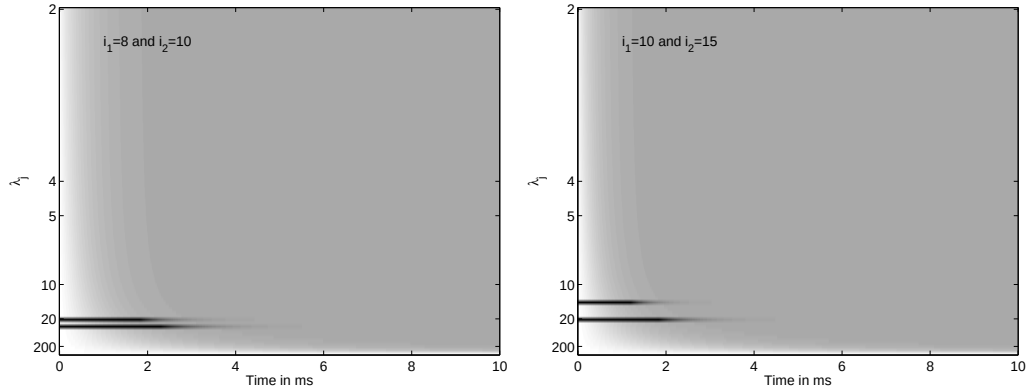

Figure 5.19: Wavenumber spectrum as function of time obtained from Eq. (5.2) using $\hat{c} = 3.4\,10^4\,\mathrm{s}^{-1}$, for two pairs of simultaneously inserted wavenumbers k_i, with $i_1 = 8$ & $i_2 = 10$, and $i_1 = 10$ & $i_2 = 15$. Dark, grey and white correspond to high, medium and low intensity.

The linear ME cannot predict the cross-talk between bands and therefore the long-time behavior from simulations, i.e., the fact that energy is mainly present in the low bands, is not reproduced. Instead, the linear ME predicts a constant, homogeneous distribution of energy $q_i = \text{const.} = 1/B$, with B the number of bands, among all bands after sufficiently long time.

5.2.5 Eigenmodes of a slightly polydisperse packing

It is possible and interesting to calculate the eigenmodes (eigenvalues and eigenvectors), from the previously considered packings, both regular and polydisperse. This gives additional insight on the packings and can explain the way they react under dynamic pulses, as in section 5.1.3, and the standing waves, as earlier in this chapter, see section 5.2.3, in the discrete element simulations.

Eigenvalue problem

The calculation of the eigenmodes of a packing based on different configurations, using the particle positions and masses and the contact stiffness employ a similar approach as in section 3.2, but in this case without tangential elasticity and hence without rotational degrees of freedom. Those could be included in future investigations.

Particle interactions The contact law defines the interaction between the two particles by relating the force to the displacement. In contrast to the "one-sided" particle contact law, for which contacts can open, the chosen law here is "two-sided" linear-elastic, meaning that no particle rearrangement, separation or irreversible sliding is allowed (which makes the particle system equivalent to a mass-spring system with fixed topology). Note that therefore stiff particles, with point-contacts, are considered and only very small deformations are allowed. The contact force $\boldsymbol{f}_i^c$ acting on particle i at contact c can be written as:

$$\boldsymbol{f}_i^c = -\boldsymbol{K}^c \cdot (\boldsymbol{u}_i - \boldsymbol{u}_j) \tag{5.7}$$

with $\boldsymbol{u}_i$ the displacement vector of particle i. The particles i and j form the pair of particles interacting with each other at contact c. The stiffness matrix related to particle i as:

$$\boldsymbol{K}^c = k_n \boldsymbol{n}^c \boldsymbol{n}^c. \tag{5.8}$$

with k_n the normal contact stiffness and $\boldsymbol{n}^c$ the normal vector at contact c from particle i to j. Note that no tangential stiffness is included.

Balance of momentum The conservation laws for linear momentum (Newton's second law) states:

$$m_i \ddot{\boldsymbol{u}}_i = \sum_{c=1}^{C_i} \boldsymbol{f}_i^c \ , \tag{5.9}$$

with m_i the mass of particle i and C_i the total number of contacts of particle i.

We define now $\boldsymbol{U}$, the displacement (translation) vector of dimension $3N$ of all particles:

$$\boldsymbol{U} = (u_1^x, u_1^y, u_1^z, u_2^x, u_2^y, u_2^z, ..., u_N^x, u_N^y, u_N^z)^T. \tag{5.10}$$

with u_i^x, u_i^y, u_i^z the x, y, z displacements of particle i and N the number of particles.

The combined conservation laws for all particles then can be written as:

$$\boldsymbol{M} \cdot \ddot{\boldsymbol{U}} = \boldsymbol{F} \tag{5.11}$$

with $\boldsymbol{M}$ the mass matrix and $\boldsymbol{F}$ the force vector.
The mass matrix

$$\boldsymbol{M} = \begin{pmatrix} m_1\boldsymbol{I}^3 & 0 & 0 & 0 \\ 0 & m_2\boldsymbol{I}^3 & 0 & 0 \\ 0 & 0 & ... & 0 \\ 0 & 0 & 0 & m_N\boldsymbol{I}^3 \end{pmatrix} \tag{5.12}$$

is diagonal of dimension $3N \times 3N$. and $\boldsymbol{I}^3$ the 3x3 identity matrix in three dimensions.
The generalized force vector $\boldsymbol{F}$ of dimension $3N$ is expressed as:

$$\boldsymbol{F} = (\sum_{c=1}^{C_1} \boldsymbol{f}_1^c, \sum_{c=1}^{C_2} \boldsymbol{f}_2^c, ..., \sum_{c=1}^{C_N} \boldsymbol{f}_N^c)^T \tag{5.13}$$

Equation (5.11) can be rewritten as

$$\boldsymbol{M} \cdot \ddot{\boldsymbol{U}} + \boldsymbol{K} \cdot \boldsymbol{U} = 0 \tag{5.14}$$

with $\boldsymbol{K}$ the positive-definite global stiffness matrix, of dimension $3N \times 3N$, such that $\boldsymbol{F} = -\boldsymbol{K} \cdot \boldsymbol{U}$

A harmonic wave solution in time is assumed for the particle displacements. Thus

$$\boldsymbol{U}(t) = \boldsymbol{A}_0 \exp(i\omega t) \tag{5.15}$$

with $\boldsymbol{A}_0$ the translational displacement amplitudes, ω frequency and t time.

Finally, equation (5.14) becomes:

$$\left(\boldsymbol{K} - \omega^2 \boldsymbol{M}\right) \cdot \boldsymbol{A}_0 = 0 \tag{5.16}$$

Solving this generalized eigenvalue problem numerically leads to $3N$ positive eigenvalues $\lambda_e = \omega_e^2$, $(e = 1, ..., 3N)$ and $3N$ eigenvectors $\boldsymbol{A}_e$.

Dispersion relation and density of states

For both the regular and the weakly polydisperse packing, using the same radii, masses and stiffness as simplification, see section 5.2.3 for more details, the eigenmodes have been calculated.

A histogram of the eigenvalues λ_e gives the density of states for the considered packing. Fig. 5.20 shows the density of states for both the regular (left) and the polydisperse (right) packing.
The finite and non-cubic dimension of the regular packing is clearly visible from the many isolated peaks. The peak at ∼35 kHz corresponds to the oscillation of two layers together in the z-direction, as this frequency correspond to a wavelength of two layers in the z direction according to the dispersion relation, see Fig. 5.21 (left). The second largest peak at ∼24 kHz corresponds to a wavelength of four layers in the x (or y) direction, according the dispersion relation, see Fig. 5.21 (left), which is exactly the dimension of the packing in that direction.
As a consequence of contact disorder (mainly) the density of state for the weakly polydisperse packing, Fig. 5.21 (right), is much smoother than for the regular one. However the peak at ∼35 kHz is still visible.

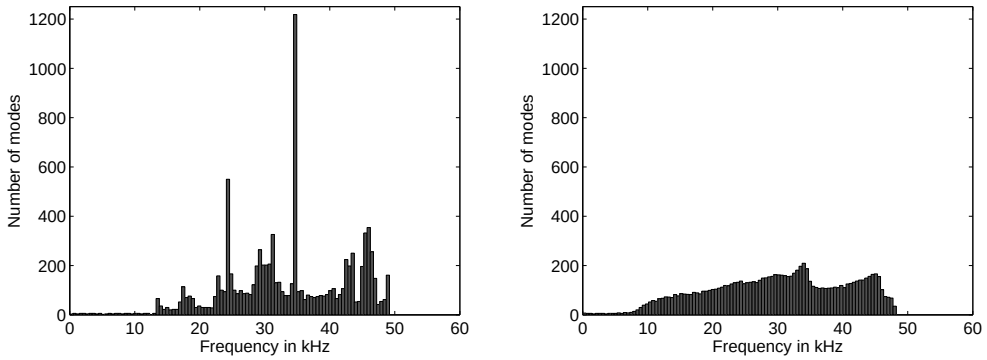

Figure 5.20: Density of states from the eigenmode calculation in a regular (left) and a polydisperse (right) packing

From the results it is also possible to derive the dispersion (frequency-wavenumber) relation. The latter is derived for both longitudinal and transversal modes in the

long z-direction (see Sec. 5.2.3). Therefore, the components of each eigenvector, $\boldsymbol{A}_e^z$ for the longitudinal modes and $\boldsymbol{A}_e^x$, for the transversal modes ($\boldsymbol{A}_e^y$ would give the second transversal relation, data not shown here) are fitted in the z-direction by the function:

$$R_1 \cos(2\pi N_l z(i)/L) + R_2 \cos(2\pi N_l z(i)/L) \tag{5.17}$$

for each wavenumber N_l =1,...,100, where L is 200.
Note that the coefficients $R_1(N_l, \lambda_e)$ and $R_2(N_l, \lambda_e)$, depend on the wavenumber N_l and eigenvalue λ_e. They are chosen by a least-square approach such that they minimize the residual of the actual displacement and the assumed wavenumber dependent form.

$$(\sum_{i=1}^{N}(A_e(i) - (R_1 \cos(2\pi N_l z(i)/L) + R_2 \sin(2\pi N_l z(i)/L))))^2. \tag{5.18}$$

Afterward $R(N_l, e) = \sqrt{R_1(N_l, e)^2 + R_2(N_l, e)^2}$ is calculated.
The obtained $(N_l \times N_l)$ matrix $R(N_l, e)$ is plotted in Fig. 5.21 where the second dimension (frequency) has been mapped in 100 frequency bins.

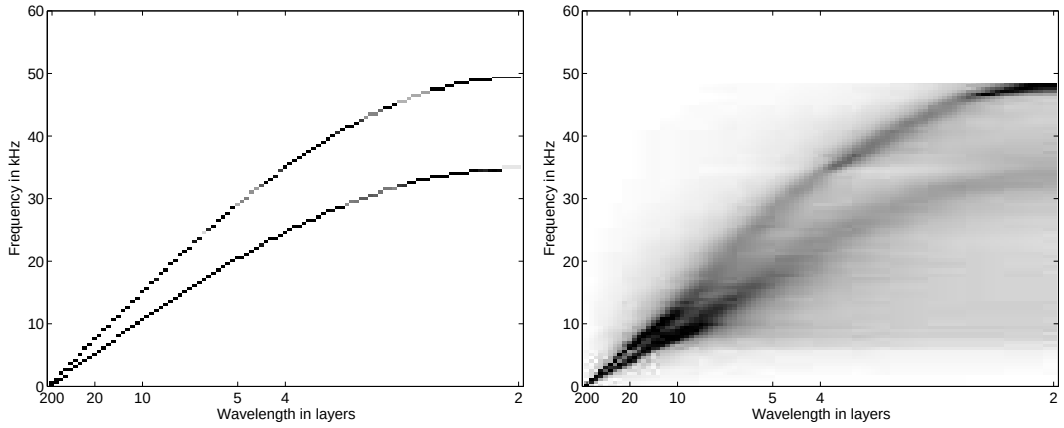

Figure 5.21: Dispersion relations from the eigenmode calculation for both normal- and tangential-displacements in the z-direction in the regular packing (left) and in the polydisperse packing (right)

As expected for the regular packing, see Fig. 5.21 (left), the dispersion relation is a perfect sine function for both longitudinal and transversal modes. This result was also obtained elsewhere from detailed simulation data, see Sec. 4.1.3. For the weakly polydisperse packing, a less sharp dispersion relation is obtained, also similar to previous results, see sections 5.1.3 and 5.2.3. While this calculation does only confirm the already known behavior, the interesting potential of this

method is the possibility to explicitly write down the time evolution of an initial wave-form expressed as a sum of eigenmodes. The results can then be compared to the simulation presented in section 5.2.3. This study, however, is not part of this work.

5.2.6 Summary and conclusions

Inspired by previous numerical results on the dispersive behavior of the wave propagation in weakly polydisperse granular packings, see section 5.1.3, the purpose of this section was to understand how single wavelengths or wavenumbers evolve in time. In other words, the central question is how is energy transferred between different frequency- (or wavenumber) bands? More generally, the idea is to model the energy density of waves in a disordered system by a linear Master equation and test this approach by comparison with simplified model systems with discrete particle simulations. The only parameter for the Master equation, $\hat{c}$ was extracted from the simulations. In future, the observed non-linear effects can be translated into the adapted Master Equation for energy-transport and evolution. Both linear and non-linear terms can be determined from the simulations involving, e.g., energy-transfer between the bands, but also frequency mixing.

Several simulations with different inserted initial wavenumbers have been performed for eight different weakly polydisperse packings. The results show a low source and target energy transfer rate, from the inserted wavenumber to the others, increasing with wavenumbers. These strong fluctuations have been approximated by a linear growth assumption and all results have been checked for self consistency. Future statistical studies with averaging over many more packings should be able to increase to quality of the results and to investigate the validity of the linear growth assumption. The simulation results have been used as input parameters for the adapted Master equation. The results show a similar qualitative behavior for the transfer of energy. However, no non-linear cross-talk between inserted wavenumbers has been obtained as observed in the simulations. The Master equation must be improved in order to take into account those effects as well.

Finally, the eigenmodes of both a regular and a weakly polydisperse packing have been calculated. This gives a better insight on their behavior concerning the dispersion relation as already, probed by dynamic wave propagation simulations. The influence of the packing dimension and structure is revealed and the foundation for a more detailed study of the eigenmode shapes is provided.

6

Conclusions and Outlook

Conclusions: In this thesis sound wave propagation through different types of confined granular systems has been studied. In particular, the role and the influence of several micro contact properties: friction, particle rotation, contact disorder, and dissipative contacts on the macro-scale sound wave propagation have been investigated. This has been done with help of three-dimensional discrete element simulations, theory and experiments. Besides results on regular lattice structures and some results on fully disordered systems, the main focus of this thesis is on systems with strong contact disorder (contact forces) and inhomogeneity but weak geometrical disorder (system structure). Sound propagation was examined in one direction, i.e. the "long" direction of the system, where the two perpendicular ones are "short". In various configurations and with many different contact properties, the goal was to better understand the different mechanisms of wave propagation as introduced in chapter 1 and summarized in the following.

The attenuation of a wave due to inter-particle viscous damping, linear velocity dependent, has been studied with the goal to better understand real damping in experiments. The results show that the strongest effect is observed when the contact relaxation (dissipation) time and the contact duration time are similar (see Sec. 4.1.3). The "coda" (oscillations following the first main oscillations) of the time signals, that is to say the high frequencies (short wavelengths), are most affected by damping. This observation was confirmed by the frequency analysis done with the spectral ratio technique. For larger frequencies nonlinear, increasing damping is observed (see Sec. 2.3). The combination of two methods used to analyze the attenuation made it possible to describe in detail the characteristics and the influence of the contact damping on the wave propagation. It would be very interesting to use this analysis to test different models for attenuation in the

system in parallel with simple and precise experiments, and possibly even to add interstitial fluids with different viscosities.

The theoretical predictions on the dispersive nature of sound waves in a regular granular packing were confirmed and accurately reproduced by the simulations. Taking as reference the maximum of the first oscillation peak of time signals, the results show an interesting acceleration of the pulse near the source. This effect is due to the strong dispersion of the wave near the source when the high frequencies (wavelength of the order of the particle size) are much slower than the lower frequencies (longer wavelength) that need time and space to fully develop. When the first oscillation's main frequency is low enough (after few tens of particle diameters when the pulse has broadened) the wave propagation reaches a more stable state. Those results were obtained, for both P- and S-waves.
A single Fourier transform of the space, or time signals, gives information on the wave-number or frequency content of the wave and its evolution in time or space respectively. For example, the frequency content can be visualized as function of distance from the source. The double Fourier transform of the space-time signals gives the dispersion relations which are rich in information about the important and complex frequency dependence of wave propagation in granular materials. Dispersion relations for regular lattices are perfectly understood, while those for the slightly disordered systems resemble the first step towards understanding fully disordered systems.

The results obtained from the inclusion of rotational degrees of freedom together with tangential restoring forces at the contact show additional modes with energy conversion between them. This confirms the necessity to include the rotational degrees of freedom into the description of wave propagation in real granular materials. The obtained dispersion relations show that a part of the energy of a shear wave is converted to a rotational wave. The wave propagation speed, the wave dispersion and the frequency filtering behavior are all affected by the tangential stiffness, as it is clearly visible in the results. Simulations and theory are in perfect quantitative agreement for regular lattices, providing the foundation to understand also disordered systems with tangential elasticity and rotations.

Starting from a regular lattice, a first small step towards disorder is made by introducing a controlled weak disorder in size. Doing this, allows to separate the contact disorder from structural disorder which allows to isolate and study different issues one by one. The results show clearly that contact disorder is responsible for an important feature of wave propagation in granular materials, which is frequency filtering.

Another aspect related to the weak polydispersity is the dispersion with respect to the evolution in time of single wavenumbers (or wavelengths). A detailed

study of how energy is transfered between different wavenumber bands has shown low energy transfer rates, from the inserted wavenumber to the other ones, for small wavenumbers. The energy transfer rates are increasing linearly for increasing source and target wavenumbers. Inserting the simulation results in an adapted Master equation approach leads to quantitative agreement for short times, qualitative agreement for intermediate times, and incorrect predictions for the long time limit due to the lack of non-linear terms in the Master Equation to be added in the future.

Making an even bigger step up in complexity by probing a realistic tablet made of a sintered frictional and cohesive powder has shown the potential of the numerical simulation method, together with the necessity to consider large enough systems in order to capture with sufficient contrast the studied wave phenomena. Future research is needed to investigate more carefully the effects of increasing disorder together with all its further implications.

The numerical part of the study has clearly shown the usefulness of discrete element simulations for a better understanding of wave propagation in granular materials. It allows a detailed analysis and description of granular packings and of the propagating waves in both space-time and wave-number as well as frequency space based on high resolution space-time signals. In addition, one of the main advantages is the possibility to separately tune each parameter of the model and study in detail their role and influence on the wave propagation by reducing the complexity. Particle simulations are a valuable tool to complement theoretical and experimental approaches in order to enhance the understanding of complex phenomena as sound propagation in (dry) granular materials.

Outlook: In the following several remarks and recommendations are given for subsequent studies.

The main part of this work concerns the study of different wave agitation types, as dynamic pulses and standing waves, in an elongated weakly polydisperse packing. This is an intermediate case with many advantages half-way between regular perfectly ordered and fully disordered systems. Evidently, the fully disordered system remain a challenge for future research.

It is also important to complete the study of this relatively simple system by considering different, more realistic contact models and contact properties. The results obtained in this work should be tested and quantitatively compared to experiments with respect to different frictional contact models, as for example those based on the Hertz-Mindlin model. Also the influence and competition of sliding, rolling and torsion should be studied in more detail in order to determine their role in the wave propagation dynamics. The theoretical study of the rotational

branches related to rotational degrees of freedom should be extended for this purpose. Future investigations should interpret and understand the eigen-vectors obtained by the theoretical derivation. Also, it would be interesting to consider non-Bravais lattices as the Hexagonal Closed Packing (HCP) lattice where optical and rotational modes should co-exist.
This point could get a high priority, especially as rolling friction is often introduced in the literature within theoretical approaches, but it is not clear whether their role is crucial.
Special attention should be given to modeling attenuation. The linear velocity-dependent viscosity introduced in the simulations is a rather simple way to obtain energy loss in the system and does not necessarily reproduce the attenuation observed in real experiments. In particular, energy losses due to local breakage and heat losses should be considered too. The study of cohesive powders should be continued in larger samples where the effects of contact adhesion on the general wave propagation behavior should be more visible.

The weak disorder introduced in the granular packings, at the contact level mainly, should be gradually increased up to a fully disordered packings. This would allow to compare the results with more realistic granular materials such as polydisperse glass beads or even sand. The challenge, however, lies in the limitation of the number of particles with respect to computation time. A compromise between a large enough representative sample and a reasonable computation time allowing extensive parameter studies should be found. Note that an increasing size distribution width for the particles can lead to an overwhelming increase of computation time. Also, in the case of full disorder, we recommend to give extra attention to the sample preparation procedure. A balance must be realized between sample density, confining pressure and realistic contact deformation. A too large confining pressure could lead to unrealistic overlap between the particles and hence violate the assumption of tiny deformations. Even if simulations offer many advantages as compared to real experiments, the sample preparation always remains the first important issue to be addressed.

The new Master equation theory proposed for the linear time evolution of single (double or multiple) wavenumbers in a granular packing should be improved in order to take into account the non-linear effects seen in the simulations, as the cross-talk between wavenumbers. The relation between eigenmodes in an elastic system and the energy-band evolution must be worked out.

In general, for the simulations, a more systematic statistical study involving many different initial packings should be done. This would increase the quality of the results and filters out the configuration-dependent effects that might be present.

Finally, for experiments, the *Spectral Ratio Technique* introduced in the second chapter, should be applied to better experimental results. The experimental set-up and the sample preparation procedure have to be especially planned and tuned with the perspective to apply the method. A strict quality control is needed for the material state and a reproducible and objective coupling between the sample and the transducers is crucial.

Bibliography

[1] I. Agnolin, J. T. Jenkins and L. La Ragione A continuum theory for a random array of identical, elastic, frictional disks. *Mechanics of Materials*, 38(8-10):687–701, 2006.

[2] M. P. Allen, D. J. Tildesley. Computer Simulation of Liquids. *Oxford University Press*, Oxford, 1987.

[3] R. Andersson, W. G. Bouwman, and I. M. de Schepper. Superfine powders of silica studied with spin-echo small-angle neutron scattering. In *Powders and Grains*, pages 13–15, Stuttgart, Germany, 2005.

[4] R. Andersson, W. G. Bouwman, S. Luding, and I. M. de Schepper. Stress, strain and bulk microstructure in a cohesive powder. *Physical Review E*, 77(051303):1–8, 2008.

[5] J. Anfosso, V. Gibiat. Elastic wave propagation in a three-dimensional periodic granular medium. *Europhysics Letters*, 67(3), 376-382, 2004.

[6] N. W. Ashcroft, N. D. Mermin. *Solid State Physics* Brooks Cole publishers, ISBN:0030839939, 1976.

[7] T. Aste, M. Saadatfar, A. Sakellariou, and T.J. Senden. Investigating the geometrical structure of disordered sphere packings. *Physica A*, 339:16–23, 2004.

[8] T. Aste, M. Saadatfar, and T. J Senden. Geometrical structure of disordered sphere packings. *Physical Review E*, 71:061302, 2005.

[9] Y. M. Bashir, J. D. Goddard. A novel simulation method for the quasi-static mechanics of granular assemblages. *J. Rheol.*, 35 (5) (1991) 849–885.

[10] M. Bath. *Spectral Analysis in Geophysics*, (Development in Solid Earth Geophysics). Elsevier Science Ltd (December 1974), ISBN-10: 0444412220.

[11] R. P. Behringer. The dynamics of flowing sand. *Nonlinear Science Today*, 3 (1993) 1–15.

[12] R. P. Behringer, G. W. Baxter. Pattern formation and complexity in granular flow. In: A. Mehta (Ed.),*Granular Matter*, Springer-Verlag, New York, 1994, p. 85.

[13] J. P. Bouchaud, M. E. Cates, P. Claudin. Stress distribution in granular media and nonlinear wave equation. J. Phys. I, France 5, 639-656, 1995.

[14] T. Bourbie, O. Coussy, B. Zinszer. Acoustics of Porous Media. Gulf Publishing Company, 1987, ISBN-10: 0872010252.

[15] R.B. Bracewell. *The Fourier Transform and its Applications*. McGraw-Hill, New York, 2000.

[16] L. Brendel and S. Dippel. Lasting contacts in molecular dynamics simulations. In H. J. Herrmann, J.-P. Hovi, and S. Luding, editors, *Physics of Dry Granular Media*, page 313, Dordrecht, 1998. Kluwer Academic Publishers.

[17] T. Brunet, X. Jia, P. Mills. Mechanisms for acoustic absorption in dry and weakly wet granular media. *Physical Review Letters*, 101 (13), art. no. 138001, 2008.

[18] A. Castellanos. The relationship between attractive inter-particle forces and bulk behavior in dry and uncharged fine powders. *Advances in Physics*, 54 (4) (2005) 263–376.

[19] C. S. Chang, S. J. Chao, Y. Chang. Estimates of elastic moduli for granular material with anisotropic random packing structure. *Int. J. Solids & Structures*, 32 (14) (1995) 1989–2009.

[20] C. S. Chang and J. Gao. Nonlinear dispersion of plane-wave in granular media. *Int. J. Non-Linear Mech.*, 30(2):111-128, 1995.

[21] C. Coste, B. Gilles. On the validity of Hertz contact law for granular material acoustics. *Eur. Phys. J. B*, 7, 155-168, 1999.

[22] C. Coste, B. Gilles. Low-Frequency behaviour of beads constrained on a lattice. *Physical Review Letters*, 90(17), art. no. 174302, 2003.

[23] C. Coste, B. Gilles. Sound propagation in a constrained lattice of beads: High-frequency behavior and dispersion relation. *Physical Review E*, Statistical, Nonlinear, and Soft Matter Physics 77 (2), art. no. 021302, 2008.

[24] P. A. Cundall and O. D. L. Strack. A discrete numerical model for granular assemblies. *Géotechnique*, 29(1):47–65, 1979.

[25] Sound Propagation and Force Chains in Granular Materials. *Invited talk*, Opening Workshop: Program on Random Media September 2007, SAMSI, Research Triangle Park, NC.

[26] C. T. David, R. G. Rojo, H. J. Herrmann, S. Luding. Hysteresis and creep in powders and grains. In: R. Garcia-Rojo, H. J. Herrmann, S. McNamara (Eds.). *Powders and Grains 2005*, Balkema, Leiden, Netherlands, 2005, pp. 291–294.

[27] N. Dejong, L. Hoff, T. Skotland, N. Bom. Absorption and scatter of encapsulated gas filled microspheres - Theoretical considerations and some measurements. *Ultrasonics*, 30(2): 95-103, 1992.

[28] J. Duran, A. Reisinger. Sands, Powders, and Grains: An Introduction to the Physics of Granular Materials. Springer-Verlag New York, Inc., New York, 1999, ISBN: 0-387-98656-1.

[29] P. Eshuis, K. van der Weele, D. van der Meer, R. Bos, D. Lohse. Phase diagram of vertically shaken granular matter. *Physics of Fluids*, 19 (12), art. no. 123301, 2007.

[30] A. L. Fetter and J. D. Walecka. *Theoretical Mechanics of Particles and Continua*. Dover Publisher, 2003.

[31] M. Frehner, S. M. Schmalholz, E. H. Snger, H. Steeb. Numerical modeling of wave propagation in heterogeneous and partially saturated rocks. *Phys. Earth. Planet. Int.*, submitted 2007.

[32] R. Garcia-Rojo, H. J. Herrmann, and S. McNamara, editors. *Powders and Grains 2005*, Leiden, 2005. A. A. Balkema Publishers.

[33] J. D. Goddard. Nonlinear elasticity and pressure-dependent wave speeds in granular media. *Proc. R. Soc. Lond. A*, 430, 105-131, 1990.

[34] I. Goldhirsch, G. Zanetti. Clustering instability in dissipative gases. *Phys. Rev. Lett.*, 70 (11) (1993) 1619–1622.

[35] E. F. Grekova, G. C. Herman. Wave propagation in rocks modeled as reduced cosserat continuum with weak anisotropy. *67th European Association of Geoscientists and Engineers, EAGE Conference - Extended Abstracts*, pp. 2643-2646, 2005.

[36] E. Hascoet, H. J. Herrmann, V. Loreto. Shock propagation in a granular chain. *Phys. Rev. E*, 59(3) 3202-3206, 1999.

[37] K. J. Hedlin (Husky Energy) and G. Margrave (University of Calgary) Seismic attenuation problem.

[38] O. Herbst, M. Huthmann, A. Zippelius. Dynamics of inelastically colliding spheres with Coulomb friction: Relaxation of translational and rotational energy. *Granular Matter*, 2 (4) (2000) 211–219.

[39] O. Herbst, R. Cafiero, A. Zippelius, H. J. Herrmann, S. Luding. A driven two-dimensional granular gas with Coulomb friction. *Phys. Fluids*, 17 (2005) 107102.

[40] H. J. Herrmann, J.-P. Hovi, S. Luding (Eds.). Physics of dry granular media, NATO ASI Series E 350. *Kluwer Academic Publishers*, Dordrecht, 1998.

[41] H. Hinrichsen and D.E. Wolf. *The Physics of Granular Media*. Wiley-VCH, Weinheim, 2004.

[42] S. R. Hostler and C. E. Brennen. Pressure wave propagation in a shaken granular bed. *Phys. Rev. E*, 72:031304, 2005.

[43] H. M. Jaeger, C. Liu, S. R. Nagel. Relaxation at the angle of repose. *Phys. Rev. Lett.*, 62 (1) (1989) 40–43.

[44] H. M. Jaeger, C. Liu, S. R. Nagel, T. A. Witten. Friction in granular flows. *Europhys. Lett.*, 11 (7) (1990) 619–624.

[45] H. M. Jaeger and S. R. Nagel. Physics of the granular state. *Science*, 255(5051):1523–1531, 1992.

[46] H. A. Janssen. Versuche über Getreidedruck in Silozellen. *Zeitschr. d. Vereines Deutscher Ingenieure* 39 (35) (1895) 1045–1049.

[47] J. Jenkins, D. Johnson, L. La Ragione, H. Makse. Fluctuations and the effective moduli of an isotropic, random aggregate of identical, frictionless spheres. *Journal of the Mechanics and Physics of Solids*, 53(1):197–225, 2005.

[48] X. Jia, C. Caroli, and B. Velicky. Ultrasound propagation in externally stressed granular media. *Physical Review Letters*, 82(9):1863–1866, 1999.

[49] X. Jia. Codalike multiple scattering of elastic waves in dense granular media. *Phys. Rev. Lett.*, 93(15):154303, 2004.

[50] S. Job, F. Melo, A. Sokolov, S. Sen. Solitary wave trains in granular chains: Experiments, theory and simulations. *Granular Matter*, 10 (1), pp. 13-20, 2007.

[51] K. D. Kafui, C. Thornton. Numerical simulations of impact breakage of spherical crystalline agglomerate. *Powder Technology*, 109 (2000) 113–132.

[52] O. Kelder, D. M.J. Smeulders. Observation of the Biot slow wave in water-saturated Nivelsteiner sandstone. *Geophysics*, 62: 1794-1796, 1997.

[53] O. Kelder. Frequency-dependent wave propagation in water-satured porous media. *PhD thesis*, Delft University of Technology, 1998.

[54] Y. Kishino (eds) *Powders and Grains 2001*, Balkema Rotterdam, 2001.

[55] M. Kleer. A triaxial cell for the experimental investigation of wave phenomena under certain stress states. *Master thesis*, Saarland University, *in preparation.*

[56] M. Lätzel, S. Luding, H. J. Herrmann, D. W. Howell, R. P. Behringer. Comparing simulation and experiment of a 2d granular Couette shear device. *Eur. Phys. J. E*, 11 (4) (2003) 325–333.

[57] L. Li, R. M. Holt, A. P. G, O-M. Nes. Simulating wave propagation using a discrete element method. *EAGE 65th Conference & Exhibition* Stavanger, Norway, June 2003.

[58] C.-h. Liu and S. R. Nagel. Sound in sand. *Phys. Rev. Lett.*, 68(15):2301–2304, 1992.

[59] C.-h. Liu and S. R. Nagel. Sound in a granular material: Disorder and nonlinearity. *Phys. Rev. B*, 48(21):646-650, 1993.

[60] S. Luding, E. Clément, A. Blumen, J. Rajchenbach, J. Duran. Studies of columns of beads under external vibrations. *Phys. Rev. E*, 49 (2) (1994) 1634.

[61] S. Luding, E. Clément, A. Blumen, J. Rajchenbach, J. Duran. Anomalous energy dissipation in molecular dynamics simulations of grains: The "detachment effect". *Phys. Rev. E*, 50 (1994) 4113.

[62] S. Luding. Stress distribution in static two-dimensional granular model media in the absence of friction. *Phys. Rev. E*, 55:4720–4729, 1997.

[63] S. Luding. Micro-macro transition for anisotropic, frictional granular packings. *Int. J. Sol. Struct.*, 41:5821–5836, 2004.

[64] S. Luding. Anisotropy in cohesive, frictional granular media. *Journal of Physics: Condensed Matter*, 17:2623–2640, 2005.

[65] S. Luding. Structure and cluster formation in granular media. *Pramana-Journal of Physics*, 64(6):893–902, 2005.

[66] S. Luding. Granular media: Information propagation. *Nature*, 435:159–160, 2005.

[67] S. Luding. Shear flow modeling of cohesive and frictional fine powder. *Powder Technology*, 158 (2005) 45–50.

[68] S. Luding, K. Manetsberger, J. Muellers. A discrete model for long time sintering. *Journal of the Mechanics and Physics of Solids*, 53(2) (2005) 455–491.

[69] S. Luding. About contact force-laws for cohesive frictional materials in 2d and 3d. *P. Walzel, S. Linz, C. Krülle, R. Grochowski (Eds.), Behavior of Granular Media*, Shaker Verlag, 2006, pp. 137–147, band 9, Schriftenreihe Mechanische Verfahrenstechnik, ISBN 3-8322-5524-9.

[70] S. Luding. Contact models for very loose granular materials. *P. Eberhard (Ed.), Symposium on Multiscale Problems in Multibody System Contacts*, IUTAM Bookseries Vol. 1, Springer, Dordrecht, The Netherlands, 2007, pp. 135–150.

[71] S. Luding. Cohesive, frictional powders: contact models for tension. *Granular Matter*, 10(4):235–246, 2008.

[72] S. Luding, A. Suiker. Self-healing of damaged particulate materials through sintering. *Philosophical Magazine*, 88, 28-29, 3445-3457, 2008.

[73] T.S. Majmudar and R.P. Behringer. Contact force measurements and stress-induced anisotropy in granular materials. *Nature*, 435(7045):1079–1082, 2005.

[74] H. A. Makse, N. Gland, D. L. Johnson, L. Schwartz. Nonlinear elasticity, sound propagation, and collective relaxation dynamics. *Phys. Rev. E*, 70, 061302, 2004.

[75] A. Merkel, V. Tournat, V. Gusev Elastic Waves In Unconsolidated Frictionless Granular Crystals. To appear in the proceedings of the International Congress On Ultrasonics, Universidad de Santiago De Chile, January 2009.

[76] E. A. Metzbower. Dispersion relations for hexagonal close-packed crystal lattices. *Physical Review*, 177(3):1139-1143, 1969.

[77] O. Mouraille and S. Luding. Sound propagation in dense, frictional granular materials. In R. Garcia-Rojo, H. J. Herrmann, and S. McNamara, editors, *Powders and Grains 2005*, page 319, Leiden, 2005. A. A. Balkema Publishers.

[78] O. Mouraille, N. Kruyt and S. Luding. Dispersion relations for frictional, random granu-lar media. in preparation.

[79] O. Mouraille, W. A. Mulder, S. Luding. Sound wave acceleration in granular materials. *J. Stat. Mech* (2006) P07023.

[80] O. Mouraille, S. Luding. Mechanic waves in sand: Effect of polydispersity. In: W. Peukert (Ed.), *Partec 2007*, 2007, CD proceeding.

[81] O. Mouraille, S. Luding. Sound wave propagation in weakly polydisperse granular materials. *Ultrasonics*, 48 (6-7), pp. 498-505, 2008.

[82] O. Mouraille, O. Herbst, S. Luding. Sound propagation in isotropically and uni-axially compressed cohesive, frictional granular solids. *Engineering Fracture Mechanics*, in press, 2009.

[83] H. B. Muhlhaus, F. Oka Dispersion and wave propagation in discrete and continuous models for granular materials. *Int. J. Solids Structures*, 33(19) 2841-2858 (1996).

[84] V. F. Nesterenko. Propagation of nonlinear compression pulses in granular media. *Journal of Applied Mechanics and Technical Physics*, 24 (5), pp. 733-743, 1983.

[85] V. F. Nesterenko. *Dynamics of Heterogeneous Materials*. Springer-verlag New York, 2001.

[86] T. Pialucha, C. C.H. Guyott, P. Cawley. Amplitude spectrum method for the measurement of phase velocity. *Ultrasonics*, vol 27, 270-279, 1989.

[87] T. Pöschel and T. Schwager. *Computational Granular Dynamics*. Springer, Berlin, 2005.

[88] D. C. Rapaport. The Art of Molecular Dynamics Simulation. *Cambridge University Press*, Cambridge, 1995.

[89] V. Richefeu, F. Radjai, M. S. El Youssoufi. Stress transmission in wet granular materials. *Eur. Phys. J. E*, 21 (4) (2006), pp. 359-369.

[90] A. Rosas, K. Lindenberg. Pulse dynamic in a chain of granules with friction. *Phys. Rev. E*, 68, 041304, 2003..

[91] W. Sachse, Y. Pao. On the determination of phase and group velocities of dispersive waves in solids. *L. Appl. Phys.*, 49(8), 4320-4327, 1978.

[92] M. H. Sadd, G. Adhikari, F. Cardoso. DEM simulation of wave propagation in granular materials. *Powder Technology*, 109(1-3): 222-233, 2000.

[93] Q. M. Tai and M. H. Sadd Contact law effects on wave-propagation in particulate material using distinct element modeling. *Int. J. Non-Linear Mech.* 28(2): 251-265, 1993.

[94] A. Santos. Does the Chapman-Enskog expansion for sheared granular gases converge? *Phys. Rev. Lett.*, 100 (2008) 078003.

[95] L. P. Sarma, N. Ravikumar. Q-factor by spectral ratio technique for strata evaluations, *Engineering Geology*, 57 (2000) 123-132.

[96] L. M. Schwartz, D. L. Johnson, S. Feng. Vibrational modes in granular materials. *Phys. Rev. Lett.*, 52(10), 831–834, 1984.

[97] J. Schwedes. Review on testers for measuring flow properties of bulk solids. *Granular Matter*, 5 (1) (2003) 1–45.

[98] F. M. Sears,B. P. Bonner. Ultrasonic Attenuation Measurement by Spectral Ratios Utilizing Signal Processing Techniques. *IEEE Transactions on geoscience and remote sensing*, Vol. GE-19, (2), 1981.

[99] N. Sela, I. Goldhirsch. Hydrodynamic equations for rapid flows of smooth inelastic spheres to Burnett order. *J. Fluid Mech.*, 361 (1998) 41–74.

[100] S. Sen, R. S. Sinkovits. Sound propagation in impure granular columns. *Phys. Rev. E* 54(6) 6857-6865, 1996.

[101] A. Shlivinski and K. J. Langenberg. Defect imaging with elastic waves in inhomogeneous-anisotropic materials with composite geometries. *Ultrasonics*, 46(1): 89-104, 2007.

[102] E. Somfai, J-N. Roux, J. H. Snoeijer, M. van Hecke, and W. van Saarloos. Elastic wave propagation in confined granular systems. *Physical Review E*, 72(2):021301, 2005.

[103] M. Sperl. Experiments on corn pressure in silo cells. translation and comment of Janssen's paper from 1895. *Granular Matter*, 8 (2) (2006) 59–65.

[104] A. S. J. Suiker, A. V. Metrikine, and R. de Borst. Comparisons of wave propagation characteristics of the Cosserat continuum model and corresponding discrete lattice models. *Int. J. of Solids and Structures*, 38:1563–1583, 2001.

[105] A. S. J. Suiker, and R. de Borst. Enhanced continua and discrete lattices for modelling granular assemblies. *Phil. Trans. R. Soc. A*, 363:2543–2580, 2005.

[106] Q. M. Tai and M. H. Sadd. A discrete element study of the relationship of fabric to wave propagational behaviours in granular materials. *Int. J. for Num. and Analytic meth. in Geomechanics*, 21(5): 295-311, 1997.

[107] P. Tarif, T. Bourbie. Experimental comparison between spectral ratio and rise time techniques for attenuation measurements. *Geophysical Prospecting* 35 (6), pp. 668-680, 1987.

[108] C. Thornton, K. K. Yin. Impact of elastic spheres with and without adhesion. *Powder Technol.*, 65 (1991) 153.

[109] C. Thornton, K. K. Yin, M. J. Adams. Numerical simulation of the impact fracture and fragmentation of agglomerates. *J. Phys. D: Appl. Phys.*, 29 (1996) 424–435.

[110] C. Thornton. Numerical simulations of deviatoric shear deformation of granular media. *Géotechnique*, 50 (1) (2000) 43–53.

[111] C. Thornton, S. J. Antony. Quasi-static deformation of a soft particle system *Powder Technology*, 109 (1-3) (2000) 179–191.

[112] C. Thornton, L. Zhang. A DEM comparison of different shear testing devices. In: Y. Kishino (Ed.), *Powders & Grains 2001*, Balkema, Rotterdam, 2001, pp. 183–190.

[113] M. N. Toksoz, D. H. Johnston, A. Timur. Attenuation of seismic waves in dry and saturated rocks: 1. Laboratory measurements. *Geophysics* 44, 1979, pp. 681.690.

[114] J. Tomas. Fundamentals of cohesive powder consolidation and flow. *Granular Matter*, 6 (2/3) (2004) 75–86.

[115] R. Tonn. The determination of the seismic quality factor Q from VSP data: a comparison of different computational methods. *Geophysical Prospecting*, 39 (1), (1991), pp. 1-27.

[116] R. Tonn. Comparison of seven methods for the computation of Q. *Phys. Earth. Planet. Inter.*, 55, 1989, pp. 259.268.

[117] A. Tourin, M. Fink, A. Derode Multiple scattering of sound, Topical review *Waves Random Media*, 10 (2000) R31–R60

[118] V. Tournat, B. Castagnede, V. Gusev, P. Bequin. Self-demodulation acoustic signatures for nonlinear propagation in glass beads. *Comptes Rendus Mecaniques*, 331(2) (2003) 119–125.

[119] V. Tournat, V. Zaitsev, V. Gusev, V. Nazarov, P. Bequin, B. Castagnede. Probing weak forces in granular media through nonlinear dynamic dilatancy: clapping contacts and polarization anisotropy. *Phys. Rev. Lett.*, 92(8):085502, 2004.

[120] V. Tournat, private communication (2007).

[121] B. Velicky, C. Caroli. Pressure dependence of the sound velocity in a two-dimensional lattice of Hertz-Mindlin balls: Mean-field description. *Physical Review E*, Statistical, Nonlinear, and Soft Matter Physics 65 (2), art. no. 021307, pp. 021307/1-021307/14, 2002.

[122] P. A. Vermeer, S. Diebels, W. Ehlers, H. J. Herrmann, S. Luding, and E. Ramm, editors. *Continuous and Discontinuous Modelling of Cohesive Frictional Materials*, Berlin, 2001. Springer. Lecture Notes in Physics 568.

[123] P. A. Vermeer, W. Ehlers, H. J. Herrmann, E. Ramm (Eds.) *Modelling of Cohesive-Frictional Materials*, Balkema at. Taylor & Francis, Leiden, Netherlands 2004, (ISBN 04 1536 023 4).

[124] C. Wensrich. Dissipation, dispersion, and shocks in granular media. *Powder Technology*, 126, 1-12, 2002.

Summary

In this study sound wave propagation through different types of dry confined granular systems is studied. With three-dimensional discrete element simulations, theory and experiments, the influence of several micro-scale properties: friction, dissipation, particle rotation, and contact disorder, on the macro-scale sound wave propagation characteristics are investigated.

Experiments, analyzed with the "Spectral Ratio Technique", make it possible to extract frequency-dependent propagation velocities and attenuation. An improved set-up for future investigations is proposed in order to better understand dispersion and propagation of sound in granular materials.

The full dispersion relation of a Face-Centered-Cubic lattice is derived from a theoretical analysis that involves translations, tangential elasticity, and rotations. The additional displacement and rotation modes and the energy conversion between them is studied using discrete element simulations. Simulations and theory are in perfect quantitative agreement for the regular lattices examined.

As a first small step away from order, systems with weak geometrical disorder (system structure) but strong contact disorder, i.e. with an inhomogeneous contact force distribution, are studied next. They reveal nicely the dispersive nature of granular materials and show strong frequency filtering. Low frequencies propagate, whereas high frequencies vanish exponentially. A more detailed study of how energy is transfered between different wavenumber bands shows linearly increasing transfer rates for increasing wavenumbers. A first theoretical approach using a linear Master Equation leads to a quantitative prediction of the energy evolution per band for short times.

A bigger second step in complexity is made by investigating the sound propagation in a realistic tablet made of a sintered frictional and cohesive polydisperse powder and prepared in different ways. These simulations nicely display history dependence and the effect of different material parameters.

As a conclusion, simulations were found to be a valuable tool to complement theoretical and experimental approaches towards the understanding of complex phenomena, such as sound propagation in (dry) granular materials. However, many open issues, in particular concerning the modeling, still remain.

Samenvatting

In dit werkstuk wordt geluidsgolf voortplanting in verschillende droge granulair systemen bestudeerd. De invloed van verschillende microschaal eigenschappen als wrijving, dissipatie, deeltjes rotatie en contact wanorde op de geluidsgolf voorplanting wordt met behulp van experimenten, theorie, en driedimensionale discrete elementen simulaties, onderzocht.

Experimenten zijn geanalyseerd met de "Spectral ratio technique" waarmee het mogelijk is om de frequentieafhankelijke golfvoortplantingssnelheid en dissipatie te bepalen. Een verbeterde experimentele opstelling is voorgesteld om het begrip van dispersie in granulair materialen te verduidelijken.

De dispersie relatie van een "Face-Centered-Cubic" rooster is afgeleid vanuit een theoretische analyse, die translaties, rotaties, en tangentiele elasticiteit bevat. De extra verplaatsingsmodes en de energie omzetting tussen hen is onderzocht. Simulaties en theorie komen zeer goed overeen waneer het de regelmatige roosters betreft.

Als eerste kleine stap weg van regelmaat, worden systemen met een zeer kleine geometrische ontregeling, maar met een grote contact ontregeling, bestudeerd. De dispersie relatie van granulair systemen wordt getoond samen met een sterke uitfiltering van frequenties. Lage frequenties kunnen zich voortplanten, terwijl hoge frequenties exponentieel worden gedampt. Een gedetailleerd onderzoek van hoe energie wordt overgedragen tussen verschillende golfgetallen laat zien dat de overzetting verhouding lineair toeneemt met het golfgetal. Een eerste theoretische benadering met een lineaire Master Vergelijking leidt tot een goede voorspelling voor korte tijden. Een grotere stap richting complexiteit is gemaakt met simulaties van golfvoortplanting in een realistische tablet gemaakt van een samengedrukt, wrijvend, cohesief poeder.

Als conclusie, er werd getoond dat simulaties een volwaardige methode vormen om samen met theorie en experimenten complexe fenomenen als golf voortplanting in droge granulair materialen te kunnen begrijpen. Echter, er zijn nog vele open vragen, in het bijzonder betreffende de modellering.

Acknowledgments

This is now the place to tell my gratitude to all the people that made this PhD work possible thanks to their help and support.

In the first place I would like to give my special thanks to Prof. Stefan Luding. Stefan, as my supervisor during these four and a half years you learned me a lot about physics and also about being a scientist. It was a very nice and interesting time. Your enthusiast, your patience, your kindness and your constant availability made it possible. Also I would like to thank your wife, Gerlinde for her direct and indirect support as she had to miss you quite some evenings and weekends during these years.

My thoughts are going now to Dr. Gerard Herman who abruptly passed away after one year of collaboration. Gerard, thank you for this short but nice time. At this occasion I want also to thank Prof. Wim Mulder who took Gerard's task over at Shell. Wim thank you for the nice and constructive remarks, discussions and collaboration.

A great thank you goes to Dr. Niels Kruyt who helped me a lot in the final stage of the PhD. Niels I enjoyed your readiness, your rigor and your sense of humor. Also I thank Prof. Holger Steeb for his kind help for the experimental part of the work.

As I spent three years at the Delft University of Technology in the former Particle Technology group held by Prof. Andreas Schmidt-Ott, I thank all the group for welcoming me during all those years. Thanks to Will and Karin for their help.

The last one and a half year of my PhD took place in the Engineering Fluid Dynamics group of Prof. Harry Hoeijmakers. I thank all Master students, PhD's and staff members for receiving me in the group for the last and most important year of my thesis. A special thanks to Anjenet and Wouter for their assistance.

The experimental part of the work was performed in the Department of Geotechnology at the Delft University of technology. Therefore I would like to thank Karel Heller and Dr. David Smeulders for the nice collaboration and the great support.

Also I am thankful to the "Laboratoire d'Acoustique de l'Universite du Maine" in general, who received me during a short but fruitful stay where I could increase my insight in acoustic experiments, and in particular to Prof. Vitali Gusev, Dr. Vincent Tournat and Aurelien Merkel for the nice discussions.

I would like to thank Dr. Akke Suiker, Prof. X. Jia, Dr. Andrei Metrikine, Dr. Elena Grekova and Dr. Ysbrand Wijnant for many interesting discussions.

As this work was part of the research programme of the Stichting voor Fundamenteel Onderzoek der Materie (FOM), financially supported by the Nederlandse Organisatie voor Wetenschappelijk Onderzoek (NWO) and the Stichting Shell Research, I thank all these organizations for their financial support.

Concerning FOM, I thank the "FOM-bureau" for the nice sport-days we spent together.

Furthermore I would like to thank many friends and colleagues that brought a lot of fun during nice discussions and activities in and around the PhD. So, Micha, Ciprian, Antina, Raghu, Robert, Orencio, Fatih, Olaf, Kazem, and Katia, Thanks!

Finally a great thank you to my family for supporting me from south of France! Also I am thankful to my wife's family for the "local" support. Last but not least a beautiful thank you to my lovely wife Sanne and our son Elia to whom I dedicated this thesis. Their love, patience and encouragments helped me so much in both good and difficult times.

About the author

December 26, 1979:	Born in Montpellier, France
June 1998:	Baccalauréat, Lycée Joffre, Montpellier, France
1998 - 2004:	Studies of Pure and Applied Mathematics, University of Science, Montpellier, France June 2004: Master in Mechanics Msc. thesis: Numerical modeling of reinforced geomaterials by wires using the non smooth contact dynamics
Jan-June 2003:	Erasmus student, Utrecht University, The Netherlands
2004 - 2008:	PhD research, Industrial partnership project Shell Research and FOM, Fundamenteel Onderzoek der Materie Delft University of Technology, the Netherlands, department of Particle Technology (2004-2007), University of Twente, the Netherlands, group of Multi-Scale-Mechanics (2007 - 2008) Thesis: Sound propagation in dry granular materials: discrete element simulations, theory, and experiments
2009 - present:	Design engineer at ASML, the Netherlands

Conferences

2005

Powders and Grains 2005, talk, Stuttgart, Germany.

2006

FOM-dagen Stroming en Warmte, poster, Veldhoven, the Netherlands.

JMBC day, poster, TU Delft, the Netherlands.

Dygram 2006 workshop, poster, Rennes, France.

2007

Physics at Veldhoven, FOM meeting, talk, Veldhoven, the Netherlands.

Partec 2007, talk, Nuremberg, Germany.

ICU 2007, talk, Vienna, Austria.

Eccomas, CFRAC 2007, talk, Nantes, France.

2008

Physics at Veldhoven, FOM meeting, poster, Veldhoven, the Netherlands.

Acoustics 2008, talk, Paris, France.

Publications

O. Mouraille and S. Luding:
Sound propagation in dense, frictional granular materials. In R. Garcia-Rojo, H. J. Herrmann, and S. McNamara, editors, *Powders and Grains 2005*, page 319, Leiden, 2005. A. A. Balkema Publishers.

O. Mouraille and S. Luding:
Mechanic wave in sand, 3D simulations. In: World Congress on Particle Technology 2006, Orlando, April 2006, CD Proceedings.

O. Mouraille, W. A. Mulder and S. Luding:
Sound wave acceleration in granular materials. *J. Stat. Mech*, 2006, P07023.

O. Mouraille and S. Luding.
Mechanic waves in sand: Effect of polydispersity. In W. Peukert editor, *Partec 2007*, 2007, CD Proceedings.

O. Mouraille and S. Luding:
Acoustic waves in granular materials. ICU 07, Vienna, Austria, April 2007, CD Proceedings.

O. Mouraille, and S. Luding:
Sound wave propagation in weakly polydisperse granular materials. *Ultrasonics*, 48 (6-7), pp. 498-505, 2008.

O. Mouraille, O. Herbst and S. Luding:
Sound propagation in isotropically and uni-axially compressed cohesive, frictional granular solids. *Engineering Fracture Mechanics*, in press, 2009.

O. Mouraille, N. P. Kruyt and S. Luding:
Dispersion relations for frictional, random granular media. In preparation.

M. Kleer, O. Mouraille, H. Steeb and S. Luding:
Spectral ratio technique for laboratory experiments on sand and glass beads. In preparation.

O. Mouraille and S. Luding:
Sound mode conversion in granular materials, a theoretical approach. In preparation.